Investigation of xBi(B')O_3-$(1-x)$$PbTiO_3$ and xBi(B',B")O_3-$(1-x)$$PbTiO_3$ Perovskite Solid Solutions with High Transition Temperatures

A Dissertation
Presented to
The Academic Faculty

by

Runrun Duan

In Partial Fulfillment
of the Requirements for the Degree
Doctor of Philosophy

School of Materials Science and Engineering
Georgia Institute of Technology
August 2007

Investigation of xBi(B')O_3-$(1-x)$$PbTiO_3$ and xBi(B',B")O_3-$(1-x)$$PbTiO_3$ Perovskite Solid Solutions with High Transition Temperatures

Approved by:

Dr. Robert F. Speyer, Advisor
School of Materials Science and Engineering
Georgia Institute of Technology

Dr. Christopher S. Lynch
School of Mechanical Engineering
Georgia Institute of Technology

Dr. Rosario A. Gerhardt
School of Materials Science and Engineering
Georgia Institute of Technology

Dr. Angus P. Wilkinson
School of Chemistry and Biochemistry
Georgia Institute of Technology

Dr. Meilin Liu
School of Materials Science and Engineering
Georgia Institute of Technology

Date Approved: July 5, 2007

ACKNOWLEDGEMENTS

I would like to express my deepest gratitude to my advisor, Dr. Robert Speyer, for his guidance and support over the past six years. He has been a tremendous mentor and taught me to be prudent, persistent and patient toward my research and my life. Thank you for providing me with the opportunity to pursue the research presented herein.

My sincere appreciation also goes to Dr. Rosario Gerhardt. She was always patient and willing to share her wisdom and insights on all wonderful things in the world of ferroelectrics and dielectrics. I am also very grateful to my committee members, Dr. Meilin Liu, Dr. Christopher Lynch and Dr. Angus Wilkinson, for their valuable suggestions and discussions of my research work.

I thank Dr. Shujun Zhang in Penn State University, whose familiarity with the needs and ideas of this field were very helpful during the research. Zhihao Bao, being my closest friend, provided me with a lot of help and friendship during past several years. I would also like to thank my colleagues, Yanli Xie, Zhe Cheng, Dr. Namtae Cho, Kathleen Silver and Fei Peng, for their assistance and friendship.

My parents have always encouraged me and cherished me with their love. I would not be where or who I am without them. Most thanks go to you, my beloved Qianning, for going through so many tough days, sharing the joys and sadness, and beginning a life long journey with me. Thank you for always being there for me.

TABLE OF CONTENTS

LIST OF TABLES

LIST OF FIGURES

SUMMARY

Perovskite solid solutions xBiInO$_3$-$(1-x)$PbTiO$_3$, (BI-PT), xBiLaO$_3$-$(1-x)$PbTiO$_3$ (BL-PT), and complex xBi(B', B")O$_3$-$(1-x)$PbTiO$_3$ (where B' and B" refer to 3+ cations) were fabricated using conventional ceramic processing. The extent of Bi(B')/(B',B")O$_3$ substitution in the perovskite system and the corresponding shifts in the transition temperatures were investigated using thermal analysis, dielectric measurements, x-ray diffraction, and electron microscopy.

For BI-PT system, maximum tetragonal perovskite distortion ($c/a = 1.082$) was obtained for $x = 0.20$, with a corresponding Curie temperature of 582°C. Nb modified BI-PT system with increased high temperature resistivity was evaluated for its transition temperature as well as electromechanical properties. BL-PT system showed reduced tetragonality and exhibited unique high temperature dielectric properties. Complex xBi(B', B")O$_3$-$(1-x)$PbTiO$_3$ solid solutions showed multiple dielectric constant peaks which were attributed to possible large cation (e.g. La^{3+}, In^{3+}, etc.) substitution into B-sites in the perovskite lattice.

CHAPTER 1

Introduction

1.1 Motivation

Piezoelectrics of commercial interest for transducer and actuator applications are generally comprised of solid solutions of $Pb(Zr_xTi_{1-x})O_3$ (PZT), with other perovskites whose compositions lie near the rhombohedral-tetragonal phase boundary (i.e., morphotropic phase boundary, MPB) [1, 2]. A MPB is defined as a temperature-independent narrow compositional range in which two crystallographic structures coexist, which gives rise to enhanced dielectric and piezoelectric properties [1]. Applications such as actuators for automotive fuel injectors, gyros, or vibration dampening, often require broader operational temperature ranges than currently available [3, 4]. Commercially available piezoelectric materials are generally limited to operating temperatures of one half T_C or approximately 150°C for most PZT formulations.

Perovskite structure can tolerate enormous amount of compositional modification, including many of the elements on the periodic table, enabling the tailoring of corresponding properties.

Even though a tremendous amount of work has been carried out on hundreds of ferroelectric compositions, research efforts have yet to provide a sufficient understanding of the phase stability of perovskite materials and a corresponding evaluation at property relationships. Specifically, the industrial and scientific communities have expressed the need for sensing and actuation over a broad temperature range.

The perovskite structure, illustrated in Figure 4.1, has the general formula: $A^{XII}B^{VI}O_3{}^{VI}$, where the Roman numerals represent the corresponding cation:anion coordination number. Based on the geometrical packing of charge spheres, Goldschmidt proposed the concept of

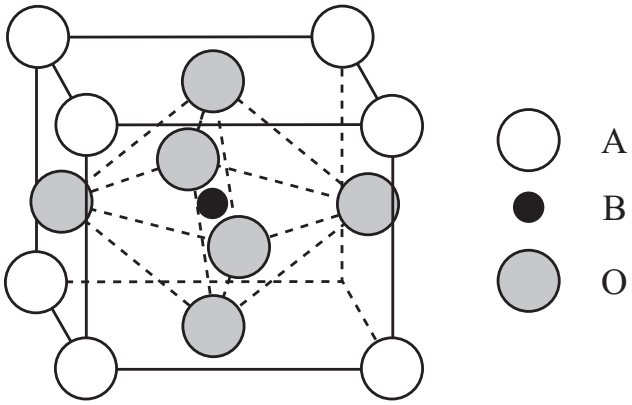

Fig 1.1: Illustration of a perovskite unit cell with the chemical formula ABO_3 (e. g. $BaTiO_3$).

a tolerance factor (t), given in equation 1.1:

$$t = \frac{(R_A + R_O)}{\sqrt{2}(R_B + R_O)} \tag{1.1}$$

where R_A, R_B, and R_O are the respective ionic radii [5]. The ideal tolerance factor for a perovskite material is one. Based on tolerance factor trends in perovskite ferroelectrics, a relationship between tolerance factor (t) and ferroelectric transition temperature (Curie temperature - T_C) for MPB systems was proposed by Eitel *et al* [6]. Using the ionic radii (denoted IR based on R_O= 0.140 nm) suggested by Shannon [7], the tolerance factor for the end members in $PbZrO_3$-$PbTiO_3$ (PZT), complex $Pb(B'B'')O_3$-$PBTiO_3$ solid solutions, and related MPB systems were calculated from equation 1.1. These end member tolerance factors were plotted as a function of the MPB transition temperature (T_C), as presented in Table 1.1 and Figure 1.2 [8].

This work will substantiate that the Curie temperature increases with decreasing tolerance factor of the end member used in materials to form solid solutions with lead titanate, as suggested in Figure 1.2 and Table 1.1. From the empirical analysis presented, $Bi(B')O_3$-based perovskites with decreasing values of 't' were suggested to confirm the premise. From Figure 1.2, it is evident that solid solutions of $BiScO_3$ ($t = 0.907$), $BiInO_3$ ($t = 0.884$), or $BiYbO_3$ ($t = 0.857$) with $PbTiO_3$ would form solid solutions that would have significantly greater T_C than PZT ($T_c = 386°C$). Following this general trend, a number of perovskites with the general formula $xBi(B')O_3$-$(1-x)PbTiO_3$ and $xBi(B',B'')O_3$-$(1-x)PbTiO_3$ solid

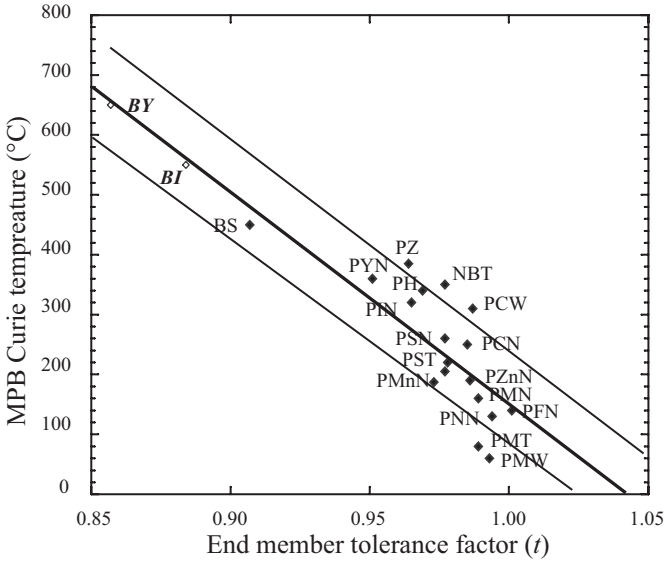

Fig 1.2: Curie temperature (T_c) of $PbTiO_3$-based MPBs versus end member tolerance factor. Compositions and properties are identified in Table 1.1 [8].

solutions were chosen to be investigated.

Tab 1.1: Tolerance factor (t), for end member ABO_3 compositions and Curie Temperature Data for MPB Solid Solutions with $PbTiO_3$ [$x ABO_3$- $(1-x)PbTiO_3$], list in order of increasing Curie Temperature [8]. (*, projected.)

Abbreviation	S.S end member $(1-x)AbO_3 + xPbTiO_3$	End member tolerance factor	Measured MPB Curie Temperature (°C)
PWN	$Pb(Mg,W)O_3$	0.993	60
PMT	$Pb(Mg,Ta)O_3$	0.989	80
PNN	$Pb(Ni,Nb)O_3$	0.994	130
PFN	$Pb(Fe,Nb)O_3$	1.001	140
PMN	$Pb(Mb,Nb)O_3$	0.989	160
PMnN	$Pb(Mn,Nb)O_3$	0.973	187
PZN	$Pb(Zn,Nb)O_3$	0.986	190
PST	$Pb(Sc,Ta)O_3$	0.977	260
PSn	$PbSnO_3$	0.978	220
PCN	$Pb(Co,Nb)O_3$	0.985	250
PSN	$Pb(Sc,Nb)O_3$	0.977	260
PCW	$Pb(Co,W)O_3$	0.987	310
PIN	$Pb(In,Nb)O_3$	0.965	320
PH	$PbHfO_3$	0.969	340
NBT	$(Na,Bi)TiO_3$	0.977	350
PWN	$Pb(Yb,Nb)O_3$	0.951	360
PZ	$PbZrO_3$	0.964	385
BS	$BiScO_3$	0.907	450
BI	$BiInO_3$	0.884	$\sim$550*
BY	$BiYbO_3$	0.857	$\sim$650*

1.2 Literature Review

1.2.1 Ferroelectric ceramics

Ferroelectricity was first discovered in Rochelle salt by Valesek in 1920. Further significant developments in the history of ferroelectric materials came in the 1940s when ferroelectricity was discovered in single crystal and polycrystalline barium titanate. The ferroelectric lead zirconate titanate (PZT) ceramic solid-solution compositions were developed [1] in the 1950s.

Ferroelectric ceramics have a number of properties which make them useful in a variety of applications. These include (1) a high dielectric constant, (2) high piezoelectric constants, (3) relatively low dielectric loss, (4) high electrical resistivity, (5) moisture insensitivity, (6) high electromechanical coupling, (7) medium hardness, (8) fairly high pyroelectric coefficients; and in some special compositions, also (9) high optical transparency and (10) high electroptic coefficients. Although these properties do not always combine to produce an optimum effect in any one application, one can see that the number of desirable properties provides the possibility for many new and unique applications. In addition, these properties can be continuously modified over specified ranges because many ceramic compositions form continuous solid solutions of one or more compounds in each other. Less obvious, but perhaps equally important, is the fact that most ceramics can be fabricated into complex shapes and are economical to produce [9].

Three prominent properties of ferroelectrics are their reversible polarization, their 'anomalous' properties and their non-linearities [10]. Ferroelectric materials are polar: They contain a permanent electric dipole at the unit cell level as a result of the local atomic arrangement, and this electric dipole spontaneously aligns with those in adjacent unit cells to yield a net polarization over many unit cell dimensions. Ferroelectricity can only occur in noncentrosymmetric crystal structures. The defining characteristic of a ferroelectric is that the direction of polarization is switchable; it can be changed in direction (within a limited set determined by the crystal symmetry) through the application of a sufficiently high electric field. Many crystals are polar; but unless the polarization is reversible with the field , the crystal is not considered ferroelectric.

The spontaneous alignment of dipoles over many unit cells result in formation of a microstructural entity known as a ferroelectric domain. For instance, when the cubic paraelectric phase of $BaTiO_3$ transforms to the tetragonal phase upon cooling below the Curie point, the displacement of the Ti^{4+} ion can occur along one of the six $\langle 100 \rangle$ directions of the cubic phase. A cooperative alignment among neighboring unit cells results in the formation of a ferroelectric domain which may be oriented in any one of these six directions. If only one orientation were to form throughout a single crystal, then we would have a single domain, and the opposing surfaces of the crystal where the polarization terminates would be oppositely charged. This kind of long-range charge separation is energetically unfavorable, and instead a number of domain orientations tend to form in all but the smallest crystallites, as illustrated in Figure 1.3a.

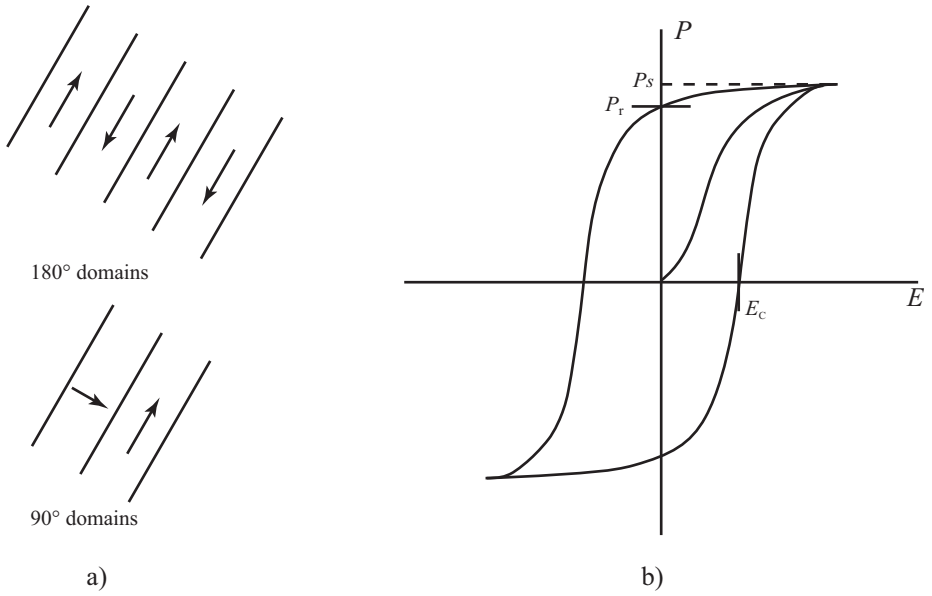

Fig 1.3: a) Polarization vectors in ferroelectric domains of 180° and 90° misorientation. b) A typical ferroelectric hysteresis loop.

In tetragonal $BaTiO_3$, adjacent domains can have their polarization vectors in antiparallel directions or at right angles to one another. The boundaries between these domain walls are about one unit cell in thickness and have a small positive energy. The formation comes at the expense of this interfacial energy. In $BaTiO_3$ the ferroelectric domains form as lamellae that are typically a few tens of a micrometer to a micrometer in thickness.

Upon application of a sufficiently high electric field, ferroelectric domains can be oriented or "poled". While domains cannot be perfectly aligned with the field except when the grain or crystal is coincidentally oriented to its c- or a-axis in the field direction, their polarization vectors can be aligned to maximize the component resolved in the field direction. The process of poling requires the motion of domain walls. In principle, a randomly oriented polycrystal of a tetragonal ferroelectric can achieve a maximum polarization that is 83% of the single crystal value. In practice much lower values are frequently observed due to incomplete domain orientation (domain wall *pinning*) wall motion. Domains misoriented by 180° tend to switch more easily than 90° domain walls since no net physical deformation is required; domains misoriented by 90° are inhibited from switching by the strain which accommodates the switching of c-and a-axes [11].

A consequence of resistance to domain switching is that polarization in a ferroelectric is hysteretic; it is not precisely reversible with the field. This behavior is illustrated in Figure 1.3b. Starting with a material in which domains are randomly oriented and yield zero macroscopic polarization, the initial shallow slope of P vs. E is that of the paraelectric component of susceptibility. At some higher field, on the order of several kV/cm for $BaTiO_3$ and the PZT/PLZT family of ferroelectrics, domain orientation begins to take place. This results in a sharply rising P with increasing field E; that is, a high dielectric susceptibility. The polarization cannot increase without limit, however, and reaches a *saturation polarization* P_s, which corresponds to the maximum degree of domain orientation possible for that material. Upon decreasing the field back to zero, some of the polarization will be lost (the paraelectric component as well as some ferroelectric contributions) but a *remnant polarization* P_r is retained. Upon reversing the direction of the field E, the polarization is removed until at some *coercive field* E_c a net zero polarization is again obtained. Further increases in the reverse field lead to saturation of P in the opposite direction.

The temperature at which a ferroelectric material reverts to the high temperature paraelectric prototype phase is called the Curie temperature (T_C). Most ferroelectrics cease to be ferroelectric above T_C. The anomalous behavior in dielectric constant near T_C is as significant as the reversible polarization, although it is not definitive of a ferroelectric. The

permittivity ϵ rises sharply to a very high peak value at the temperature T_C; the very high values in this neighborhood are referred as *anomalous* values, as can be seen in Figure 1.4. The permittivity values of ferroelectrics are high even in temperature regions not close to T_c. The permittivity ϵ can be measured by putting a pair of electrodes on the crystal and using any suitable a.c. method of measuring the crystal capacitance. Above the Curie temperature T_C, the dielectric anomaly is frequently of the $Curie-Weiss$ form to a good approximation.

$$\epsilon = \frac{4\pi C}{T - T_C}$$

C is known as the Curie constant. ϵ falls off rapidly below T_c. While in some cases, the form of the anomaly above T_c is not approximately Curie-Weiss.

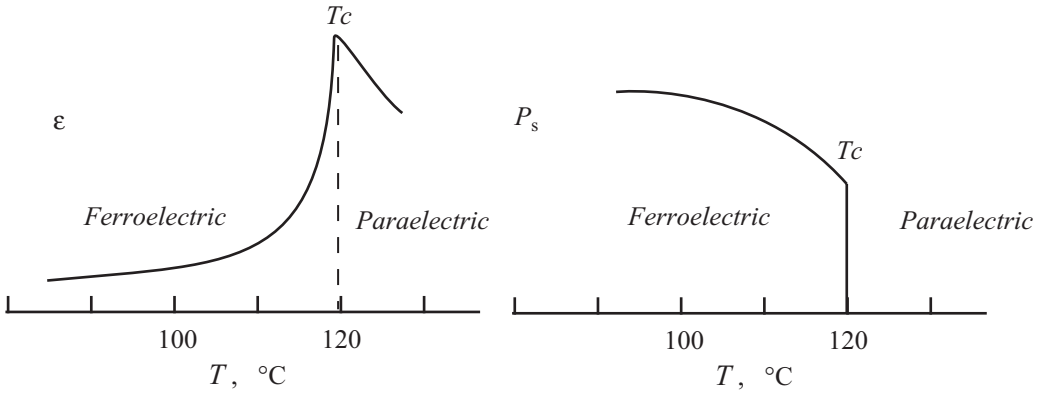

Fig 1.4: Permittivity (left diagram) and polarization (right diagram) of barium titanate, to show the electric anomaly.

1.2.2 Piezoelectric ceramic materials and selected properties

1.2.2.1 Curie temperature (T_C)

The Curie point of a ferroelectric material is the temperature above which it loses its characteristic ferroelectricity. At temperatures below the Curie point the dipole moments are partially aligned within ferroelectric domains in ferroelectric materials. As the temperature is increased from below the Curie point, thermal fluctuations increasingly destroy this alignment, until the net polarization becomes zero at and above the Curie point. In some materials, this is not observed as they decompose prior to passing into the paraelectric

state [12]. Above the Curie point, the material is purely paraelectric (as displayed in Figure 1.4). In the disordered state above the Curie temperature, thermal energy overrides any interactions between the local dipole moments of ions. Below the Curie temperature, these interactions are predominant and cause the local moments to order or align so that there is a net spontaneous polarization.

In the ferroelectric case, as temperature T increases from absolute zero, the spontaneous polarization decreases from P_0, its value at T = 0. At first this occurs gradually, then with increasing rapidity until the spontaneous polarization disappears at the Curie temperature. In ferroelectric materials the course of polarization with temperature may be more complicated, but the spontaneous polarization disappears at the Curie temperature.

This loss of net polarization with increased temperature, termed 'thermally activated aging', degrades the properties of the ferroelectrics. A maximum usage temperature of $\frac{1}{2}T_C$ (in Celsius) is usually applied [13] in order to slow down this effect. In lead-based piezoelectrics, high T_C compositions often come along with higher coercive fields. The improved domain stability under high mechanical and electrical stresses is very important for high power devices [13]. High T_C ferroelectrics also offer improved temperature stability in their electrical performance.

1.2.3 Piezoelectricity

Piezoelectricity is a property possessed by a select group of materials. It was discovered in 1880 by Pierre and Jacques Curie. However, the term 'piezoelectricity' (pressure electricity) was first suggested by W. Hankel in 1881. Cady [**?**] defines piezoelectricity as "electric polarization produced by mechanical strain in crystals belonging to certain classes, the polarization being proportional to the strain and changing sign with it." Two effects are manifest in piezoelectricity: the direct effect is identified with the phenomenon whereby polarization is generated from a mechanical stress, dielectric displacement D is proportional to the stress σ;

$$D = d \cdot \sigma \tag{1.2}$$

whereas the converse effect is associated with the mechanical movement generated by the application of an electrical field, an applied field E produces a proportional strain ε.

$$\varepsilon = d \cdot E \tag{1.3}$$

Both effects are useful and have found application in present-day devices.

1.3 References

REFERENCES

[1] B. Jaffe, W. R. Cook and H. Jaffe, *Piezoelectric Ceramics*, Academic Press, New York, (1971).

[2] D. A. Berlincourt, C. Molik and H. Jaffe, "Piezoelectric Properties of Polycrystalline Lead Titanate Zirconate Compositions," *Proceedings of the IRE* **2** 220 (1960).

[3] H. Lammer, "Flexible Piezoelectric Films," International Patent No. WO 02081401 (October 2002).

[4] S. Yoshikawa, A. Bogue and B. Degon, "Commercial Application of Passive and Active Piezoelectric Vibration Control," *Proceedings of the 11th IEEE International Symposium on Applications of Ferroelectrics*, Montreux, Switzerland, 293 (1998).

[5] V. M. Goldschmidt, *Geochemistry*, Edited by N. F. Mott and S. E. Bullard, Clarendon Press, Oxford, (1954).

[6] R. Eitel, C. Randall, T. Shrout, S. Park, P. Rehrig and W. Hackenberger, "New High Temperature Morphotropic Phase Boundary Piezoelectrics Based on $Bi(Me)O_3{-}PbTiO_3$ Ceramics," *Jpn. J. Appl. Phys.*, **40** [10] 5999 (2001).

[7] R. D. Shannon, "Revised Effective Ionic Radii and Systematic Studies of Interatomic Distances in Halides and Chalcogenides," *Acta. Crystallogr*, Sec. A, **32** [A] 751 (1976).

[8] S. E. Park and T. R. Shrout, "Characteristics of Relaxor-Based Piezoelectric Single Crystals for Ultrasonic Transducers," *IEEE Transactions on Ultrasonics, Ferroelectrics, and Frequency Control*, **44** [5] 1140 (1997).

[9] R. C. Buchanan, *Ceramic Materials for Electronics: Processing, Properties, and Applications*, Marcel Dekker, New York, (1986).

[10] J. Burfoot, *Ferroelectrics: An Introcuction to the Physical Principles*, Van Nostrand, London, (1967)

[11] Y. Chiang, D. P. Birnie and W. D. Kingery, *Physical Creamics*, John Wiley & Sons, New York, (1997).

[12] L. A. Shuvalov, "Symmetry Aspects of Ferroelectricity," *Journal of the Physical Society of Japan*, **28** [supplement] 38 (1970).

[13] R. C. Turner, P. A. Fuierer, R. E. Newnham and T. R. Shrout, "Materials for High Temperature Acoustic and Vibration Sensors: A Review," *Applied Acoustics*, **41** 299 (1994).

CHAPTER 2

Preparation and Characterization of High Curie Temperature $BiInO_3$-$PbTiO_3$ and Nb doped $BiInO_3$-$PbTiO_3$ Perovskites Solid Solutions[0]

2.1 $BiInO_3$-$PbTiO_3$ System

2.1.1 Experimental procedure

2.1.1.1 Mixed oxide powders

Powder mixtures of xBI-$(1-x)$PT, with x values from 0.05 to 0.35 in steps of 0.05 were prepared by ball-milling PbO (Hammond Lead Products), Bi_2O_3 (Alpha Aesar), In_2O_3 (Alpha Aesar) and TiO_2 (anatase, Aldrich Chemical Co., Inc.) at room temperature in plastic jars for 4 h in ethanol and deionized water (1:1 ratio), using 8 mm diameter partially stabilized zirconia milling media. An additional 3 mol% PbO was added to ensure a Pb-rich atmosphere during firing [1]. Each slurry was then dried for ∼12 h at 90°C. The as-dried mixture was ground using an alumina mortar and pestle, and passed through an 80-mesh sieve to eliminate large particle lumps. Portions of the resulting powder were pressed at ∼150 MPa into cylindrical pellets (16 mm in diameter and ∼1.7 mm in height). These compacts were fired in covered MgO crucibles at 450, 750, 825 (all held for 4 h), 1000 and 1100°C (both held for 2h, the shorter time was used to reduce the PbO loss). Heating rates were 8°C/min and cooling occurred in the furnace with no power applied to the heating elements. Additional loose powder of the same composition as the pellets was placed around the pressed pellets in the crucible to create an overpressure of the volatile constituents.

[0]Published in *Journal of Materials Research* **19** [7] 2185 (2004) and *Journal of Materials Research* **20** [8] 2067 (2005)

Powder mixtures were also fired via a two-step process. Powders were shaped using a die and punch into softly pressed cylindrical disk compacts, and calcined (reacted) in magnesia crucibles at 850°C for 4 h. These were then remilled for 4-5 h, dried, passed through an 80-mesh sieve, and then pressed at ∼150 MPa into cylindrical pellets of 6.2 mm in diameter and ∼5 mm in height. These green bodies were then fired in covered MgO crucibles with surrounding powder of the same composition, heating at 8°C/min to 1050, 1100, or 1150°C and soaking for 2 h. A sample calcined at 1000°C for 2 h was also prepared by crushing with a mortar and pestle, re-pressing at ∼150 MPa, and then heating at 8°C/min to 1150°C and soaking for 2 h.

2.1.1.2 Sol-gel prepared powders

Polycrystalline samples of composition BI-PT were prepared from: lead acetate ($Pb(COOCH_3)_2$, Research Chemical Ltd.) indium acetate ($In(COOCH_3)_3$, Indium Corporation of America), bismuth acetate ($BI(COOCH_3)_3$, Alfa Aesar) and titanium *n*-butoxide ($TiC_{16}H_{36}O_4$, ACROS). Glacial acetic acid, isopropyl alcohol, and distilled water were used as solvents. Lead acetate was dissolved in glacial acetic acid (650 g per liter). Separately, a 1:1 molar mixture of bismuth and indium acetates was dissolved in a 1:4 volume mixture of distilled water and glacial acetic acid, so that there was 50 g of indium acetate and 66.25 g bismuth acetate to 1 liter of solvent. This mixture was heated at 80°C in a conical flask under stirring for 1 h. Titanium *n*-butoxide was dissolved in glacial acetic acid and isopropyl alcohol (1:1:1 in volume ratio), and this solution was poured slowly into the previous mixture under stirring to obtain a sol. Mixtures of the three solutions were of molar ratios to generate x values identical to those prepared for the mixed oxides. The sol was held at 70°C under constant stirring for 48 h to yield a light yellow gel. These gels were then dried at ∼100°C for 24 h. These were in turn ground using a mortar and pestle into powders and heated at 3°C/min to soaking temperatures of 450, 500, 550, and 600°C for 6 h, in covered magnesia crucibles. In a two-step process, samples heat-treated at 600°C were crushed using a mortar and pestle and then pressed (150 MPa) into cylindrical pellets ∼5 mm thick and 6.2 mm in diameter, and heated at 4°C/min to 1000 or 1150°C, soaking for 2.5 h (a 900°C soak was

also evaluated for $x = 0.15$). As before, loose powder of the same composition was placed around the pellets in the covered MgO crucibles.

2.1.2 Characterization

Phase analyses of heat-treated and crushed (using a mortar and pestle) compositions were performed by powder X-ray diffraction (XRD) using CuKα radiation at a scanning speed of 0.015° per step with one step per second. Lattice parameters for the tetragonal perovskite-structured phase were determined using the extrapolation method [2], in which lattice parameters, calculated from each diffraction peak, were plotted against $(1/2)(\cos^2\theta/\sin\theta + \cos^2\theta/\theta)$. $\langle hk0\rangle$ diffraction lines were used to determine the lattice parameter a, and $\langle 00l\rangle$ diffraction lines were used to determine the lattice parameter c. The true lattice parameters were determined by extrapolating to where this function is zero ($2\theta = 180°$). An example is shown in Figure 2.1.

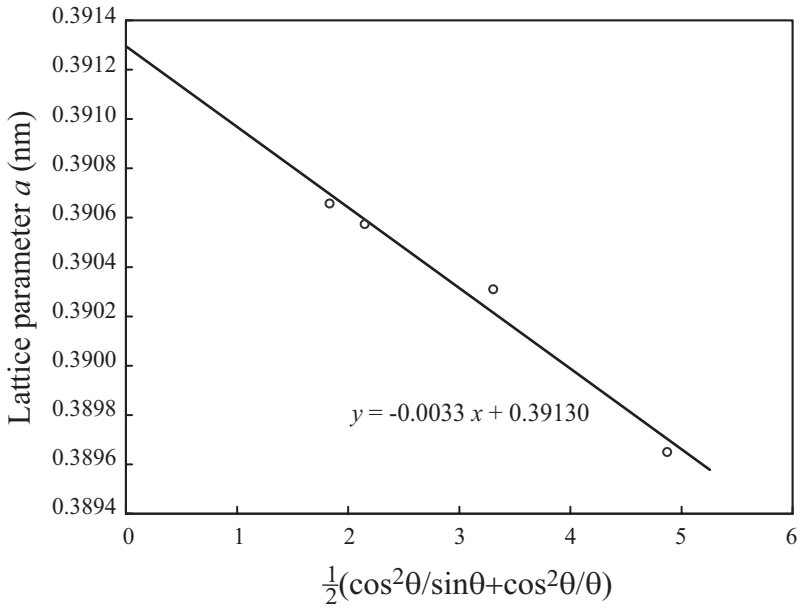

Fig 2.1: Example of extrapolation method: Lattice parameter a of a xBI$-(1-x)$PT sample with $x = 0.10$, fired at 1000°C.

Tab 2.1: Phases identified after heat-treatment of compositions to various temperatures. T: TiO_2 (anatase, ICDD: 21-1272). B: Bi_2O_3 (ICDD: 41-1449). P: PbO (massicot, i.e. yellow lead oxide, ICDD: 38-1477). L: PbO (litharge, ICDD: 05-0561). I: In_2O_3 (ICDD: 06-0416). R: $PbTiO_3$, tetragonal perovskite structure (e.g. ICDD: 06-0452). C: cubic $PbTiO_3$ (ICDD: 40-0099). Q: $Pb_3Bi_2O_6$ (ICDD: 45-0657). U: unidentified peaks at 26.4° and 34.2° 2θ. Subscript "tr" indicates a trace quantity.

Temperature	$x = 0.05$	$x = 0.10$	$x = 0.15$	$x = 0.20$	$x = 0.25$	$x = 0.30$	$x = 0.35$
25°C	T,B,I,P,L	T,B,I,P,L	T,B,I,P,L	T,B,I,P,L	T,B,I,P,L	T,B,I,P,L	T,B,I,P,L
450°C	T,B,I,P,L,U	T,B,I,P,L,U	T,B,I,P,L,U	T,I,B,P,L,U	T,B,I,P,L,U	T,B,I,P,L,U	T,B,I,P,L,U
750°C	C,R_{tr},I	C,R_{tr},I	C,R_{tr}	C,I	C,I	C,I,Q	C,I, Q
825°C	R	R,I_{tr}	C,R,I	C,R_{tr},I	C,R,I	C,R,I,Q	C,R,I,Q
1000°C	R,I_{tr}	R,I_{tr}	R	R,I_{tr}	R,I	R,I,Q	R,I,Q
1100°C	R	R,I_{tr}	R,I_{tr}	R,I_{tr}	R,I_{tr}	R,I,Q	R,I,Q

2.1.3 Results and discussion

2.1.3.1 Results of mixed oxides

Table 2.1 lists the phases identified for xBI-$(1-x)$PT compositions based on comparison with the ICDD database as a function of temperature. XRD patterns for $x = 0.15$ are shown as a function of temperature in Figure 2.2. Batch oxides reacted between 450 and 750°C to form a phase which can be roughly correlated to a cubic perovskite structure ("pseudo-cubic," see discussion). At and above 825°C for $x \preceq 0.10$, and at and above 1000°C for $x \succeq 0.15$, peaks corresponding solely to the tetragonal perovskite structure were detected, along with trace amounts of In_2O_3. For $x \succeq 0.30$ and temperatures at and above 750°C, the concentration of In_2O_3 was more substantial, and peaks corresponding to $Pb_3Bi_2O_6$ were identified, in addition to the tetragonal perovskite-structured phase.

After reaction heat-treatment at or above 1000°C, the a lattice parameter of the tetragonal perovskite-structured phase dilated in roughly even steps with increasing x up to $x = 0.30$, while dilation of the c lattice parameter with x was greater in magnitude, yet halted at $x = 0.20$ (Figure 2.3). Correspondingly, the c/a ratio increased up to $x = 0.20$, and then decreased over the range $0.20 \preceq x \preceq 0.30$, showing no clear trend thereafter.

Figure 2.4a is an SEM micrograph of a pressed mixed oxide particle compact prior to heat-treatment, showing an average particle size of ∼200 nm, with the exception of Bi_2O_3 particles (as indicated by EDS), which were in the range of 5 μm. After heat treatment at

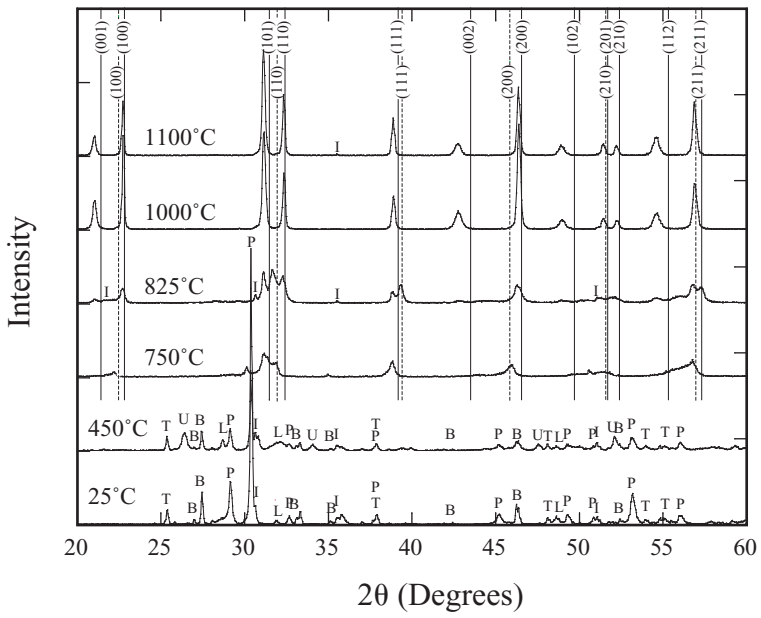

Fig 2.2: XRD patterns for $x = 0.15$ heat-treated to various temperatures. Symbols have the same meaning as in Table 2.1. Solid lines correspond to ICDD data for $PbTiO_3$ adopting the tetragonal perovskite structure and similarly, dashed lines indicate cubic-structured $PbTiO_3$.

750°C, particles similar in appearance as the ∼200 nm starting particles were seen, but voids took the place of the larger Bi_2O_3 particles (Figure 2.4b). Formation of faceted particles in some regions is also apparent. After heat-treatment at 825°C, distinct regions of larger faceted particles, as well as the smaller particles of the size of the original batch, may be seen (Figure 2.4c). After heat-treatment at 1000°C, ∼5 μm cube-shaped particles formed (Figure 2.4d). Dimensional densities of microstructures such as that in Figure 2.4d were ∼65% of theoretical. Theoretical densities (TD) were calculated based on lattice parameters measured for the various compositions from XRD.

Two-step firing, with an 850°C pre-calcining step, resulted in more densified microstructures (Figure 2.5).

Densities of samples with $x = 0.05$ and $x = 0.10$ are not plotted in Figure 2.5 since they broke apart after firing. The $x = 0.20$ composition soaked at 1100°C sintered to 93.0% of TD. A typical microstructure after such a 2-step firing is shown in Figure 2.6a.

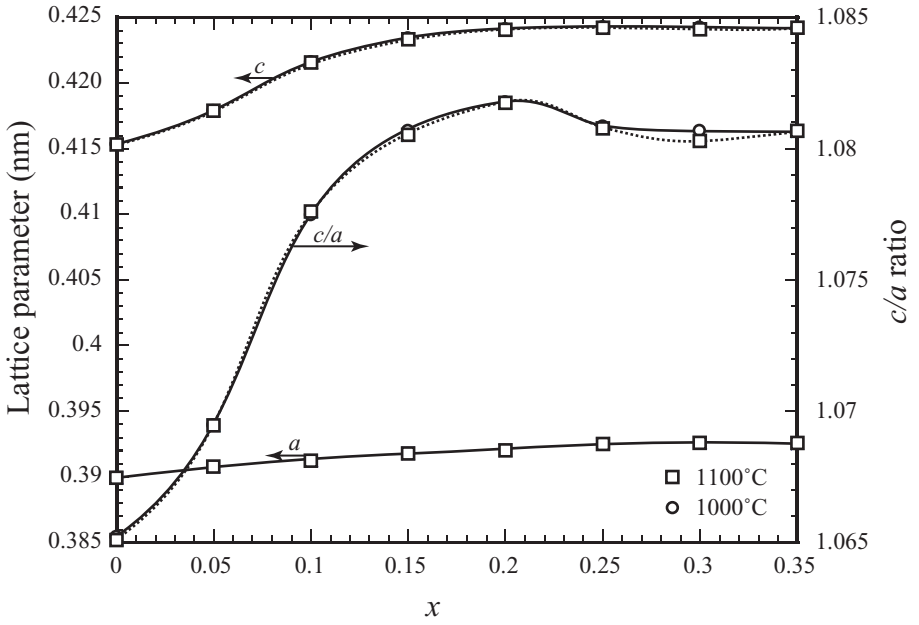

Fig 2.3: Change in the lattice parameters a, c, and their ratio vs. composition and temperature.

After crushing the agglomerated cubes formed by pre-calcining at the higher temperature of 1000°C, re-pressing and refiring, an Archimedes density of 94.7% of TD was obtained (Figure 2.6b).

Figure 2.7 shows DSC traces of samples with various compositions as a function of temperature. Endotherm onsets, interpreted as the Curie temperatures (ferroelectric-paraelectric transformation), increased significantly with x up to $x = 0.15$. Figure 2.8 shows the DSC-determined Curie temperature overlayed with the XRD-determined c/a ratio as a function of composition; both traces follow a similar trend. An $x = 0.15$ sample soaked at 825°C, which showed both tetragonal and pseudo-cubic-structured (see discussion) perovskite phases, showed two distinct DSC endotherms (Figure 2.9, traces a and b). The higher temperature endotherm matches with the Curie temperature endotherm for this composition after soaking at 1100°C (trace c).

2.1.3.2 Results of sol-gel fabrication

DTA traces of heated gels showed partially superimposed exotherms in the range 250-400°C in nearly the same position for all values of x(Figure 2.10). A smaller exotherm over the

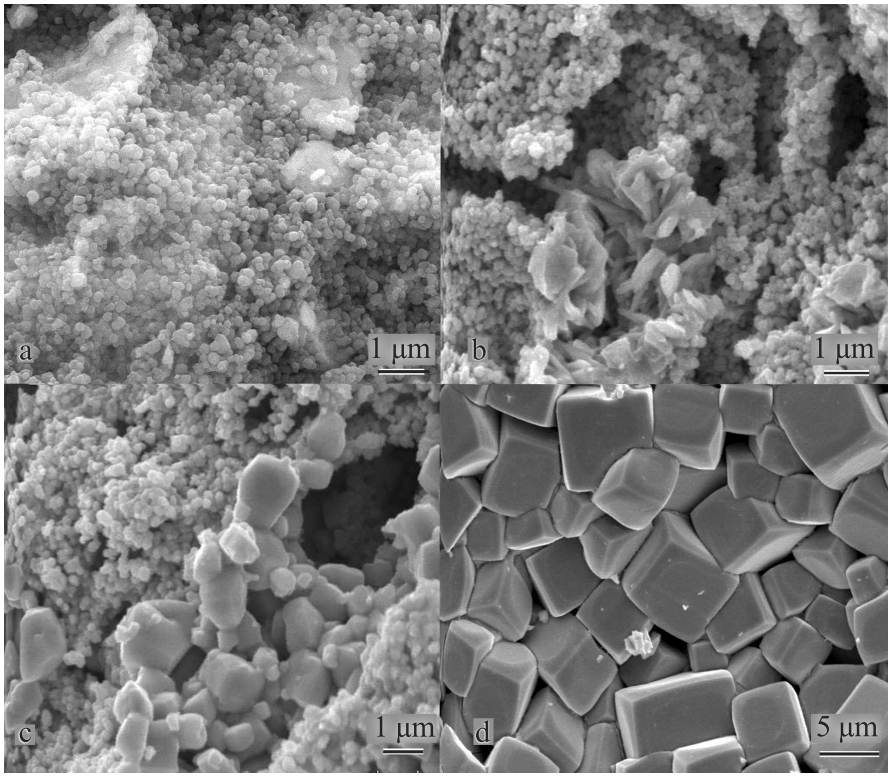

Fig 2.4: Secondary electron SEM images. a) Green body compact before heat-treatment ($x = 0.15$). b) Fractured surface of a $x = 0.15$ fired compact soaked at 750°C for 4 h. c) Fractured surface of a $x = 0.15$ fired compact soaked at 825°C for 4 h. d) Fractured surface of a $x = 0.15$ fired compact soaked at 1000°C for 2 h.

range 420-520°C was apparent for batches of low x ($0.05 \preceq x \preceq 0.15$), which was not observed for batches with $x = 0.20$ and higher. For all batches, a sharp weight loss was measured over the range 200-300°C, with a minor residual weight loss measured above 300°C for $x \preceq 0.10$. The final weights reached were ∼70% of original weight, except for $x = 0.35$ which had its final weight at ∼79% of its original weight(Figure 2.11).

Table 2.2 shows the XRD-identified phases after heat treatment of sol-gel-prepared xBI-$(1 - x)$PT, as a function of soak temperature and composition. For samples soaked in the range 450-600°C, phase-pure tetragonal perovskite was identified for $x \preceq 0.10$ and a cubic perovskite phase best-corresponded to XRD peaks for $x \succeq 0.15$, with In_2O_3 identified as a second phase for $x \succeq 0.30$. XRD results from 600°C soaks for various compositions are shown in Figure 2.12, where both pseudo-cubic- and tetragonal-structured perovskite diffraction peaks were broadened. XRD patterns for $x = 0.15$ as a function of temperature

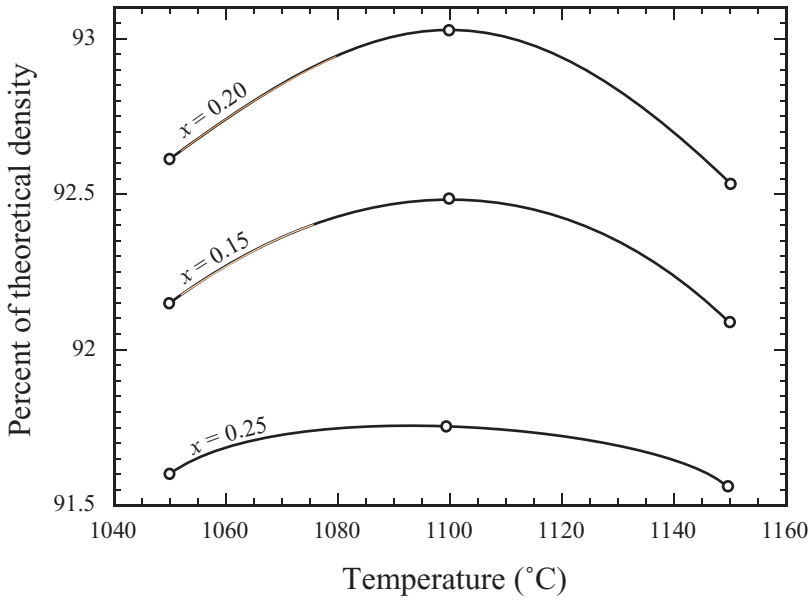

Fig 2.5: Archimedes densities, relative to theoretical densities, for various compositions calcined at 850°C for 4 h, milled, re-pressed, and then soaked at various temperatures for 2 h.

are shown in Figure 2.13.

After two-step processing, broadened peaks converted to sharp peaks. Lattice parameter calculations on the pseudo-cubic-structured perovskite phases ($x \succeq 0.15$), i.e. assuming a single lattice parameter for all diffraction peaks, showed inconsistencies. Lattice parameter dilation for the tetragonal perovskite-structured phase formed after 2-step heat treatment at 1150°C as a function of x is shown in Figure 2.14.

DSC traces of all compositions showing the broadened pseudo-cubic or tetragonal perovskite structures showed no endotherm corresponding to a Curie temperature transformation. However after two-step heat treatments, similar DSC results to those of mixed oxides were observed.

Figure 2.15a is a TEM micrograph of a $x = 0.05$ sol-gel-prepared powder heat-treated at 600°C, showing an average particle size in the range of ∼50 nm.

Figure 2.16shows the particle sizes of sol-gel processed samples with different x after heat-treatment at various temperatures up to 600°C, based on XRD peak broadening. For samples soaked at the same temperature, average particle sizes decreased with increasing

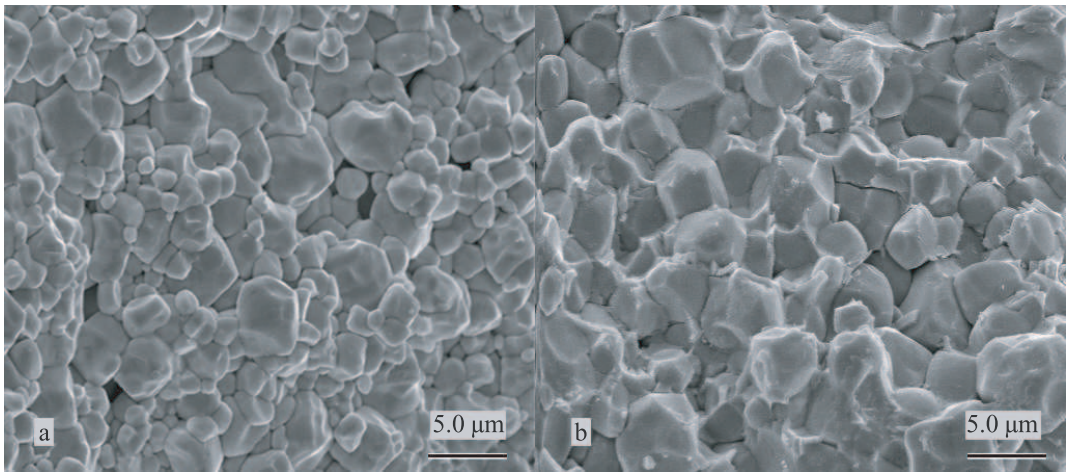

Fig 2.6: a) Fractured surface of a specimen pre-reacted from mixed oxide powders at 850°C for 4 h, re-milled, dry pressed at ∼150 MPa, and heat treated at 1100°C for 2 h. b) Fractured surface of a specimen pre-reacted from mixed oxide powders heat-treated at 1000°C for 4 h, crushed with a mortar and pestle, dry pressed at ∼150 MPa, and heat treated at 1150°C for 2 h.

x. For temperatures below 550°C, average particle size increased slightly with increasing soak temperature.

Figure 2.15b shows the microstructure of a two-step fired sol-gel-prepared sample, showing an average grain size of ∼5 μm. Figure 2.17 shows the Archimedes densities of two-step fired sol-gel-prepared samples. These densities were higher than those obtained with mixed oxide powders; the $x = 0.20$ sample reached 98.2% of TD. Figure 2.18 shows the DSC traces of the crushed sol-gel-prepared samples fired at 1150°C, with $x = 0.05$ and $x = 0.15$. The Curie temperature indicated by the onsets of the endotherms of those samples were almost identical to the results obtained from the mixed oxides method.

2.1.3.3 Discussion of mixed oxides

Mixed oxide raw materials reacted between 450 and 750°C. Bi_2O_3 melts at 825°C, but forms eutectic liquids with other batch constituents at lower temperatures; the Bi_2O_3-PbO binary system [3] shows a 730°C eutectic. The Bi_2O_3 particles fused, wetting and reacting with the remaining particles, in turn forming a pseudo-cubic perovskite structured phase either at the soaking temperature or during cooling. This phase is referred to as pseudo-cubic since the individual diffraction peaks did not split into peaks corresponding to a tetragonal

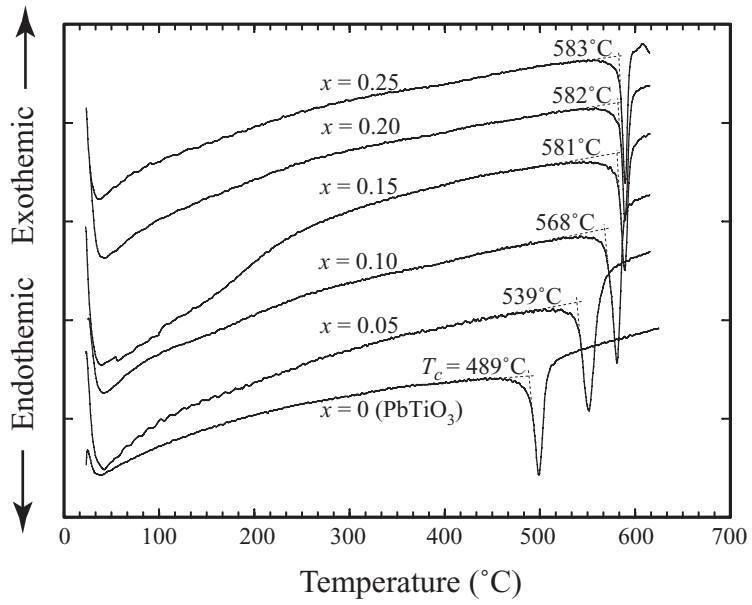

Fig 2.7: DSC traces of specimens of various compositions, previously soaked at 1100°C for 2 h. Scan rate: 8°C/min.

distortion, yet do not all uniformly fit a single lattice parameter. A non-cubic distortion of some form for this phase is also implied by the DSC endotherm (Figure 2.9) attributed to that phase, interpreted as a Curie temperature transformation which would only occur in a non-cubic phase. Cube-shaped particles of tetragonal perovskite-structured compound then grew out of the liquid phase starting at 750°C (to a greater extent for lower values of x). After heat treatment at 825°C for $x \preceq 0.10$ and after heat-treatment at 1000°C for higher values of x, the microstructure had completely transformed to the tetragonal perovskite cubes. For compositions up to $x = 0.25$, virtually phase-pure xBI-$(1-x)$PT formed (i.e. only trace amounts of In_2O_3 were detected).

The solubility of Bi and In in the $PbTiO_3$ solid solution for $x \preceq 0.25$ is confirmed both by the fact that additional phases of In_2O_3 and $Pb_3Bi_2O_6$ were detected only for $x \succeq 0.30$, and by the a and c lattice parameters remaining unchanged only over this latter compositional range. The maximum tetragonal distortion was measured for $x = 0.20$, though the vast majority of lattice distortion had occurred by $x = 0.15$. This is borne out by DSC-measured Curie temperatures, which reached a near-saturated value of 581°C for $x = 0.15$. The DSC-determined Curie temperature for pure $PbTiO_3$ of 489°C corresponds well to the literature

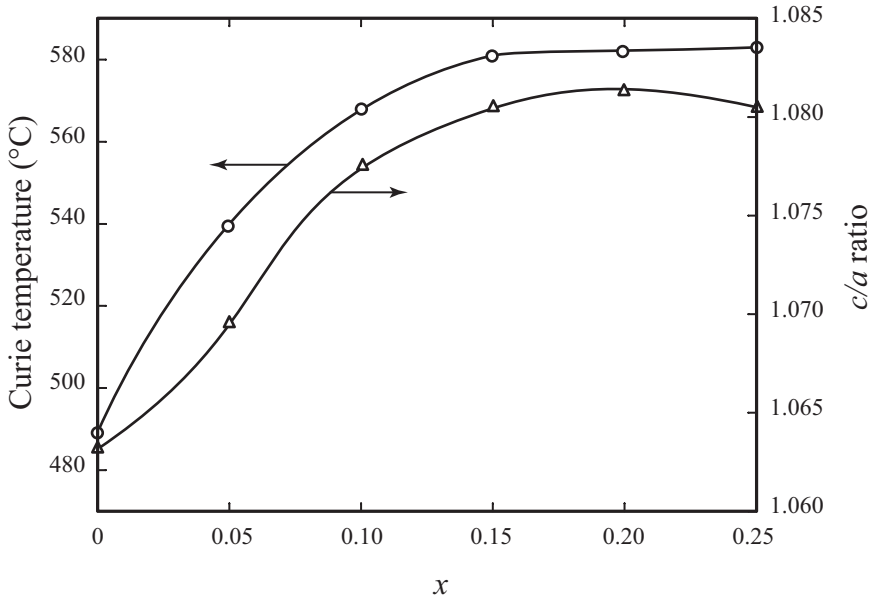

Fig 2.8: DSC-determined Curie temperature and XRD-determined c/a ratio of samples soaked at 1100°C for 2 h as a function of composition.

value of 490°C [4].

The formation of randomly-oriented tetragonal perovskite cubes during the initial heat-treatment did not lend toward the formation of a dense microstructure. Heat-treatments at 1100°C appeared to provide the closest approach (Figure 2.5). Below that temperature, inadequate thermal energy was provided for sintering, and above that temperature, the vapor pressure of lead oxide became a factor. Upon pulverizing the cube agglomerates, the cubes then assembled tightly upon re-pressing, resulting in a higher density after a second firing. This was especially true if the cubes were fully formed, e.g. after calcining at 1000°C, in which a fired density of 94.7% of theoretical was obtained from dry-pressed particles with no additives. Use of processing organics to increase green body density should further improve the fired density of the mixed oxides.

2.1.3.4 Discussion of sol-Gel fabrication

Reactions among sol-gel constituents to form a phase-pure perovskite compound occurred as low as 200-300°C. For $x \preceq 0.10$, the formed compound was tetragonal, while for higher values of x, it was pseudo-cubic. For these compositions, this pseudo-cubic phase converted

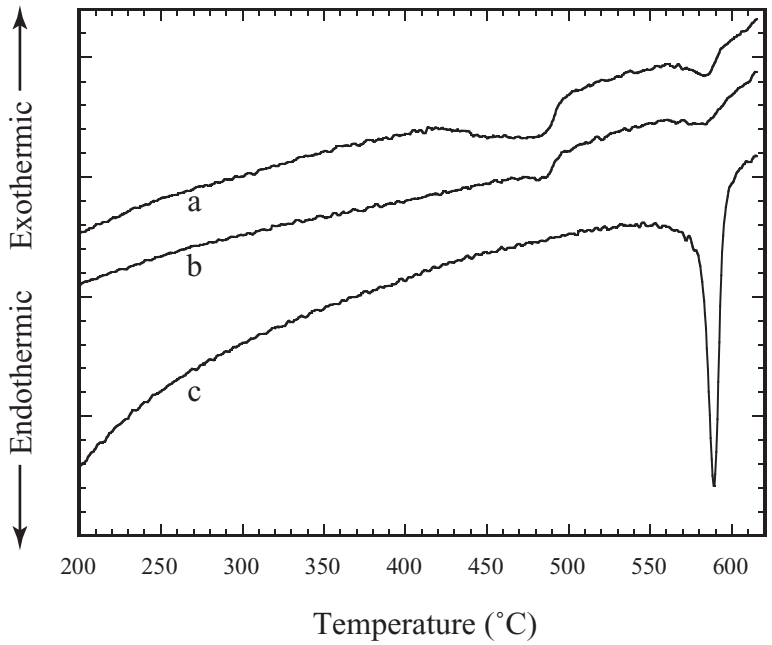

Fig 2.9: DSC traces: a) $x = 0.15$ specimen previously heat treated at 825°C for 4 h, first DSC scan. b) Repeated DSC scan on the same specimen as in a). c) $x = 0.15$ specimen previously heat-treated at 1100°C for 2 h.

to tetragonal after two-step heat-treating at or above 1000°C. After soaking at 1150°C, not even trace amounts of In_2O_3 were detected for compositions of $x \preceq 0.15$. The extent of x which formed phase-pure perovskite solid solution was the same as for mixed oxides, as was the trend in dilation of c and a lattice parameters.

The average particle size of the sol-gel-prepared calcined particles was substantially smaller than the average size of cubes formed from reaction among mixed oxides, ∼25 nm compared to ∼5 μm for mixed oxides. Upon crushing, pressing, and refiring sol-gel specimens, higher fired densities were obtained for sol-gel-prepared samples (as high as 98.2% of TD) as compared to those obtained from calcined mixed oxide particles. Grain sizes for these two-step fired sol-gel samples were ∼2 orders of magnitude larger than the particles formed after the first heat-treatment step. The mechanism by which this substantial coarsening occurs remains to be established. For both mixed oxide and sol-gel-based fabrication methods, within the solubility limits observed, a change in perovskite structure via passing through the MPB was not detected.

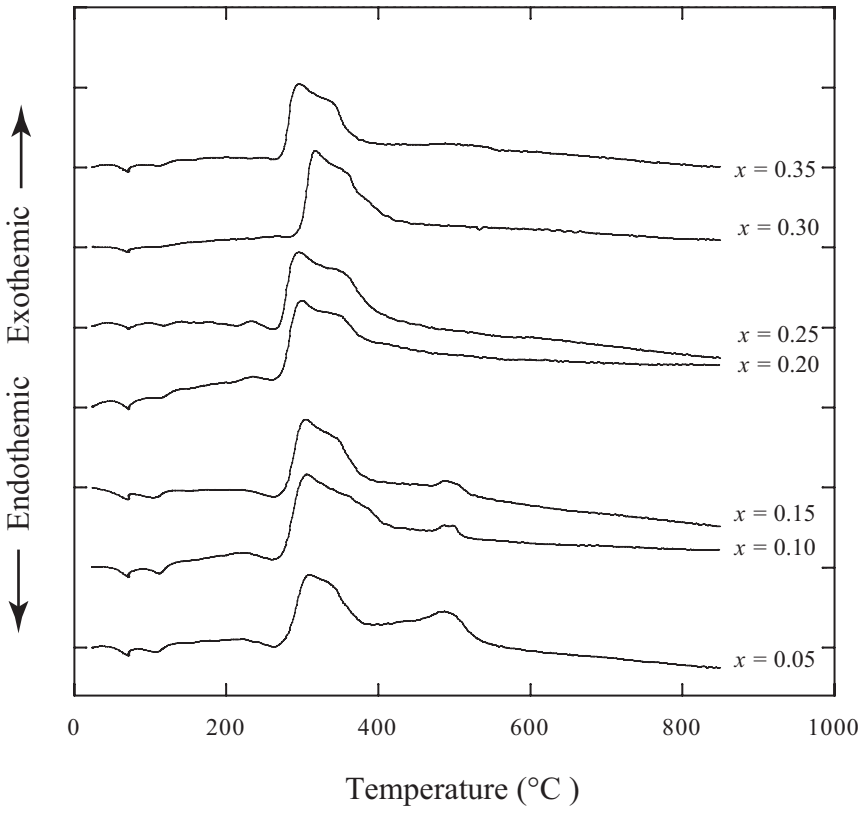

Fig 2.10: DTA trace of gel powders over the composition range $x = 0.05$ to $x = 0.35$, heated at 5°C/min to 850°C.

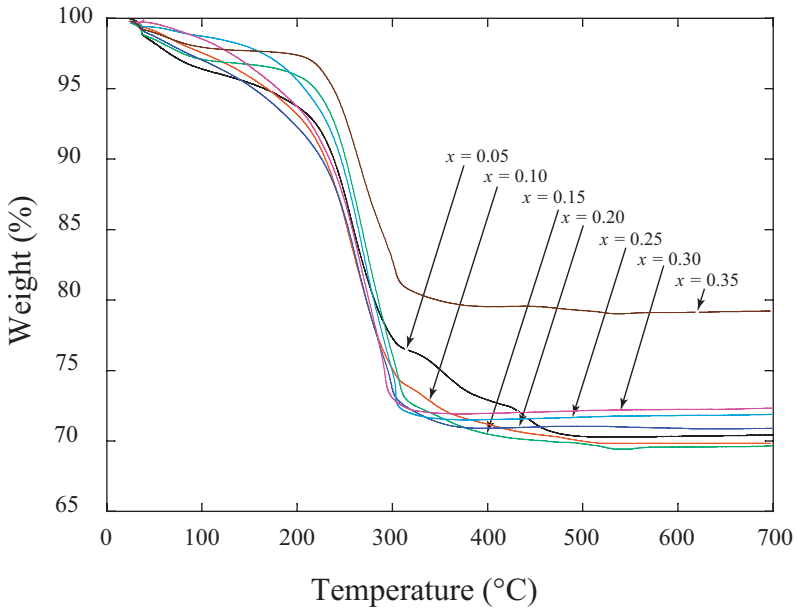

Fig 2.11: TG trace of gel powders with $x = 0.05$ to $x = 0.35$, heated at 5°C/min to 700°C.

Tab 2.2: Phases detected from sol-gel-processed samples of various compositions, after heated-treating at the indicated temperatures for 6 h (450-600°C) or in two-step processes, heat-treated at 600°C for 6 h, crushed, re-pressed, and then heat-treated at 1000 or 1150°C for 2.5 h. R: tetragonal perovskite $PbTiO_3$ (e.g. ICDD: 06-0452). C: cubic perovskite $PbTiO_3$ (e.g. ICDD: 40-0099). I: In_2O_3 (ICDD: 06-0416). Q: $Pb_3Bi_2O_6$ (ICDD: 45-0657). U': Unidentified peak at 26.8°C 2θ. −: Broadened peaks which could not be identified. X: Specimen fused.

Temperature	$x = 0.05$	$x = 0.10$	$x = 0.15$	$x = 0.20$	$x = 0.25$	$x = 0.30$	$x = 0.35$
450°C	R	R	C	C	–	–	–
500°C	R	R	C	C	C	C	C, I
550°C	R	R	C	C	C	C,I	C,I,U'
600°C	R	R	C	C	C	C,I	C,I,U'
1000°C	R	R	C,R,I	R,I	R,I	R,I,Q	R,I,Q
1150°C	R	R	R	R,I_{tr}	R,I	R,I,Q	X

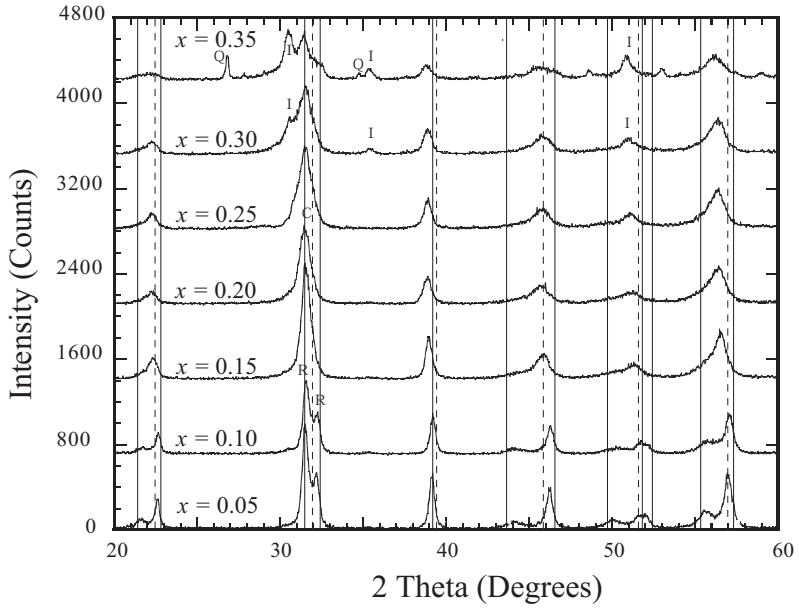

Fig 2.12: XRD patterns of sol-gel prepared powders heat treated at 600°C for 6 h. Dashed lines correspond to cubic $PbTiO_3$ (ICDD: 40-0099) and solid lines correspond to the tetragonal $PbTiO_3$ (ICDD: 06-0452). I: In_2O_3 (ICDD: 06-0416). Q: $Pb_3Bi_2O_6$ (ICDD: 45-0657).

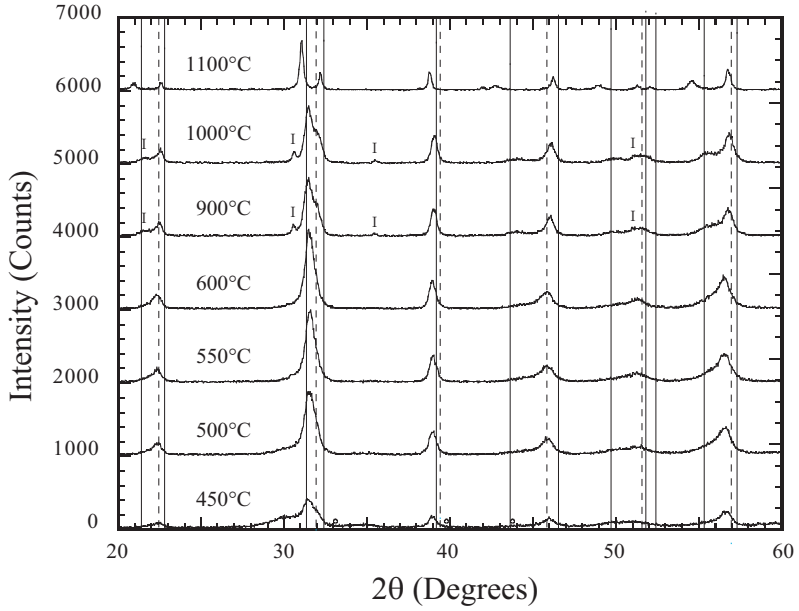

Fig 2.13: XRD patterns of sol-gel prepared powders of $x = 0.15$ soaked at various temperatures. Diffraction patterns labeled 900, 1000, and 1150°C correspond to a two-step heat treatment. Markers and lines are as defined in Figure 2.12.

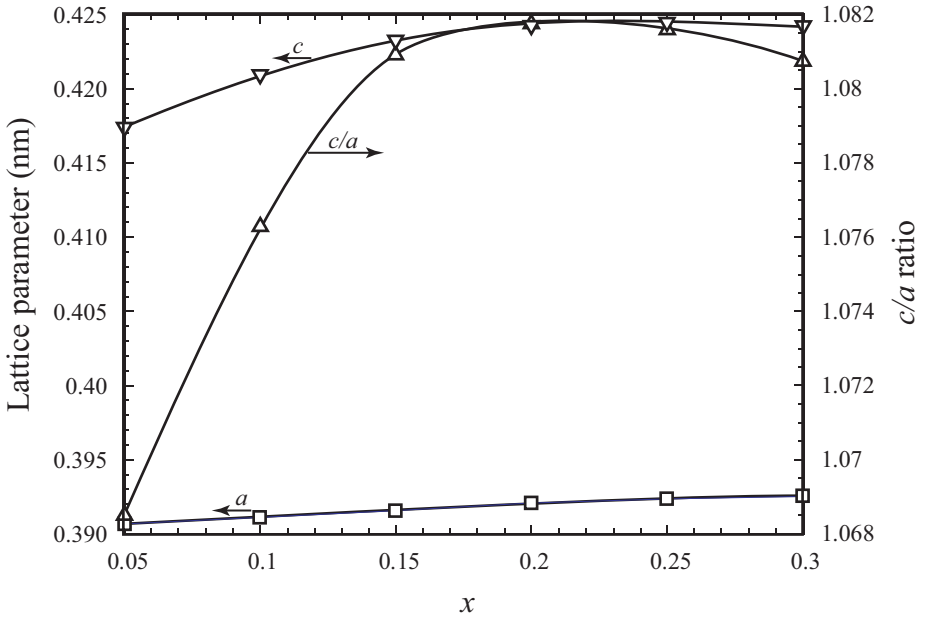

Fig 2.14: Change in the lattice parameters a, c, and their ratio vs. composition for sol-gel prepared specimens soaked at 1150°C for 2 h.

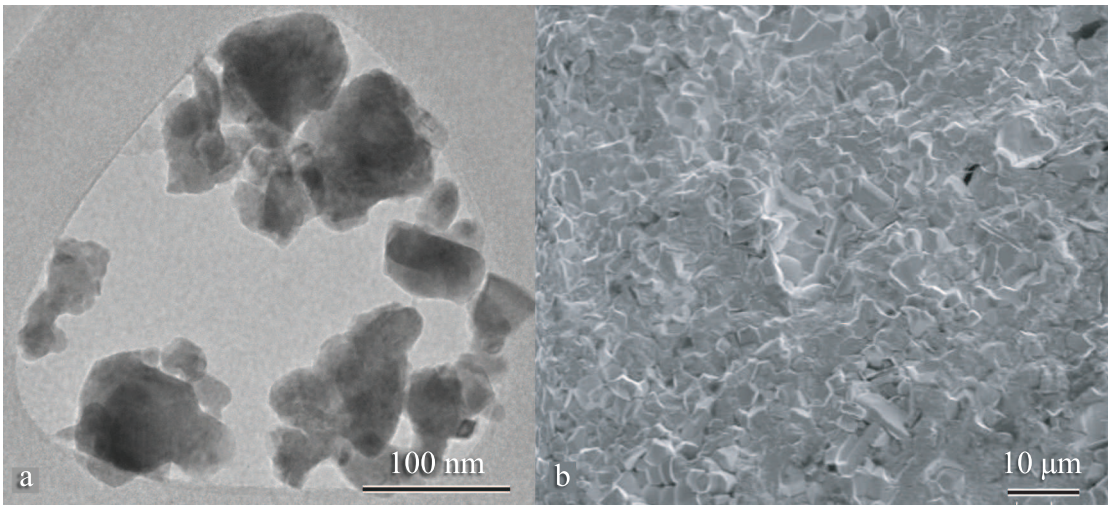

Fig 2.15: a) TEM micrograph of sol-gel-prepared powder soaked at 600°C for 6 h. b) SEM micrographs of fractured surface of a sol-gel-prepared $x = 0.20$ composition, calcined at 600°C for 6 h, crushed and pressed into a pellet which was soaked at 1150°C for 2.5 h.

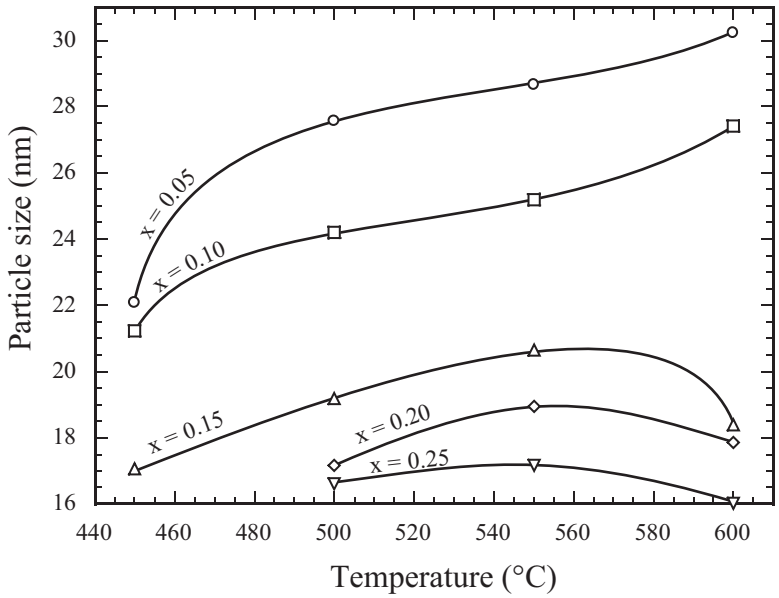

Fig 2.16: Particle sizes of the sol-gel-processed samples as a function of composition and soaking temperature.

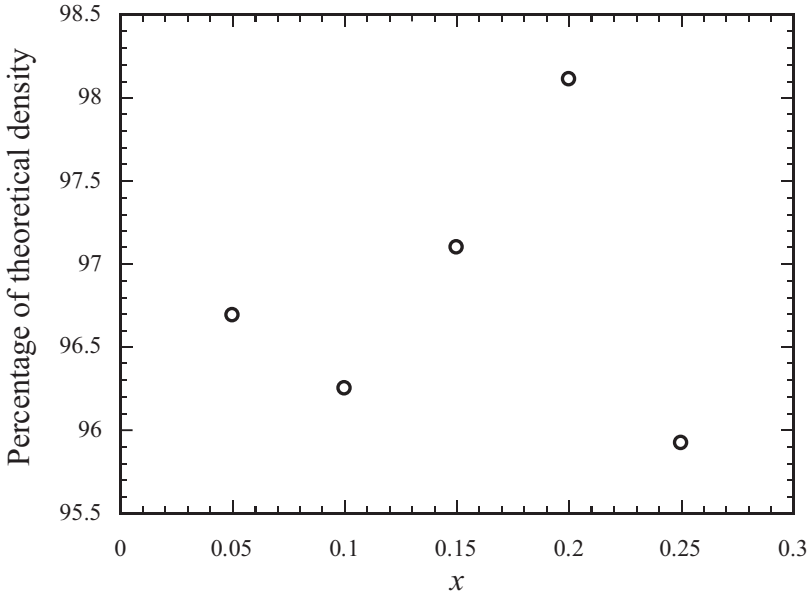

Fig 2.17: Archimedes densities (relative to theoretical densities) of sol-gel-prepared samples of various compositions, exposed to the 2-step heat treatment described in the caption to Figure 2.15b.

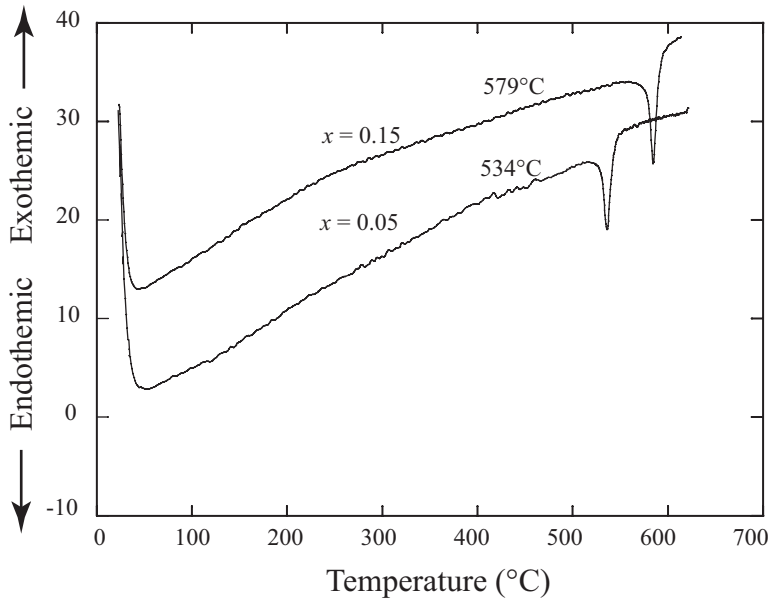

Fig 2.18: DSC traces of the crushed pre-calcined sol-gel prepared samples fired at 1150°C, for $x = 0.05$ and $x = 0.15$.

2.2 Nb doped $BiInO_3$-$PbTiO_3$ Perovskites

2.2.1 Experimental procedure

Pure and Nb- modified xBI-$(1-x)$PT (BI-PT)($x = 0.15,\ 0.20$) ceramics were synthesized using conventional solid-state reaction. High purity materials In_2O_3 (Alfa Aesar), Bi_2O_3 (MCP Inc.), Pb_3O_4 (Alfa Aesar) and TiO_2 (Ishihara) were used as starting materials. The powders were vibratory milled and subsequently calcined at 950°C for 6 h. Nb_2O_5 (Alfa Aesar) in the range 1-3 mol%, was used as a donor additive in the calcined materials, and the mixture was vibratory milled again. The mixed powders were pressed into cylindrical pellets of 12 mm in diameter and 1.5 mm in thickness. The pellets were embedded in the calcined source and placed in a sealed alumina crucible, then sintered at 1100°C for 2 h. An Archimedes density of 96-97% of theoretical density was obtained for the samples after sintering. The samples were ground down to 0.2-0.5 mm in thickness, then were electroded with a post-fire silver paste (Dupont 6160) on parallel faces and fired at 750°C. Dielectric properties as a function of temperature were measured from 1 kHz to 1 MHz frequencies using multi-frequency LCR meter (HP 4284A) over the temperature range from room temperature to 650°C. High field measurements including polarization hysteresis and strain-electric field curve were measured using a modified Sawyer-Tower circuit and linear variable differential transducer (LVDT) driven by a lock-in amplifier (Stanford Research Systems, Model SR 830). The piezoelectric coefficient d_{33} was measured using a Berlincourt-style d_{33} meter (ZJ-2, Institute of Acoustics Academia Sinica). Resistivity was measured using Keithley model 2410-C source-meter when applying 100V across the disk samples.

Disk samples with dimensions of ∼10 mm in diameter and ∼0.5 mm in thickness were used to determine the planar mode (k_p) and thickness mode (k_t) electromechanical coupling factors. Shear mode samples (k_{15}) were prepared with dimensions 10 × 10 × 0.5 mm^3. The samples were firstly poled along the length direction, the electrode was subsequently removed and re-sputtered on the thickness direction. The electromechanical coupling factors k_t and k_{15} were calculated using the equation $k_{15,t}^2 = \frac{\pi}{2}\frac{f_r}{f_a}\cot[\frac{\pi}{2}\frac{f_r}{f_a}]$ [5], while the coupling k_p was calculated by the formula $1/k_p^2 = 0.398\frac{f_r}{f_a - f_r} + 0.579$ [7, 8], where f_r is the

resonance frequency and f_a the anti-resonance frequency, measured by using an HP 4194A impedance/gain-phase (Hewlett-Packard) analyzer.

2.2.2 Results and discussion

X-ray powder diffraction (XRD) performed on the modified $0.15BiInO_3$-$0.85PbTiO_3$ (1.5 mol% Nb) is presented in Figure 2.19. A pure tetragonal perovskite phase was detected

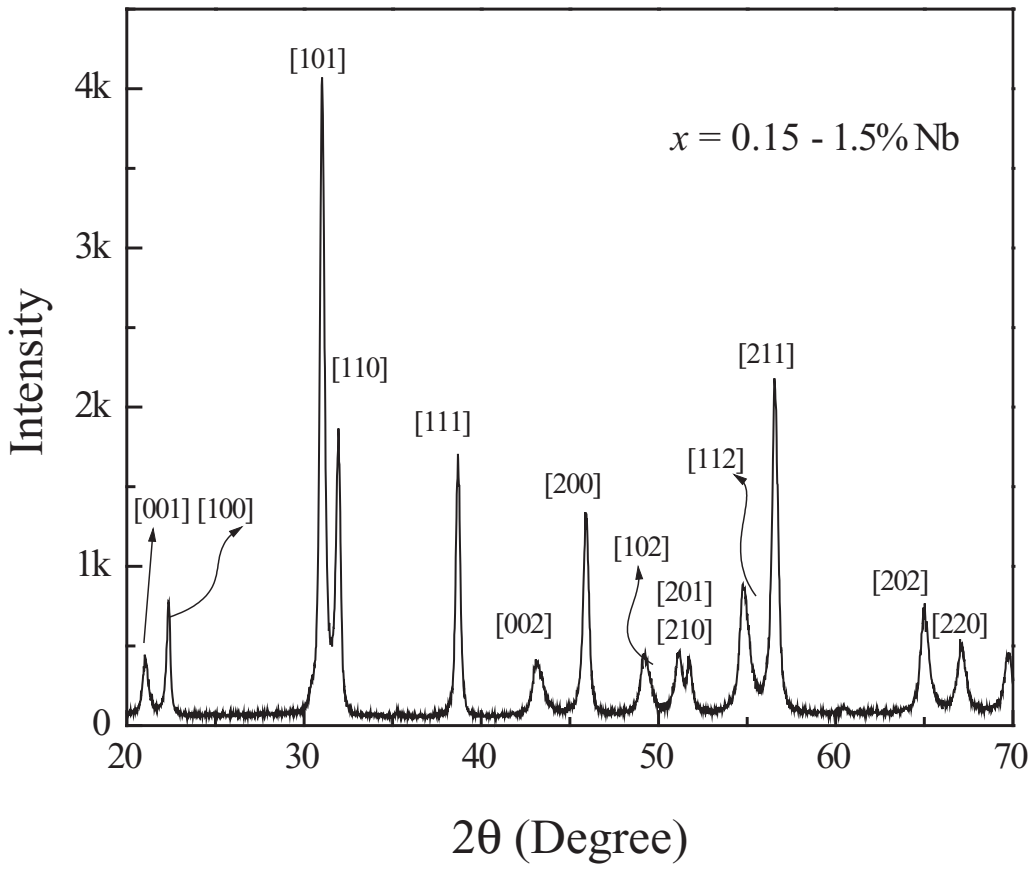

Fig 2.19: X-ray powder diffraction of niobium-modified $0.15BiInO_3$-$0.85PbTiO_3$, showing pure tetragonal perovskite phase.

with a c/a ratio calculated to be 1.067 (c = 0.4121 nm and a = 0.3864 nm were determined using the extrapolation method [2]), smaller than the values reported [6] because of the niobium additive. This slight reduction in c/a ratio is similar to the niobium-modified $Bi_4Ti_3O_{12}$ ceramics with bismuth layer structures [9] and PZT ceramics with perovskite structures [10], where the relatively smaller niobium cations enter the B site location (in

ABO_3). Figure 2.20 shows a SEM photomicrograph of fracture surfaces of pure and Nb-modified BI-PT materials. Average grain sizes for pure BIPT ceramics were found to be ~ 2 μm, while they were less than 1 μm for the modified counterpart, implying the niobium additive functioned as a grain growth inhibitor [10]. It was observed from Figure 2.20 that the pure BI-PT material shows a very clear inter-granular fracture, while the modified one exhibits a more trans-granular behavior (Figure 2.20).

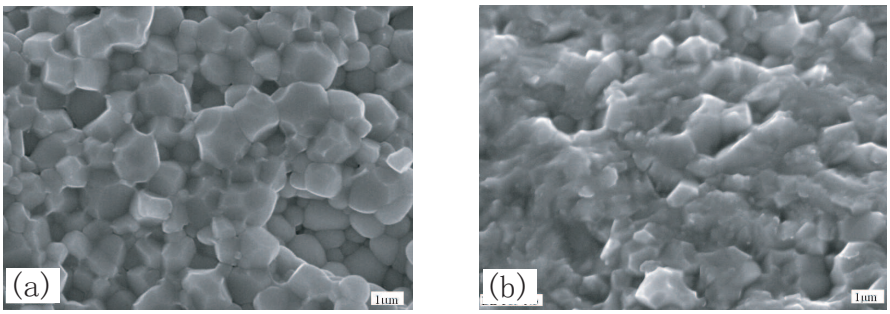

Fig 2.20: SEM images for pure (a) and niobium modified (b) 0.15$BiInO_3$-0.85$PbTiO_3$.

The room temperature dielectric constant increased for modified composition with $x = 0.20$ when compared to the pure counterpart (as listed in Table 2.3), while the loss was found to decrease significantly. The T_C of pure 0.20$BiInO_3$-0.80$PbTiO_3$ ceramic was 582°C, much higher than the T_C of the end member PT (∼490°C). This phenomenon was observed in other bismuth - containing systems, such as $BiScO_3$-$PbTiO_3$[12] and $Bi(Mg_{1/2}Ti_{1/2})O_3$-$PbTiO_3$ [12]. It is evident from Figure 2.21 (a) that the T_C shifts to lower temperatures with increasing niobium oxide concentration. The reduction in T_C with niobium content was found to be 20°C/ mol% Nb.

In Figure 2.21 (b), the dielectric loss for the pure 0.20$BiInO_3$-0.80$PbTiO_3$ ceramic was found to be 6% at room temperature, rising sharply with increasing temperature, reaching 20% at 600°C and 1 MHz frequency. For the Nb- modified 0.20$BiInO_3$-0.80$PbTiO_3$, the dielectric loss was found to be lower than 2% at room temperature, increasing to 7% at 600°C and 1 MHz frequency for 1 mol%, and only 3% for both 2 mol% and 3 mol% Nb-modified ceramics.

The pure 0.20$BiInO_3$-0.80$PbTiO_3$ ceramic could not be poled because of its high dielectric loss and low resistivity, while the Nb- modified materials could be poled owing to the high resistivity at elevated temperature. As listed in Table 2.3, the resistivities were measured at 400°C for the pure and Nb- modified 0.20$BiInO_3$-0.80$PbTiO_3$ samples, it was found that the resistivity increased with niobium addition. The resistivity of 23 × 10^6 Ω·cm for the 2 mol% dopant level was an order of magnitude higher than for pure 0.20$BiInO_3$-0.80$PbTiO_3$. The piezoelectric properties were characterized for the pure and modified 0.20$BiInO_3$-0.80$PbTiO_3$ ceramics 24 hours after the poling process, and the results are listed in Table I, in which the d_{33} of 0.20$BiInO_3$-0.80$PbTiO_3$ modified with 2 mol% niobium was found to be 36 pC/N, exhibiting better properties as compared to other compositions. 0.15$BiInO_3$-0.85$PbTiO_3$-1.5 mol% Nb was selected for further studies for the following reasons: first, $BiInO_3$-$PbTiO_3$ with 15% $BiInO_3$ showed a lower c/a ratio compared to that with 20% $BiInO_3$ [6], which makes it easier to pole; and secondly, ∼1.5 mol% niobium doping level was expected to show better piezoelectric behavior and T_C based on Table 2.3. The dielectric behavior for 0.15$BiInO_3$-0.85$PbTiO_3$-1.5 mol% Nb was measured as a function of temperature and is presented in Figure 2.22, in which the T_C was found to be 542°C, with a maximum dielectric constant of around 8,500. The dielectric loss was found to be 1.4% at room temperature, which increased to 6% at 600°C and 1 MHz frequency, similar to those values of modified 0.20$BiInO_3$-0.80$PbTiO_3$ materials (Figure 2.21 (b)). The dielectric constant showed a very stable dielectric temperature behavior before the Curie temperature.

The bipolar polarization hysteresis and butterfly strain curves were also measured at 1 Hz and 200 kV/cm, and are shown in Figure 2.23, in which the coercive field (E_C) was found to be 125 kV/cm and remnant polarization (P_r) was measured to be ∼26 C/cm^2. E_C was higher compared to the $BiScO_3$-PbTiO3 system (∼20-40 kV/cm) and PZT5A ceramics (∼15 kV/cm) owing to the enhanced T_C and large c/a ratio, improving domain stability under high mechanical and electrical stresses, important for high power devices. The electromechanical coupling factors, piezoelectric coefficients, dielectric constant and resistivity of modified 0.15$BiInO_3$-0.85$PbTiO_3$ were measured and the results are listed in

Table 2.4 and compared to tetragonal PT ceramic, in which it is apparent that the modified 0.15$BiInO_3$-0.85$PbTiO_3$ material shows better piezoelectric and dielectric properties, with much higher T_C and resistivity. Figure 2.24 presents the temperature dependence of the coupling factors (k_{15} and k_p) and piezoelectric coefficients d_{15}. It was found that the coupling factors remained almost constant until 520°C, then dropped rapidly as the temperature approached T_C at ~542°C, while the piezoelectric coefficient d_{15} increased from 85 pC/N at room temperature to 320 pC/N at 520°C, expanding the temperature usage range significantly compared to PZT and BSPT systems.

2.3 Chapter Conclusions

The solubility limit of BI in xBI-$(1-x)$PT was $x = 0.25$. Curie temperature and lattice distortion increased rapidly with x up to near-saturation at $x = 0.15$ with a corresponding Curie temperature of 581°C. In mixed oxide powders, Bi_2O_3 particles fused and reacted with the other batch constituents to form liquid phase, from which ~ 5 μm tetragonal perovskite cubes precipitated. Upon two-step firing, densities of 94.7% of TD were obtained. Sol-gel fabrication yielded similar results with respect to solubility limit and Curie temperatures. After two-step firing of calcined nano-sized sol-gel powders, tetragonal perovskite microstructures of as high as 98.2% of TD were formed. Pure $BiInO_3$-$PbTiO_3$ materials with a tetragonal perovskite phase (BI = 15% and 20%) could not be poled due to large c/a ratios, high dielectric losses and low electrical resistivities at elevated temperatures. Niobium-modified $BiInO_3$-$PbTiO_3$ compositions greatly decreased the dielectric loss and increased the resistivity, allowing the sample to be poled. T_C shifted to lower temperature by 20°C/ mol% niobium. 0.15$BiInO_3$-0.85$PbTiO_3$-1.5 mol% Nb was found to possess good piezoelectric coefficients with d_{33} around 60 pC/N and d_{15} of 85 pC/N. This, together with a large E_C of 125 kV/cm and a high T_C of 542°C, makes the Nb- modified 0.15$BiInO_3$-0.85$PbTiO_3$ composition a candidate for sensing applications at elevated temperatures.

2.4 References

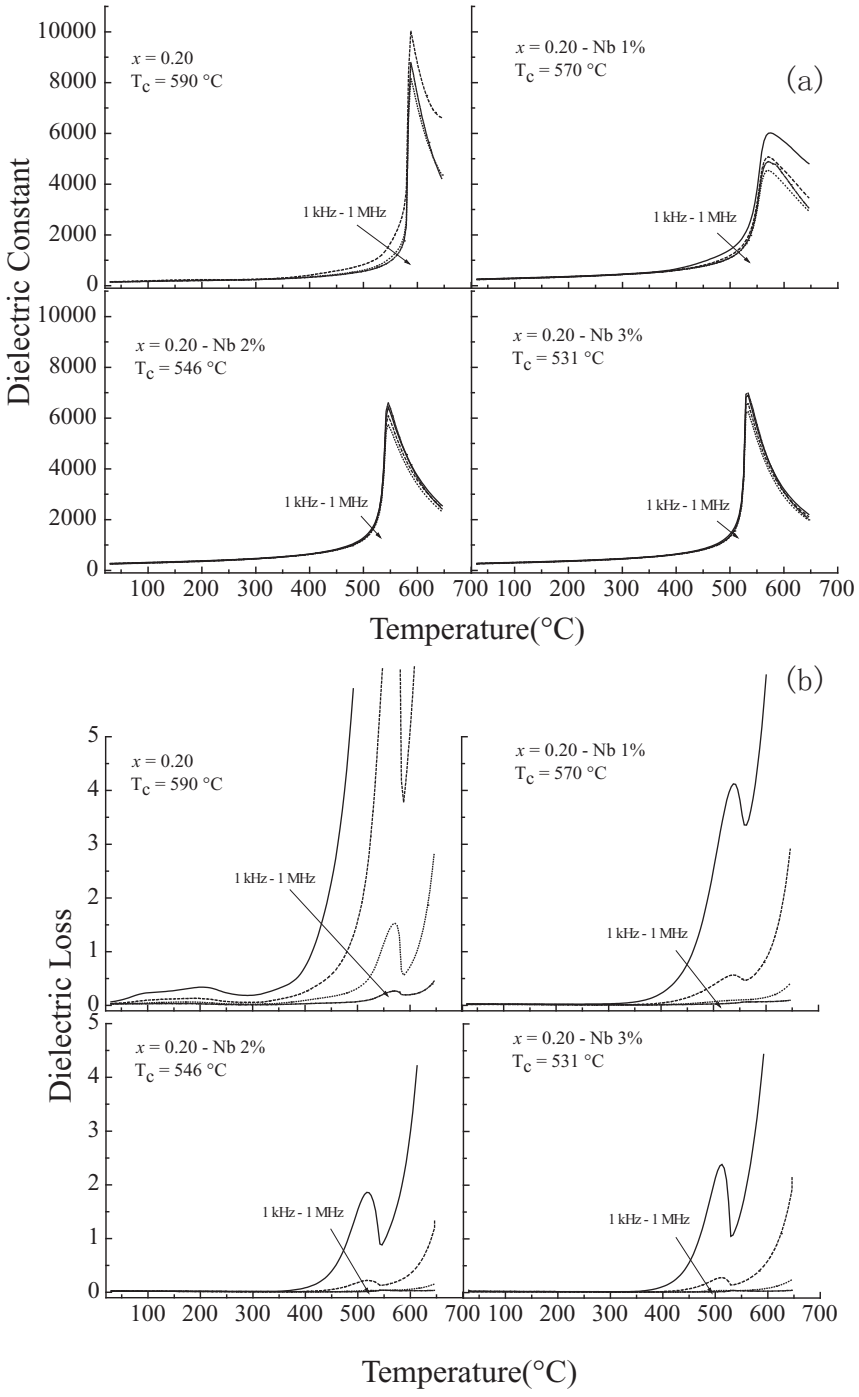

Fig 2.21: Dielectric constant (a) and dielectric loss (b) as a function of temperature and frequency for pure and niobium-modified $0.20BiInO_3$-$0.80PbTiO_3$ ceramics.

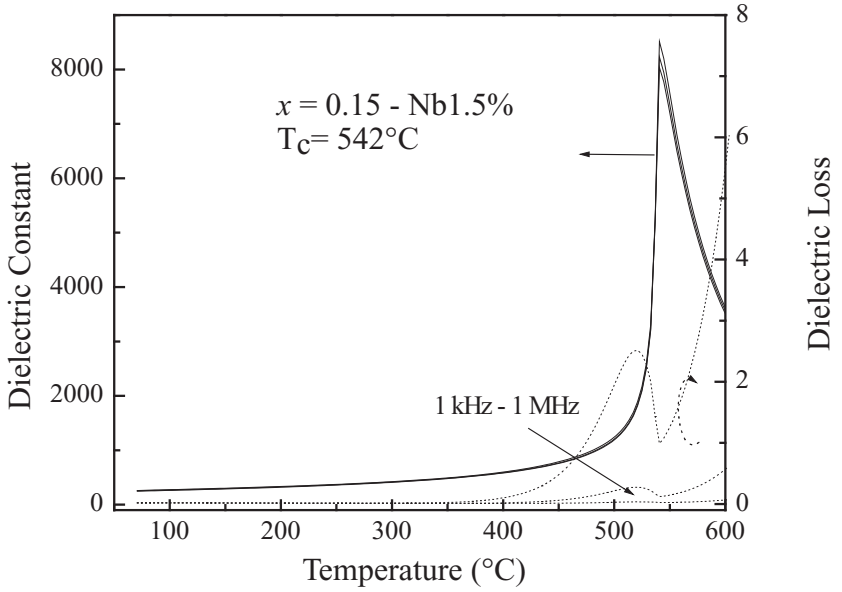

Fig 2.22: Dielectric constant and dielectric loss as a function of temperature and frequency for 1.5 mol% niobium- modified $0.15BiInO_3$-$0.85PbTiO_3$.

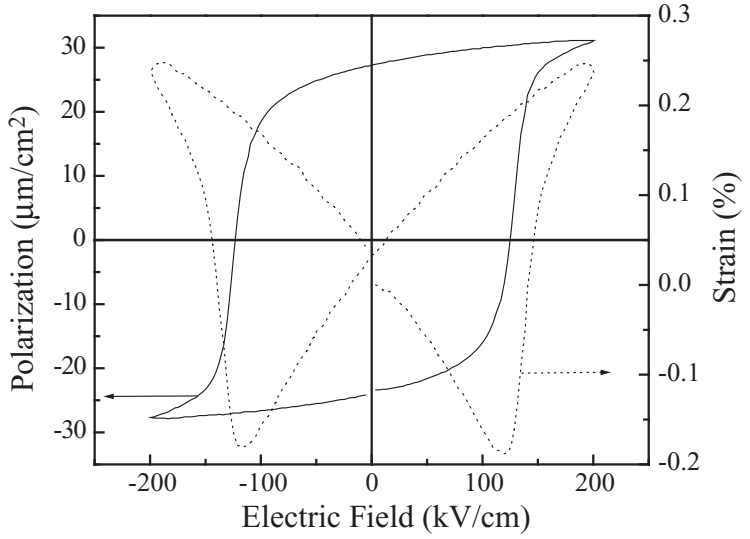

Fig 2.23: Bipolar polarization and strain versus electric field measured at 1 Hz and 200 kV/cm for 1.5 mol% niobium- modified $0.15BiInO_3$-$0.85PbTiO_3$.

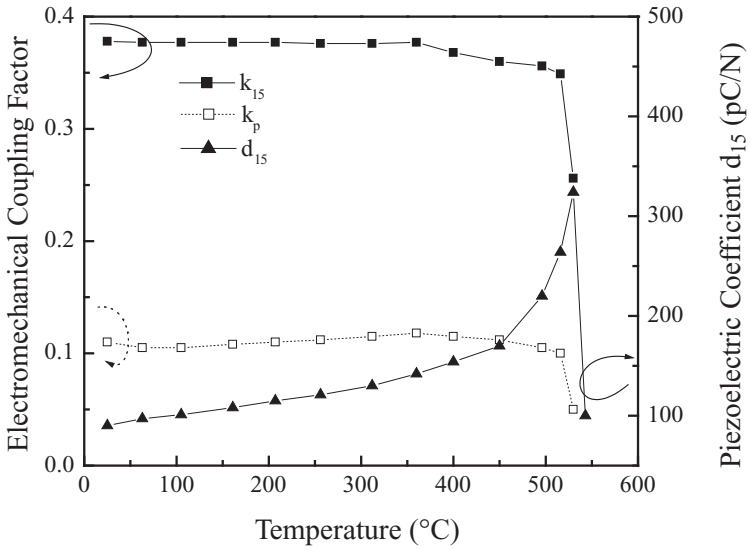

Fig 2.24: Electromechanical coupling factors k_{15} and k_p and piezoelectric coefficient d_{15} as a function of temperature for 1.5 mol% niobium- modified $0.15BiInO_3$-$0.85PbTiO_3$.

Tab 2.3: Dielectric and piezoelectric properties of pure and modified tetragonal $0.20BiInO_3$-$0.80PbTiO_3$.

Material	K_{33}^T	Loss	T_C (°C)	$d_{33}(pC/N)$	k_p	k_t	Resistivity at 400°C (Ω·cm)
$0.20BiInO_3$-$0.80PbTiO_3$	160	0.06	582	/	/	/	1×10^6
$0.20BiInO_3$-$0.80PbTiO_3$ - 1% Nb	250	0.018	570	18	4.6%	/	11×10^6
$0.20BiInO_3$-$0.80PbTiO_3$ - 2% Nb	255	0.016	550	36	10%	28%	23×10^6
$0.20BiInO_3$-$0.80PbTiO_3$ - 3% Nb	270	0.011	531	30	7%	40%	20×10^6

Tab 2.4: Dielectric and piezoelectric properties of $0.15BiInO_3$-$0.85PbTiO_3$- 1.5 mol% Nb (0.15BI-PT with Nb), compared to tetragonal perovskite $PbTiO_3$

Material	K_{33}^T	T_C (°C)	k_p	k_t	$d_{33}(pC/N)$	k_{15}	$d_{15}(pC/N)$	Resistivity at 400°C (Ω·cm)
0.15BI-PT with Nb	250	542	11%	38%	60	38%	85	26×10^6
$PbTiO_3$	190	470	/	30%	56	/	/	0.2×10^6

REFERENCES

[1] Private communication, TRS Ceramics, State College, PA, (2003).

[2] B. D. Cullity, *Elements of X-Ray Diffraction*, 2nd Ed., Addison Wesley, Reading, MA, (1978).

[3] E. M. Levin, C. R. Robbins, and H. F. McMurdie, *Phase Diagrams for Ceramists*, American Ceramic Society, Westerville, OH, (1964).

[4] Xu. Y. *Ferroelectric Materials and Their Applications.* North-Holland, (1991).

[5] *IEEE Std on Piezoelectricity*, ANSI/IEE Std. 176 (1987).

[6] R. R. Duan, R. F. Speyer, E. Alberta and T. R. Shrout, "High Curie Temperature Perovskite $BiInO_3$-$PbTiO_3$ Ceramics," *Journal of Materials Research*, **19** 2185 (2004).

[7] Y. Yamashita, K. Harada, Y. Hosono, S. Natsume and N. Ichinose, "Effects of B-site ions on the electromechanical coupling factors of $Pb(B'B")O_3$-$PbTiO_3$ piezoelectric materials," *Japanese Journal of Applied Physics*, **37** 5288 (1998).

[8] *Electrical Measurement Method for Piezoelectric Ceramic Elements*, EMAS-6100 (Standard of Electronic Materials Manufacture Association Japan), (1993).

[9] L. Zhang, R. Chu, S. Zhao, G. Li and Q. Yin, "Microsturcture and Electrical Properties of Niobium Doped $Bi_4Ti_3O_{12}$ Layer-structured Piezoelectric Ceramics," *Materials Science and Engineering B*, **116** 99 (2005).

[10] B. Jaffe, W. R. Cook, H. Jaffe, *Piezoelectric Ceramics*, Academic Press, New York, (1971).

[11] R. Eitel, C. Randall, T. Shrout and S. Park, "Preparation and Characterization of High temperature Perovskite Ferroelectrics in the Solid Solution $(1-x)BiScO_3$-$xPbTiO_3$," *Japanese Journal of Applied Physics*, **41** 2099 (2002).

[12] C. A. Randall, R. E. Eitel, B. Jones, T. R. Shrout, D. I. Woodward and I. M. Reaney, "Investigation of a High T_C Piezoelectric System: $(1-x)Bi(Mg_{1/2}Ti_{1/2})O_3$-$x$PbTiO$_3$, *Journal of Applied Physics*, **95** 3633 (2004).

CHAPTER 3

Preparation and Characterization of xBiLaO$_3$-$(1-x)$PbTiO$_3$ Ceramics with Multiple Dielectric Anomalies[0]

3.1 Experimental Procedure

Powder mixtures of xBiLaO$_3$-$(1-x)$PbTiO$_3$, with x values from 0 to 0.225 in steps of 0.025 were prepared by ball-milling PbO, Bi_2O_3, La_2O_3 and TiO_2 in the anatase form (all from Alpha Aesar, Ward Hill, MA) at room temperature in plastic jars for 4 h in ethanol, using 8 mm diameter partially stabilized zirconia milling media. All particles were specified by the supplier as < 4.5 μm. Additional intermediate compositions were also prepared to confirm observed trends. An additional 1 mol% PbO was added to ensure a Pb-rich atmosphere during firing. Each slurry was then dried for ∼8 h at 90°C. The as-dried mixture was ground using an alumina mortar and pestle, and passed through an 80-mesh sieve to eliminate large particle lumps. The resulting powder was calcined in covered MgO crucibles at 1000°C for 5 h. Heating rates were 6°C/min and cooling occurred in the furnace with no power applied to the heating elements. Additional loose powder of the same composition as the pellets was placed around the pressed pellets in the crucible to create an overpressure of the volatile constituents.

Calcined powders were then used to form dense sintered compacts. These were ground using a mortar and pestle, the resulting powders were passed through an 80-mesh sieve, and then pressed at ∼150 MPa into cylindrical pellets of 15 mm in diameter and ∼2.5 mm in height. These green bodies were then fired in covered MgO crucibles with surrounding powder of the same composition, heating at 8°C/min to 1150 ($0.025 \leq x \leq 0.100$), 1175

[0]Submitted to *Journal of Materials Research*

($0.125 \leq x \leq 0.150$), or 1200°C ($0.175 \leq x \leq 0.225$), soaking for 2.5 h. All of these fired specimens had relative densities in excess of 90%. These firing temperatures were chosen from a matrix of firing temperatures (1125-1200°C) as those which resulted in the most phase-pure specimens.

To extract impurity phases, a sintered pellet of $x = 0.10$ was ground using an alumina mortar and pestle. The powder was placed in a beaker with diluted nitric acid (0.05 mol/L). The mixture ratio of 1 g of powder to 100 ml nitric acid was stirred using a glass rod. After allowing the powder to settle to the bottom of the beaker, the nitric acid was decanted. The remaining powder was then washed 5 times with deionized water before being placed into a drying oven.

Phase analyses of heat-treated and crushed (using a mortar and pestle) compositions were performed by powder X-ray diffraction (XRD, Phillips X'Pert PRO Alpha-1) using CuKα1 radiation at a scanning speed of 0.008°per step with one step per 15 seconds. Lattice parameters for the tetragonal perovskite-structured phase were determined using the Jade 7.0 (Materials Data, Inc., Livermore, CA). All peaks (minus those of impurity phases) were used in the calculation of a and c lattice parameters. This calculation used numerical optimization based on the least-squares criterion. Standard deviations of lattice parameters from each (hkl) peak relative to the optimized mean values were the basis for error bars.

Curie temperatures were identified using differential scanning calorimetry (DSC, DSC cell from TA Instruments, New Castle, DE, with an interface by Innovative Thermal Systems, Atlanta, GA) endotherms, under heating rates of 12°C/min. Approximately equal volumes of material were evaluated for each DSC scan by tap-filling platinum DSC sample pans. Densities of sintered specimens were determined using Archimedes method. Microstructure was characterized using scanning electron microscopy (SEM, Model S-800, Hitachi High Technologies, Tokyo, Japan, with a Energy Dispersive Spectrometer, EDS, Thermo Noran, Middleton, WI, and Model 1530 SEM, LEO Electron Microscopy, Inc., Oberkochen, Germany).

Dielectric properties as a function of temperature were measured from 1 kHz to 100 kHz, using a multi-frequency LCR meter (Hewlett Packard 4284A, Agilent Technologies,

Inc., Palo Alto, CA) over the temperature range from room temperature to 700°C in 5°C increments. Disk samples were prepared for dielectric measurements by grinding to ∼1.5 mm in thickness and electroding on the parallel faces with a silver paste (DuPont 6160), with subsequent firing at 750°C.

3.2 Results

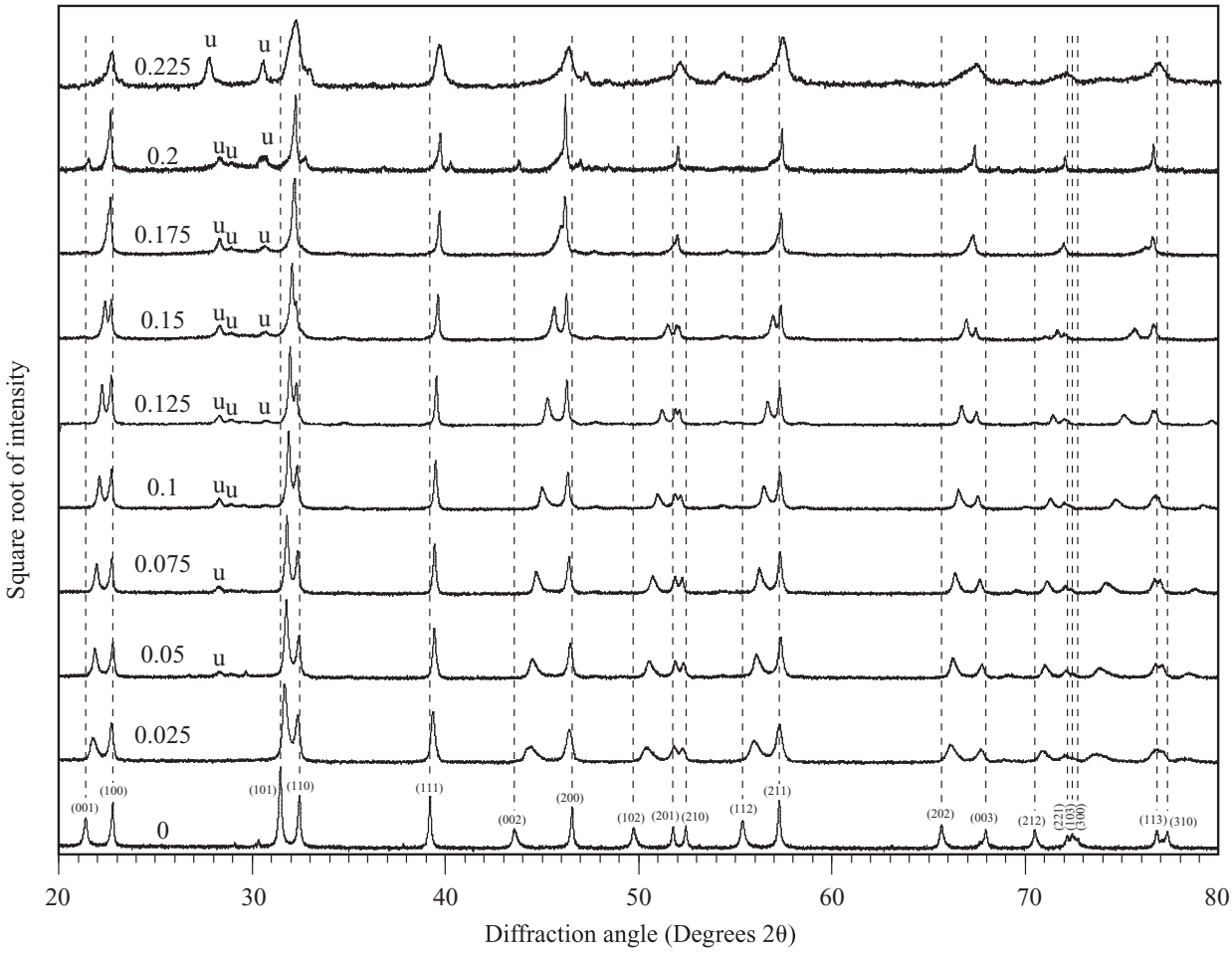

Fig 3.1: XRD patterns of xBiLaO$_3$-$(1-x)$PbTiO$_3$ compositions of varying x. Dashed vertical lines and (hkl) indicies correspond to PbTiO$_3$ (ICDD: 40-0099). "u" indicates an unidentified phase.

Figure 3.1 shows that phase pure perovskite-structured solid solutions were obtained for compositions with $x < 0.05$, while trace amounts of impurities were detected for compositions of higher x up to $x = 0.200$. The impurity concentration increased precipitously at $x = 0.225$. Figure 3.2 shows that the a lattice parameter generally increased and the

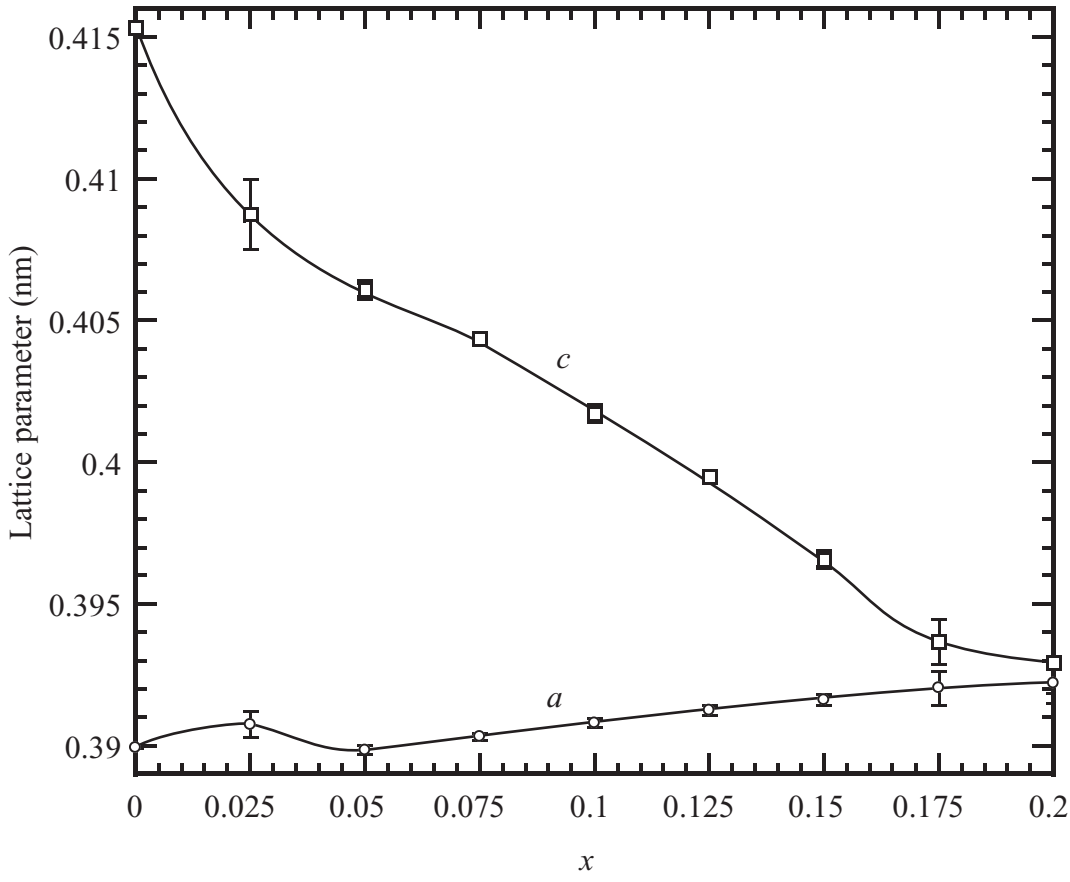

Fig 3.2: Calculated c and a lattice parameters for $x\mathrm{BiLaO_3}$-$(1-x)\mathrm{PbTiO_3}$ compositions of varying x.

c lattice parameter decreased with increasing x. These values reached near-equivalence at $x = 0.200$.

Figure 3.3 shows tetragonal lattice parameters merging to a single cubic lattice parameter at 300°C for $x = 0.10$. Figure 3.4 indicates there are no apparent structural changes occurring in the temperature range 550-650°C. Based on hot-stage XRD, Figure 3.5 shows a convergence of c and a lattice parameters to a single (cubic) lattice parameter at ∼400°C for $x = 0.05$ and ∼300°C for $x = 0.10$.

Figure 3.6 shows one or two DSC endotherms for various compositions. The lower temperature endotherm onset decreased with increasing x. For $x > 0.05$, a second, higher temperature endotherm appeared, whose position also decreased (less rapidly) with increasing x. Figure 3.7 shows the variation of dielectric constant of samples of varying x with

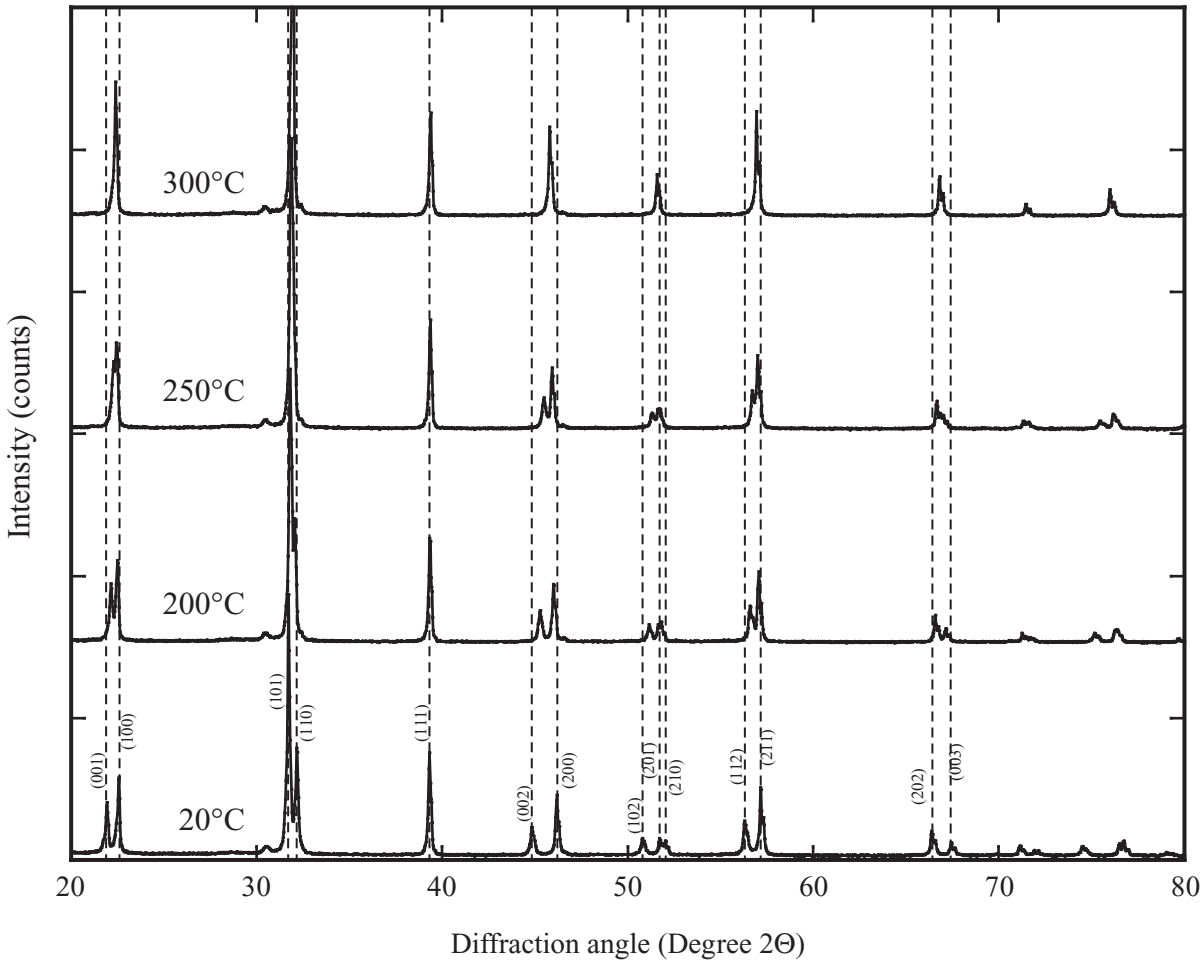

Fig 3.3: Hot-stage XRD traces of $x = 0.10$ over the range 20-300°C.

temperature. Figure 3.8 compares the peaks of the dielectric constants with the onsets of the DSC endotherms. Not all specimens evaluated by DSC were evaluated for their dielectric constant behavior with temperature.

3.3 Discussion

With increasing $BiLaO_3$ substitution for $PbTiO_3$, that is increasing x, the tetragonal distortion decreased as if to form a morphotropic phase boundary. However, the perovskite phase appears to become saturated with substituting cations above approximately $x = 0.20$; at $x = 0.225$, the concentration of impurity phases increases sharply (Figure 3.1).

For pure $PbTiO_3$, the endotherm onset at 495°C matches with the literature value for the Curie temperature of this compound [1]. Substitution of $BiLaO_3$ decreases this

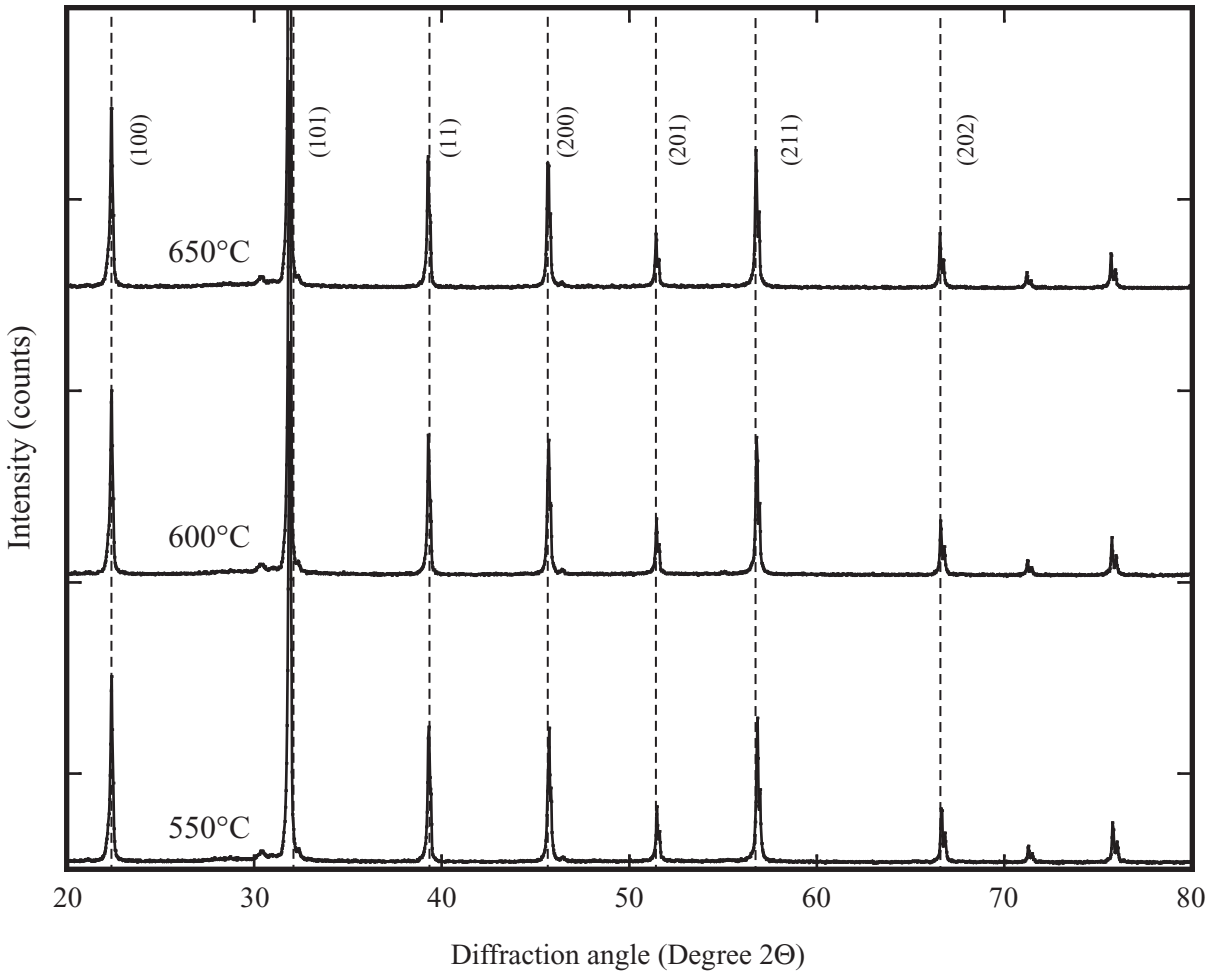

Fig 3.4: Hot-stage XRD traces of $x = 0.10$ over the range 550-650°C.

Curie temperature. The intensity of these endotherms decreases with increasing x since the tetragonal distortion at room temperature is less extensive with increasing x.

For $x = 0.05$ the Curie transformation from the ferroelectric tetragonal symmetry to the seemingly paraelectric cubic phase at 400°C is well-illustrated in Figure 3.5, and corresponds well to the DSC endotherm onset at 400°C (Figure 3.6) and dielectric anomaly peak at 430°C (Figure 3.7). This is similarly consistent for $x = 0.10$, though the convergence of c and a lattice parameters at 300°C in Figure 3.5 is a result of interpolation.

Starting at $x = 0.05$, a higher temperature endotherm appears (onset at 620°C for $x = 0.05$), which decreases in temperature slightly with increasing x. The intensity of this endotherm steps up significantly for $x \geq 0.100$. Corresponding to these endotherms are

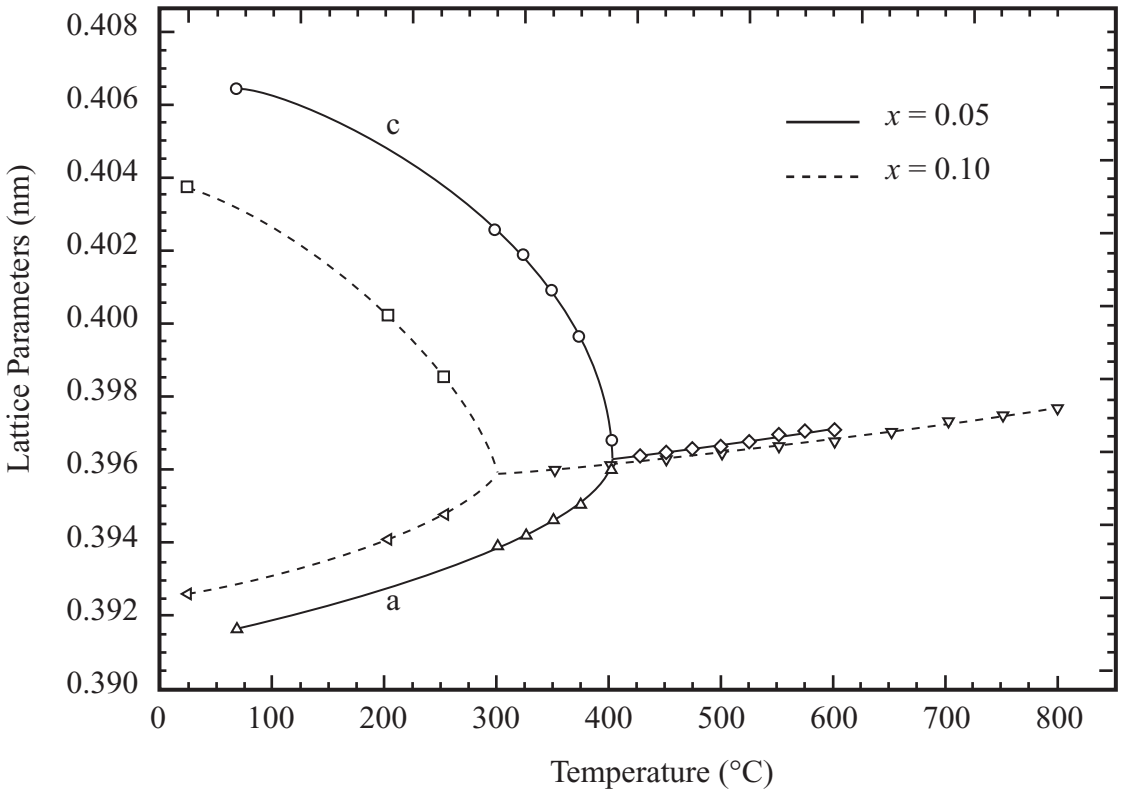

Fig 3.5: Lattice constants determined from hot-stage X-ray diffraction for $x = 0.050$ and $x = 0.100$. Tetragonal and cubic lattice parameters were both determined for low and high temperatures.

dielectric anomaly peaks (Figure 3.7), which show the same compositional dependence of their temperature values as the DSC onsets (Figure 3.8). However, there is no indication of any structural change corresponding to these thermal and dielectric signatures. Using $x = 0.10$ as example, hot-stage x-ray diffraction studies show the clear tetragonal to cubic change for the 300°C DSC endotherm onset (Figures 3.3 and 3.5), but no structural change for the 605°C DSC endotherm onset (Figure 3.4). Hot stage XRD and DSC traces for $x = 0.10$ were performed on the nitric acid-washed powder (phase-pure by XRD at room temperature) to ensure that the endotherm was not related with the unidentified impurity phases.

Dielectric anomalies in a class of dielectrics called "relaxors" occur without any structural transformation indicated by XRD [2]. This behavior has been observed in ternary oxide perovskites, e.g. $Pb(Mg_{1/3}Nb_{2/3})O_3$, or PMN. These dielectric anomaly peaks are

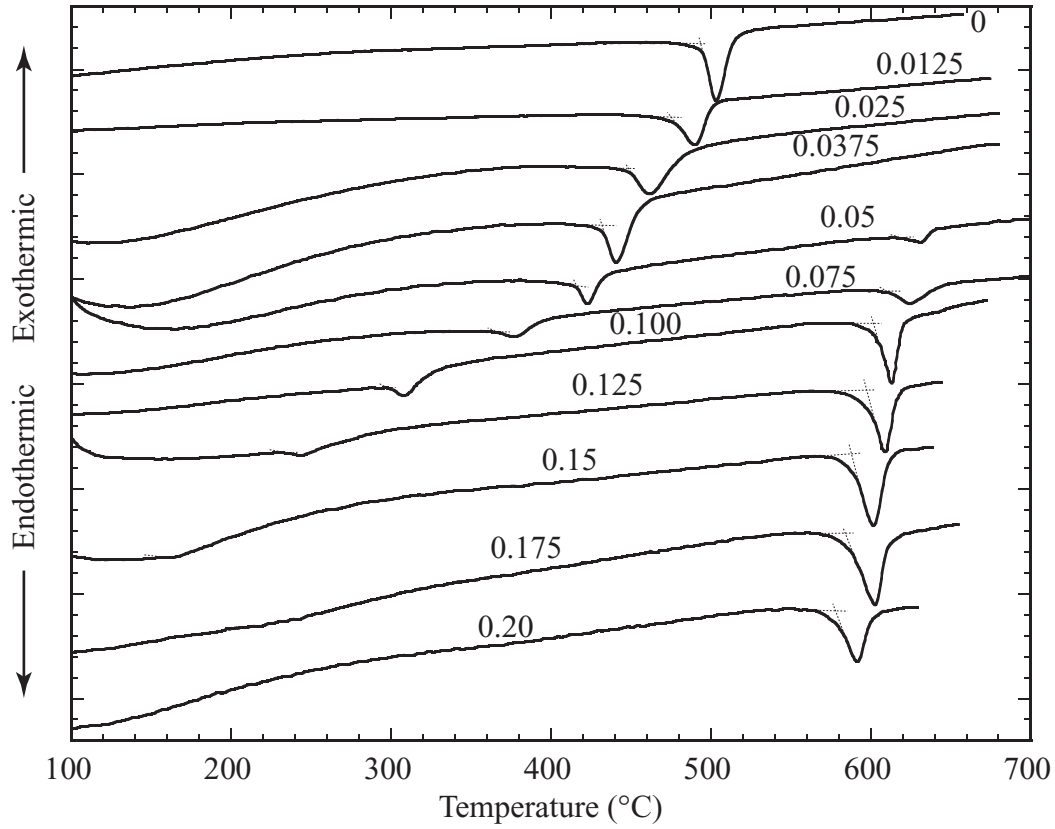

Fig 3.6: DSC traces of various compositions under a heating rate of 12°C/min. The numbers in the figure legend correspond to values of x.

comparatively broad, the peak position is frequency dependent and the hysteresis gradually closes as temperature is raised toward the Curie temperature. Ferroelectricity in these materials has been argued to be based on heterogenous distribution of B-site cations causing lattice distortions at a scale too fine for detection using standard XRD techniques.

The extent to which the xBiLaO$_3$-(1−x)PbTiO$_3$ shows all the characteristics of a relaxor ferroelectric remains to be further explored. The dielectric anomaly peaks are broad, but the hysteresis behavior and shift in the high-temperature dielectric anomaly peak could not be analyzed due to the increased conductivity of these compositions under stronger electric fields and higher temperatures. Regardless, the argument used for relaxor ferroelectrics, i.e. heterogeneous distribution of B-site cations, is a plausible explanation for the observed ferroelectric behavior at temperatures above the first dielectric anomalies for $x \geq 0.05$. The higher temperature endotherms/dielectric anomalies would correspond to randomization of

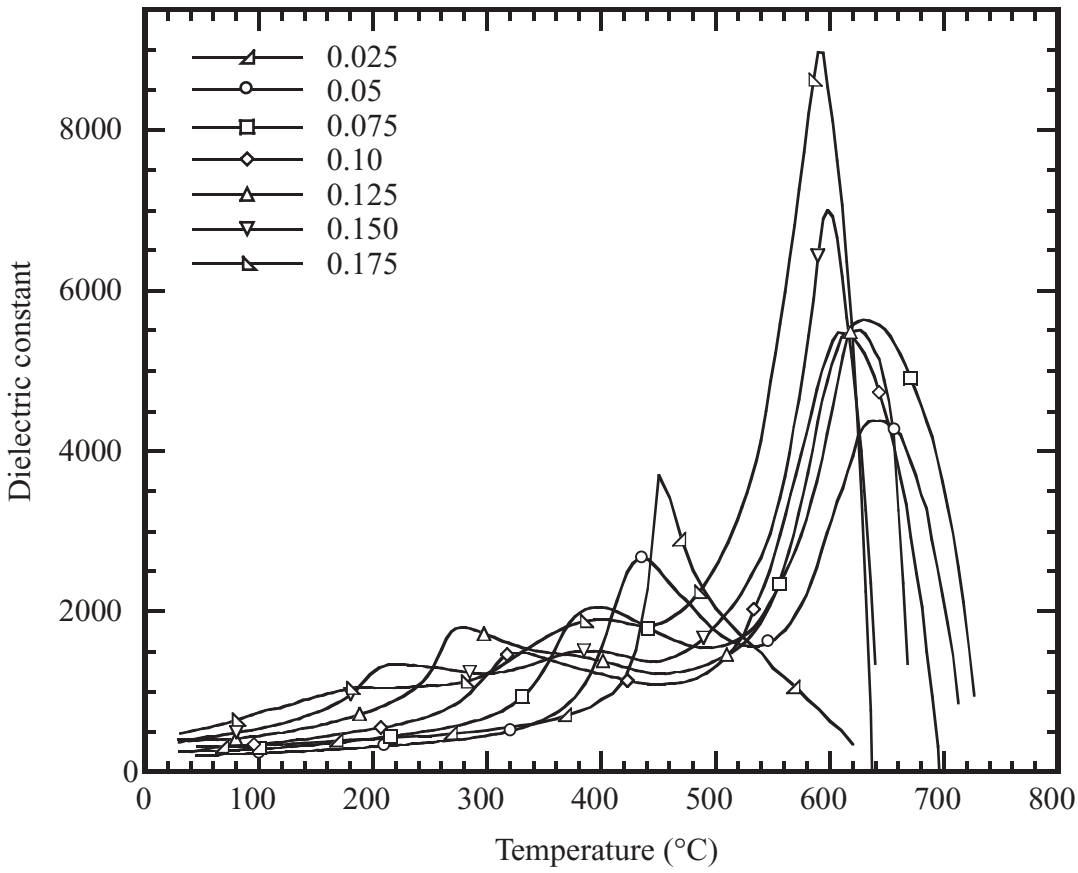

Fig 3.7: Dielectric constant plots as a function of temperature. The numbers in the figure legend correspond to values of x. Data markers are for curve identification and do not represent data points.

B-site cations in the case of a ferroelectric to paraelectric transformation, or correspond to a change in the nature of segregation of these B-site cations for a ferroelectric to ferroelectric transformation.

3.4 Chapter Conclusions

As $BiLaO_3$ is added to $PbTiO_3$, a point is reached ($x = 0.05$ for xBiLaO3-$(1-x)$$PbTiO_3$) in which two dielectric anomalies are observed. At lower temperatures (160-495°C), a normal tetragonal to cubic Curie-like transformation is demonstrated. At higher temperatures (∼600°C) a second transformation occurs with no structural changes indicated by x-ray diffraction. This transformation is akin to that which occurs in a relaxor ferrelectric, in which ferrolelectric behavior stems from a heterogenous distribution of B-site cations.

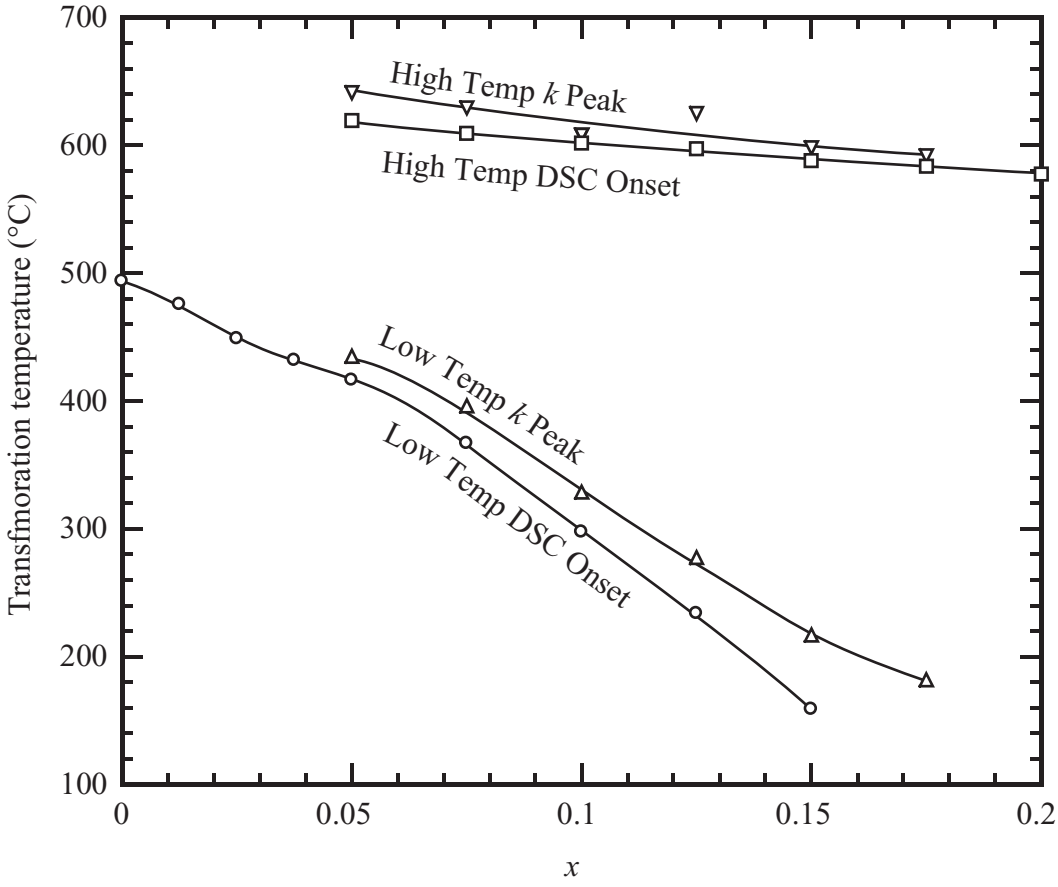

Fig 3.8: Curie temperatures determined from onsets of DSC endotherms and from peaks in dielectric constant versus data.

3.5 References

REFERENCES

[1] A. J. Moulson and J. M. Herbert, *Electroceramics*, 2nd Ed., John Wiley and Sons New York (2003).

[2] L. E. Cross, "Relaxor Ferroelectrics: An Overview," *Ferroelectrics*, **151** 305 (1994).

CHAPTER 4

Multiple dielectric peak response in ferroelectric perovskite solid solutions containing multiple B-site Cations

4.1 Preliminary

Perovskite structured ceramics based on morphotropic phase boundary (MPB) compositions such as $PbTi_{1-x}Zr_xO_3$, have come to dominate the world market for piezoelectric materials. During the past few years, extensive research [1]-[7] has been done on the studies in the simple Bi(B')O_3-$PbTiO_3$ and complex Bi(B'B")O_3-$PbTiO_3$ (B', B" refer to B-site cations) type perovskite families due to the discovery of high Curie temperature (T_C) and excellent piezoelectric properties in the xBiScO$_3$-$(1-x)$PbTiO$_3$ system by Eitel *et al* [1]. Some of these $PbTiO_3$-based solid solutions show a change of crystallographic symmetry as well as some other properties such as enhancement in dielectric and piezoelectric properties. For example, the xBi$(Mg_{1/2}Ti_{1/2})O_3$-$(1-x)$PbTiO$_3$ [2] system showed reduced tetragonality with increasing x, and enhanced dielectric and piezoelectric properties in the MPB region. On the other hand, increased tetragonality and higher Curie temperatures, when compared to $PbTiO_3$, were observed in the $BiInO_3$-$PbTiO_3$ [3] and Bi$(Zn_{1/2}Ti_{1/2})O_3$-$PbTiO_3$ systems [4]. The $BiFeO_3$-$PbTiO_3$ system was found to exhibit large spontaneous polarizations [5]. In the simulation studies of xBiScO$_3$-$(1-x)$PbTiO$_3$, first-principle studies have suggested that the onset of hybridization between Bi/Pb-6p and O-2p orbitals, the mechanism which is enhanced upon A-site substitution of Pb by Bi, influences the ferroelectric properties of Bi(B')O_3-$PbTiO_3$ systems [7]. However, considering the different behaviors of the mentioned Bi(B')O_3-$PbTiO_3$ solid solutions with various B-site substituted cations, the nature of the B-site substitution may also have played an important role.

For Pb-based ferroelectrics, the dielectric peak anomalous response is a well-known phenomenon and can be observed when measuring the dielectric constant with increasing temperature. The dielectric constant first rises up when the temperature approaches the Curie temperature. After it goes through the ferroelectric-paraelectric transformation, the dielectric constant drops beyond the Curie temperature, representing the loss of poled state because the dipoles become disordered as a result of thermal fluctuations [8]. The ferroelectric-paraelectric transformation is also accompanied by a crystal structure transformation from ferroelectric perovskite (such as tetragonal or rhombohedral) to paraelectric cubic [9].

Here an unusual dielectric phenomenon is observed in Bi(B'B"B"')O_3-$PbTiO_3$ perovskite specimens containing multiple B-site cations, which is different from common Pb-based ferroelectrics. Instead of observing one single dielectric peak, multiple dielectric anomalies were detected. The validity of the high temperature dielectric constant peak was further confirmed by Differential Scanning Calorimetry (DSC) measurements. The only previous report on the existence of multiple dielectric peaks was published in 1981 by Jang *et al* [10]. In this section, dielectric constant and DSC results are presented for the multiple A and B cation compositions shown in Table 4.1. A brief explanation for the multiple dielectric anomalies observed are discussed.

Tab 4.1: $PbTiO_3$ based solid solutions which were investigated.

Systems	A site cations	Possible B site cations	Abbreviations
$(BiInO_3)_{0.15}$-$(PbZr_{0.45}Ti_{0.55}O_3)_{0.85}$	Pb^{2+}, Bi^{3+}, In^{3+}	In^{3+}, Zr^{4+}, Ti^{4+}	BI-PZT
$(Bi_{0.35}La_{0.10}Sc_{0.25}(O_3)_{0.35})$-$(PbTiO_3)_{0.65}$	Pb^{2+}, Bi^{3+}, La^{3+}	La^{3+}, Sc^{3+}, Ti^{4+}	BLS-PT
$(Bi_{0.39}Sc_{0.39}(O_3)_{0.39})$-$(PbTiO_3)_{0.61}$	Pb^{2+}, Bi^{3+}	Sc^{3+}, Ti^{4+}	BS-PT
$(Bi_{0.40}Sc_{0.38}(O_3)_{0.39})$-$(PbTiO_3)_{0.61}$	Pb^{2+}, Bi^{3+}	Bi^{3+}, Sc^{3+}, Ti^{4+}	N-BS-PT

Samples for the solid solutions listed in Table 4.1 were prepared by conventional ceramic processing to form the compound oxides. Powder oxide batches of corresponding mixtures were milled at room temperature in plastic jars for 4 h in ethanol, using 8 mm diameter partially stabilized zirconia milling media. Each slurry was then dried for ∼6 h at 100°C. The as-dried mixture was ground using an alumina mortar and pestle, and passed through an

80-mesh sieve to eliminate large particle agglomerates. The resulting powders were calcined in covered MgO crucibles at 850°C for 2.5 h. The as-calcined powders were ground with a mortar and pestle, and calcined again at 900°C to 1000°C (depending on the compositions) for 2 h. Heating rates used were 7°C/min and cooling was allowed to occur in the furnace with no power applied to the heating elements. Calcined powders were then used to form dense sintered compacts. These were ground using mortar and pestle, the resulting powders were passed through an 80-mesh sieve, and then pressed at ∼150 MPa into cylindrical pellets of 15 mm in diameter and ∼2.5 mm in thickness. These green bodies were then fired in covered MgO crucibles with surrounding powder of the same composition, heating at 7°C/min up to a temperature between 1000°C and 1200°C depending on the composition and soaking for 2 to 4 h. Sintered pellets were either crushed for X-ray diffraction or polished and electroded with silver paste for dielectric measurement. Phase analysis of heat-treated and crushed compositions was performed by powder X-ray diffraction (XRD, Philips PW 1800 automated powder diffractometer) using CuKα radiation at a scanning 2θ range of 20°-80°. Transition temperatures were identified using differential scanning calorimetry endotherms (DSC, TA Instruments DSC cell with an Innovative Thermal Systems interface), under heating rates of 15°C/min. Relative densities of sintered specimens were determined using the Archimedes method. Dielectric properties as a function of temperature were measured using an impedance analyzer (HP 4192).

Figure 4.1 shows the typical ABO_3 perovskite structure, where the A sites are normally occupied by Pb^{2+} and Bi^{3+} and the B sites are normally occupied by Ti^{4+}, Zr^{4+} and Sc^{3+} [9].

Figure 4.2 shows the XRD patterns for the four compositions listed in Table 4.1. For all four compositions, perovskite structure with low symmetry unit cell derived from cubic prototype were identified. In each case, the low temperature ferroelectric phase is derived from the high temperature ideal cubic perovskite structure, the paraelectric phase. The lower symmetry phases, are identified by either {111} splitting, or {110} and {200} splitting as shown in the magnified views in Figure 4.2.

Figure 4.3 shows the dielectric constant at 1 kHz as a function of temperature for the

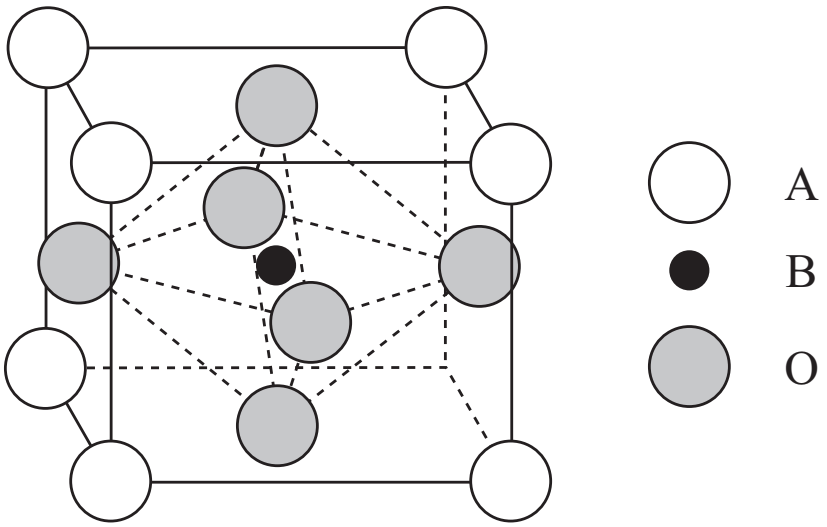

Fig 4.1: Typical unit cell of ABO_3 with Perovskite structure.

various compositions studied. It can be seen that all compositions except for the BS-PT exhibit more than one dielectric peak. For the BI-PZT specimen, a low-temperature peak appeared at 310°C and was followed by a high temperature peak at ∼600-610°C (Figure 4.3a). The BLS-PT specimen displays three peaks, one at ∼330°C, followed by one at 525°C and another at 615°C (Figure 4.3b). The peaks at 330°C and 615°C are related to the BL-PT [11], while the middle peak at 525°C is related to Sc^{3+} [12]. Figure 4.3c is a direct comparison of stoichiometric BS-PT and nonstoichiometric N-BS-PT. The BS-PT specimen showed one single dielectric peak at 430°C while the N-BS-PT specimen showed not only the first dielectric constant maximum at 430°C which matched that of the BS-PT specimen, but also exhibited a second peak at 610°C.

A latent heat can be measured via DSC if the ferroelectric-to -paraelectric transition is first order [13]. Differential scanning calorimetry scans of the specimens in Figure 4.3 are shown in Figure 4.4. The endotherm onsets can be interpreted to be the transition temperatures [3]. The positions of the dielectric peaks in the BI-PZT specimen (Figure 4.3a) matched the endotherm positions in the DSC measurements shown in Figure 4.4a well. These endotherms imply that both transitions in the BI-PZT specimen are first order. For ferroelectrics, it has been known that the order of transition can be changed by application of a hydrostatic pressure [14] or by variation in chemical composition through ion

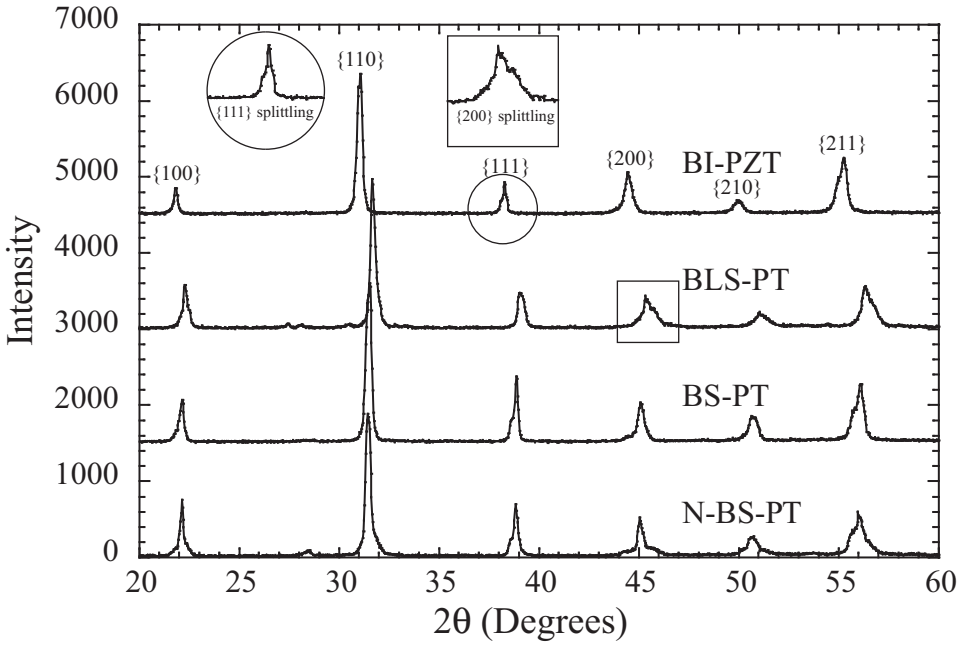

Fig 4.2: XRD patterns of different solid solution specimens investigated. Compositions are given in Table 4.1. The peaks are indexed with reference to the cubic {hkl}'s. The inset graphs highlight the characteristic splitting of the pseudocubic peaks for the given derivative lower symmetry phases.

substitution [15, 16].

For the BLS-PT specimen, a double endotherm was detected (one at 595°C, the other at 610°C) which is close to the temperature where the highest dielectric peak is observed. However, a latent heat was not detected for the transitions at 510°C nor at 330°C (Figure 4.3b). This implies that the transitions at 330°C and $\sim$ 510°C are second order (enthalpy is continuous through the transformation). Similarly, the ferroelectric-paraelectric transformation for the BS-PT (with 39 mol% Bi and Sc) specimen (Figure 4.3c) is a second order transformation [12], because no DSC endotherm was detected as shown in Figure 4.4c top. However, for the nonstoichiometric N-BS-PT specimen (with 40% Bi and 38% Sc), an endotherm at $\sim$610°C was detected (Figure 4.4c bottom).

Confirmation that the location and magnitude of the multiple dielectric peaks can be controlled by the ratio of the multiple cation compositions will be elaborated in subsequent section. The results on a series of BLS-PT specimens (where relative the Sc/La ratio varies) show systematic behavior running from that of pure BS-PT to pure BL-PT [17].

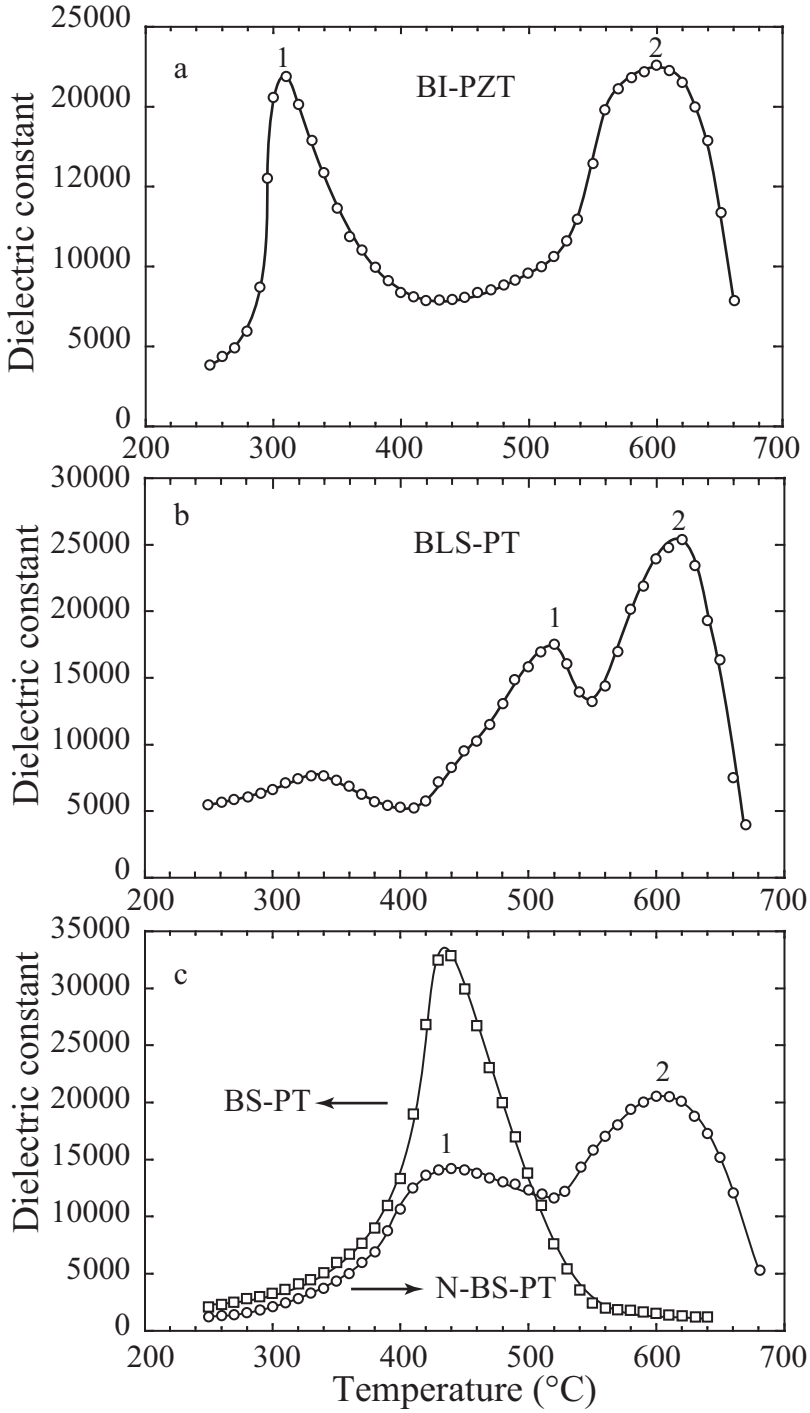

Fig 4.3: Dielectric constant at 1 kHz vs. temperature for differently doped PT specimens investigated.

To help understand the unusual behavior in the properties of the solid solutions presented in Figures 4.3 and 4.4, some well known solid solutions can be used as references. In the xPbZrO$_3$-$(1-x)$PbTiO$_3$ (PZT) system, the Curie temperature shifts to lower temperature with increasing Zr^{4+} substitution for Ti^{4+} (B-site). This implies that dipoles responsible for the dielectric anomaly of the xPbZrO$_3$-$(1-x)$PbTiO$_3$ system are a result of the combined effect of the substitutional Zr^{4+} and Ti^{4+} which give rise to a single Curie temperature whose position changes depending on the composition [9]. For simplicity, the dipoles in this PbTiO$_3$-based PZT solid solutions can be referred to as Zr^{4+}-related dipoles. Likewise, in the BS-PT systems, the substitution of Sc^{3+} into Ti^{4+} also forms Sc^{3+}-related dipoles. Depending on the amount of Sc^{3+} doping, the Curie temperature of the xBiScO$_3$-$(1-x)$PbTiO$_3$ system is seen to change [1].

A qualitative relationship between the tolerance factor and the transition temperature at the MPB in Bi(B'B")O$_3$-PbTiO$_3$ has been proposed by Eitel *et al* [1]. This relationship asserted that, in general, as the tolerance factor decreased, the transition temperature increased. The tolerance factor ($t = \dfrac{(R_A + R_O)}{\sqrt{2}(R_B + R_O)}$), is practically determined by the size of B-site cations in Bi(B'B")O$_3$-PbTiO$_3$, since the size of A-site substitution of Bi^{3+} is only slightly smaller than that of Pb^{2+}. For xPbZrO$_3$-$(1-x)$PbTiO$_3$ and xBiScO$_3$-$(1-x)$PbTiO$_3$ solid solutions, the transition temperatures are in the ~350-450°C range [18, 1], while for the xBiInO$_3$-$(1-x)$PbTiO$_3$ solid solution system the transition temperature is 582°C with $x = 0.15$ [3]. For the xBiLaO$_3$-$(1-x)$PbTiO$_3$ system even higher transition temperatures of ~600°C were measured (when $x > 0.05$) [11].

It is speculated that the reason the xBiInO$_3$-$(1-x)$PbTiO$_3$ and xBiLaO$_3$-$(1-x)$PbTiO$_3$ systems display high transition temperatures around 600°C is because of the small tolerance factor as the result of some In^{3+} and La^{3+} entering into the B-sites rather than the A-sites. It is reasonable to assume that when large cations such as In^{3+} (0.094 nm ionic radius) and La^{3+} (0.117 nm) or even Bi^{3+} (0.117 nm) are incorporated into the B-site, they would form dipole moments that are less easily affected by thermal fluctuations with increased temperature, as compared to smaller cations such as Sc^{3+} (0.0885 nm) or Zr^{4+} (0.086 nm).

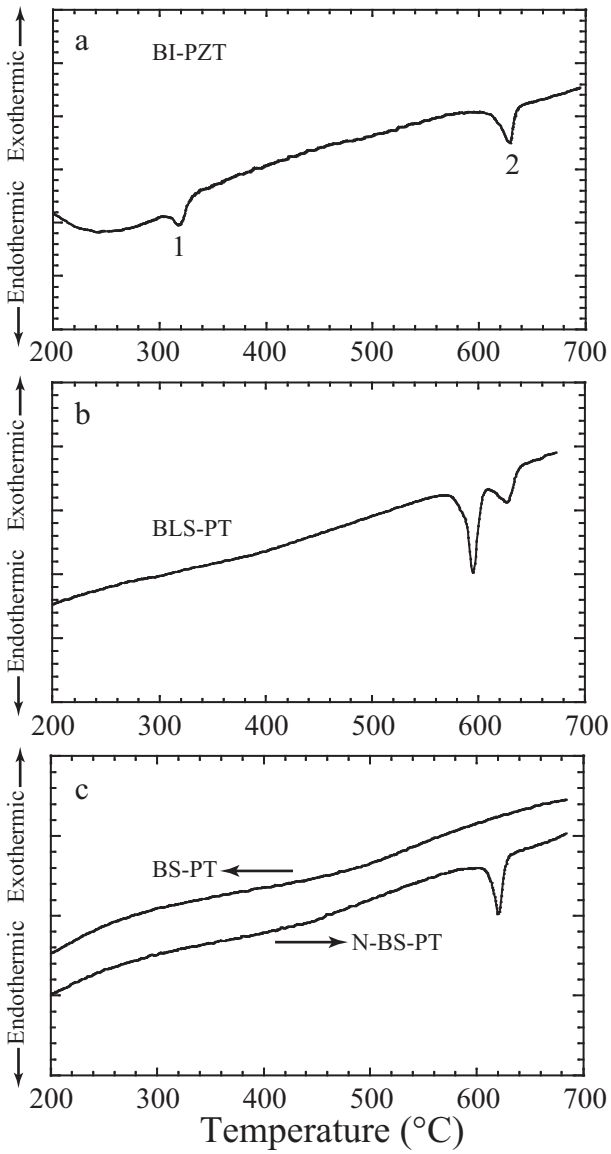

Fig 4.4: Differential scanning calorimetry scans of the specimens whose dielectric response are displayed in Figure 4.3

Therefore, the dielectric constant of the BI-PZT, BLS-PT and N-BS-PT systems can be viewed as a result of combined contributions from dipoles related to Zr^{4+} and In^{3+} (as in BI-PZT system), Sc^{3+} and La^{3+} (as in BLS-PT) and Sc^{3+} and Bi^{3+} (for the N-BS-PT systems) when they form solid solutions with $PbTiO_3$. In the N-BS-PT system, the 2 mol% (using Ti^{4+} as the frame of reference) difference between Bi^{3+} and Sc^{3+} was arbitrarily created to see if some large Bi^{3+} would enter the B-site to compensate for the lack of Sc^{3+} instead of creating B-site vacancies. The results showed that, compared to only one dielectric anomaly for BS-PT, the appearance of the second dielectric anomaly of the N-BS-PT supports the idea that the extra Bi^{3+} has taken the place of the missing Sc^{3+} in the B-site in the N-BS-PT specimen.

In summary, when the temperature is increased, dipoles related to the smaller cations Zr^{4+} or Sc^{3+} become thermally activated first and give rise to a dielectric anomaly at lower temperature. This causes the overall increase of dielectric constant (the low temperature dielectric constant peak) until thermal fluctuation by further increasing of temperature can randomize those dipoles. The dielectric constant then begins to decrease. This assumes that dipoles related to the large cations such as In^{3+}, La^{3+}, Bi^{3+} have not yet been activated so that the dielectric constant maximum observed at low temperatures (labeled 1) in Figure 4.3 in the temperature range of 310°C (BI-PZT), 510°C (BLS-PT) and 430°C (N-BS-PT) can be mostly attributed to dipoles related to Zr^{4+} or Sc^{3+}. With continued increasing of temperature to over 600°C, the dipoles related to large cations such as In^{3+}, La^{3+} and Bi^{3+} are then thermally activated. The overall dielectric constant rises up again and the high temperature dielectric peaks appear (labeled 2 in Figure 4.3). The source of the multiple dielectric peak behavior in these multiple cations compositions is therefore ascribed to possible B-site occupancy by the large cations In^{3+}, La^{3+} and Bi^{3+}, thus providing more experimental evidence that the transition temperatures in $PbTiO_3$ solid solutions with $Bi(B'B'')O_3$ are determined in great part by the sizes of the B-site cations as predicted by the relationship between tolerance factor and Curie temperature [1].

The previous section speculated that in a complex Bi(B'B"B"')O_3-$PbTiO_3$ system, the dipoles associated with certain doped B-site cations would behave independently at elevated temperatures. To provide further information for such a theory, a series of $Bi_{0.35}La_xSc_{0.35-x}(O_3)_{0.35}$-$(PbTiO_3)_{0.65}$ with different La/Sc ratio was designed. By varying the La/Sc ratio, the Sc/La related dipoles were expected to exhibit systematic temperature response with corresponding $BiScO_3$/$BiLaO_3$ concentrations as they are in the individual $BiScO_3$-$PbTiO_3$ and $BiLaO_3$-$PbTiO_3$ systems.

4.2 Experimental Procedure

Powder mixtures of $Bi_{0.35}La_xSc_{0.35-x}(O_3)_{0.35}$-$(PbTiO_3)_{0.65}$, with x values from 0.050 to 0.150 in steps of 0.025 were prepared by ball-milling PbO, Bi_2O_3, La_2O_3, TiO_2 (all from Alpha Aesar) and Sc_2O_3 (Pacific Industrial Development Corporation, Michigan). Milling was carried out at room temperature in plastic jars for 8 h in ethanol, using 8 mm diameter partially stabilized zirconia milling media. Each slurry was then dried for ∼12 h at 90°C. The as-dried mixture was ground using an alumina mortar and pestle, and passed through an 80-mesh sieve to eliminate large particle lumps. The resulting powder was calcined in covered MgO crucibles at 850°C for 2.5 h. The as-calcined powders were ground with a mortar and pestle, and calcined again at 1000°C for 4 h. Heating rates were 7°C/min and cooling occurred in the furnace with no power applied to the heating elements.

Calcined powders were then used to form dense sintered compacts. They were ground using a mortar and pestle, the resulting powders were passed through an 80-mesh sieve, and then pressed at ∼150 MPa into cylindrical pellets of 15 mm in diameter and ∼2.5 mm in height. These green bodies were then fired in covered MgO crucibles with surrounding powder of the same composition, heating at 7°C/min to 1150°C and soaking for 2 h. Sintered pellets were either crushed for X-ray diffraction or polished and electroded with silver paste for dielectric measurement.

Phase analyses of heat-treated and crushed (using a mortar and pestle) compositions were performed by powder X-ray diffraction (XRD) using CuKα1 radiation (Philips PW 1800 automated powder diffractometer). Transition temperatures were monitored using

differential scanning calorimetry endotherms (DSC, TA Instruments DSC cell with an Innovative Thermal Systems interface), under heating rates of 12°C/min. Relative densities of sintered specimens were determined using the Archimedes method. Dielectric properties as a function of temperature were measured using an impedance analyzer (HP 4192A) over the temperature range from room temperature to 700°C.

4.3 Results

Figure 4.5 shows XRD patterns of $Bi_{0.35}La_xSc_{0.35-x}(O_3)_{0.35}$-$(PbTiO_3)_{0.65}$ specimens, with x values from 0.050 to 0.150. Perovskite structured solid solutions were identified for all compositions, while trace amounts of an impurity phase were detected for $x = 0.100$, 0.125, and 0.150. All the compositions have structural symmetry close to r3m with a slight tetragonal distortion, which can be seen from the split of the (200) peak at $\sim 45°$ 2θ (circled peak in Figure 4.5). The peak split became less apparent as the x value increased, indicating structure went towards a pseudo-cubic structure.

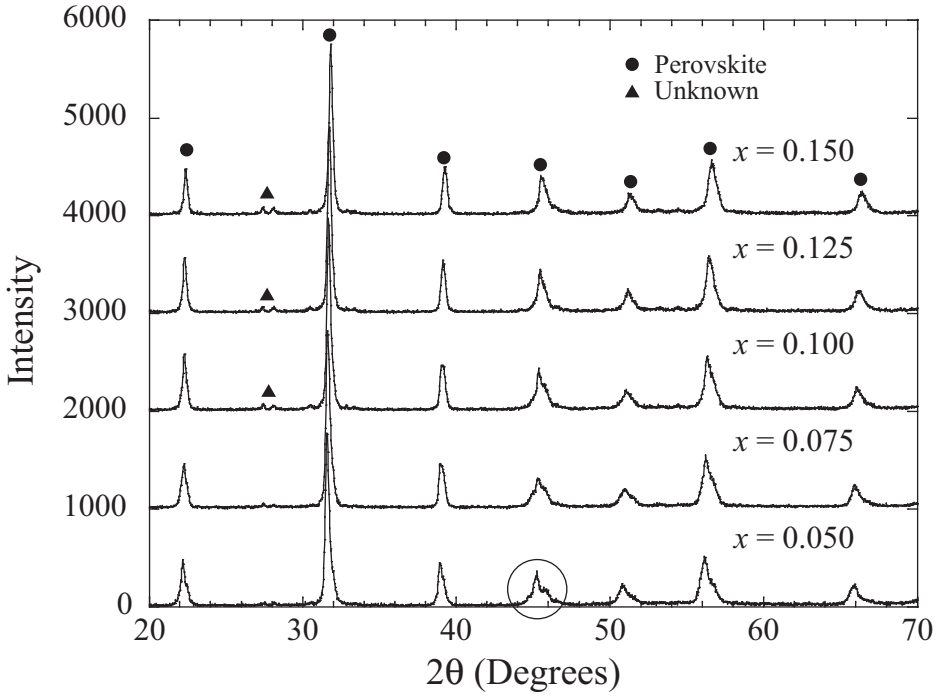

Fig 4.5: Overlayed XRD patterns of different compositions of the system $Bi_{0.35}La_xSc_{0.35-x}(O_3)_{0.35}$-$(PbTiO_3)_{0.65}$.

Figure 4.6 shows the dielectric constant response vs. temperature for the $Bi_{0.35}La_{0.10}Sc_{0.25}(O_3)_{0.35}$-$(PbTiO_3)_{0.65}$ specimen and the two simpler solid solutions, $(BiScO_3)_{0.25}$-$(PbTiO_3)_{0.75}$ and $(BiLaO_3)_{0.10}$-$(PbTiO_3)_{0.90}$. The five-cation specimen (displayed in Figure 4.6c)shows three maxima, at ∼330°C, 515°C and 620°C. For the $(BiScO_3)_{0.25}$-$(PbTiO_3)_{0.75}$ specimen (Figure 4.6a), a maximum formed at ∼510°C (shown for both 1 kHz and 10 kHz). They are at a similar position as the 515°C peak observed for the $Bi_{0.35}La_{0.10}Sc_{0.25}$-$(PbTiO_3)_{0.65}$ specimen. The dielectric constant maximum at 620°C for the $(BiLaO_3)_{0.10}$-$(PbTiO_3)_{0.90}$ sample displayed in Figure 4.6b (taken at 10 kHz) matches the highest temperature peak detected in the five-cation specimen, and also displays a low temperature peak at ∼320°C [1].

Figure 4.7 presents the DSC measurements of the three compositions whose dielectric behaviors are displayed in Figure 4.6. The endotherm onsets are attributed to be the Curie temperatures [3]. Based on DSC endotherms, T_c = 515°C for $(BiScO_3)_{0.25}$-$(PbTiO_3)_{0.75}$. Two endotherms at 315°C and 605°C were detected for $(BiLaO_3)_{0.10}$-$(PbTiO_3)_{0.90}$. Two consecutive endotherms were detected at 595°C and 630°C for the $Bi_{0.35}La_{0.10}Sc_{0.25}(O_3)_{0.35}$-$(PbTiO_3)_{0.65}$ specimen.

Figure 4.8 shows the dielectric constant as a function of temperature for various $Bi_{0.35}La_xSc_{0.35-x}(O_3)_{0.35}$-$(PbTiO_3)_{0.65}$ compositions. It can be seen that all compositions exhibit multiple dielectric peak behavior. For x values of 0.05 and 0.075 (Figure 4.8a), low-temperature peaks at 390-400°C (labeled as peak 1) were followed by high temperature peaks at ∼640°. For higher x (Figure 4.8b), the low-temperature dielectric peak shifted to higher temperature (520-530°C), while the position of the higher-temperature (labeled as peak 2) dielectric peak decreased slightly (600-620°C).

Figure 4.9 displays the DSC measurements of specimens in Figure 4.8. Two DSC endotherms were detected for all five compositions with the first peak appearing at 595-610°C and the second peak at 630-640°C.

[1] Because of too high a conductivity at elevated temperature, no satisfactory data was obtained at 1 kHz for the $(BiLaO_3)_{0.10}$-$(PbTiO_3)_{0.90}$ specimen.

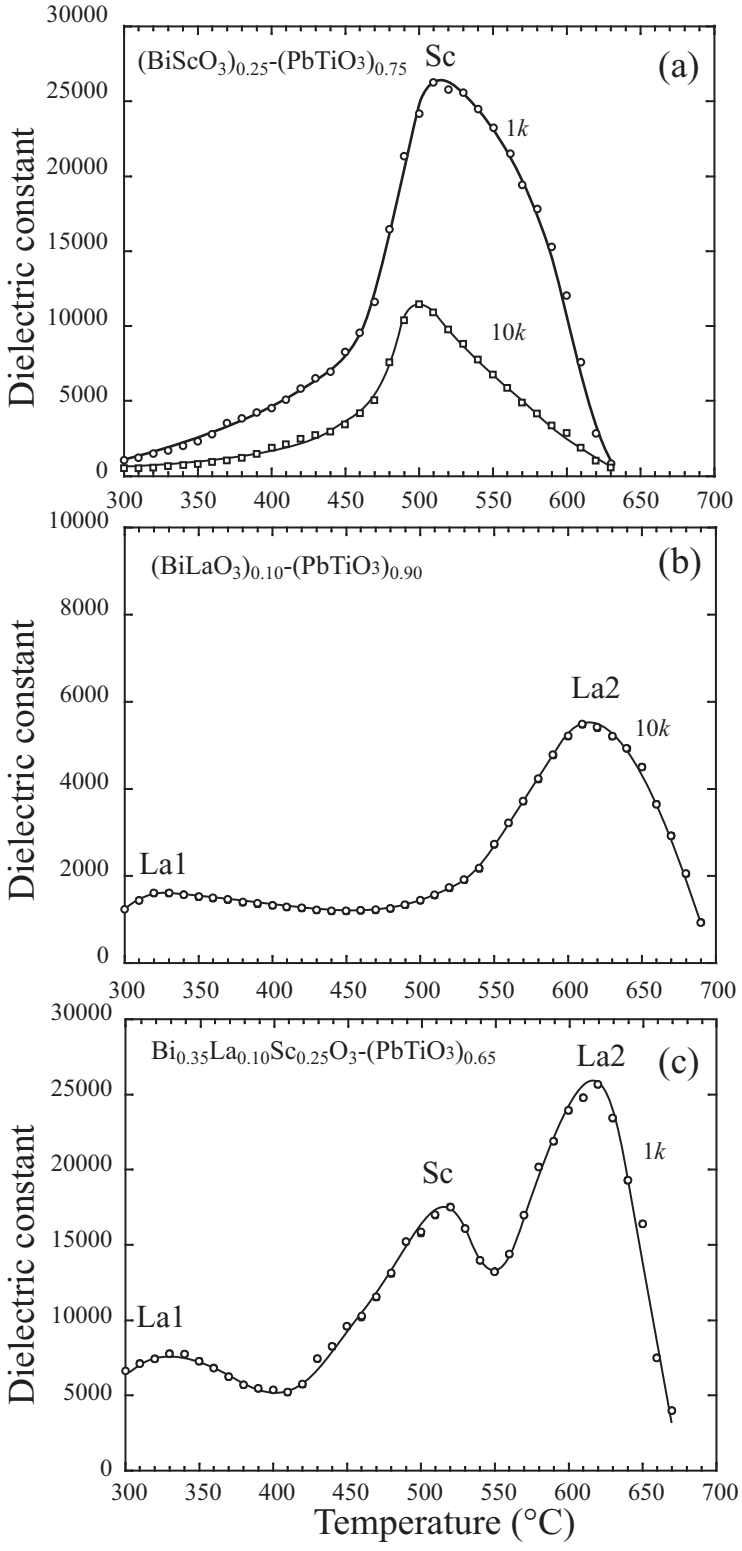

Fig 4.6: Dielectric constant of different BLS-PT compositions.

Figure 4.10 summarizes how the double doping of the B-site with Sc^{3+} and La^{3+} serves to enhance the detected peak 1 transition temperatures, while the positions for peak 2 shift to slightly lower temperatures.

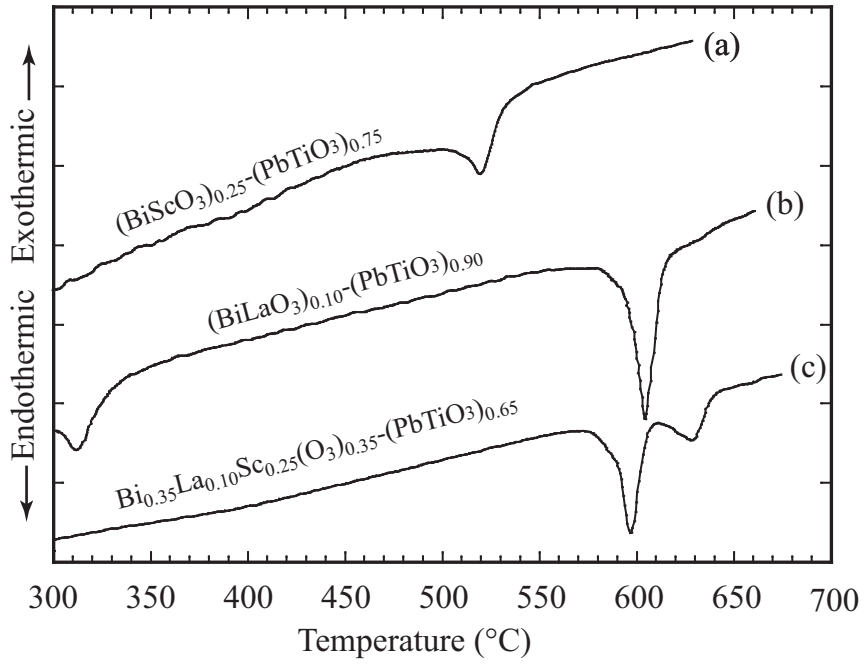

Fig 4.7: Differential scanning calorimetry scans in which endotherms indicate Curie transformations for same specimens whose dielectric response are depicted in Figure 4.6.

4.4 Discussion

Pure $PbTiO_3$ has a well defined tetragonal structure at room temperature with a c/a ratio of 1.065[9]. It has been known that doping of Pb(B'B")O_3 or Bi(B'B")O_3 to $PbTiO_3$ reduces the tetragonal distortion. With increasing substitution, the structure changes from tetragonal symmetry to rhombohedral through the narrow compositional range of the MPB. Both $BiScO_3$ and $BiLaO_3$ doping of $PbTiO_3$ appears to reduce the tetragonality of the corresponding solid solution systems [1, 11]. By partial substitution of La^{3+} for Sc^{3+}, compositions could also be formed with reduced tetragonality.

Figure 4.6a clearly suggests that T_c for xBiScO$_3$-$(1-x)$PbTiO$_3$ with $x = 0.25$ system is around 520°C. This is corroborated by the DSC endotherm displayed in Figure 4.7a. Likewise, Figure 4.6b depicts two transitions for the $(BiLaO_3)_{0.10}$-$(PbTiO_3)_{0.90}$ specimen

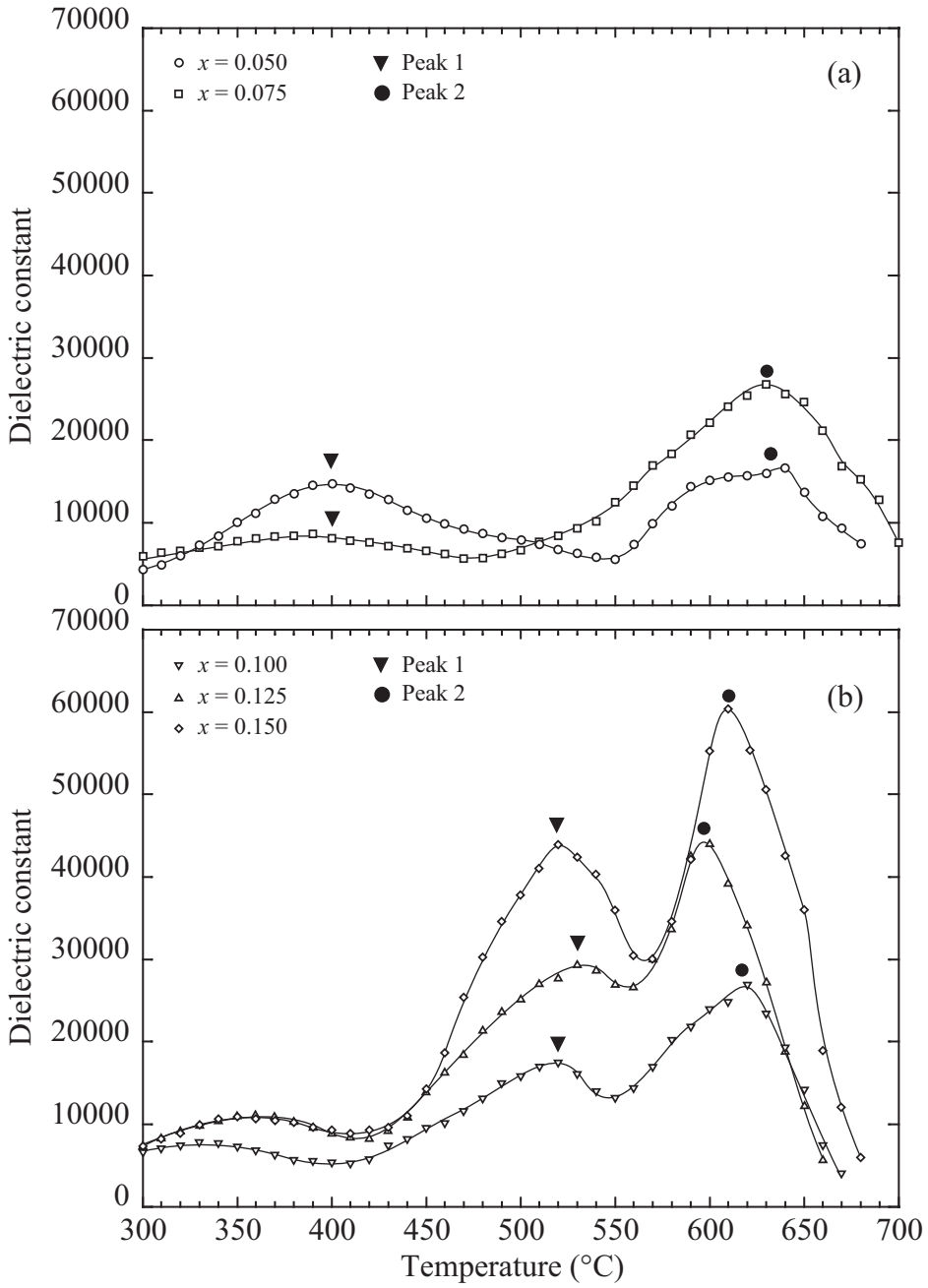

Fig 4.8: Dielectric constant at 1 kHz vs. temperature for various compositions of $Bi_{0.35}La_xSc_{0.35-x}(O_3)_{0.35}$-$(PbTiO_3)_{0.65}$ perovskite-structured solid solutions.

which are also detected by the DSC scan shown in Figure 4.7b. Figure 4.6c shows that all three transition peaks are detected in the combined $Bi_{0.35}La_xSc_{0.35-x}(O_3)_{0.35}$-$(PbTiO_3)_{0.65}$ specimen. However, the DSC scan in Figure 4.7c requires further explanation. The endotherms detected at 595°C and 630°C are most likely associated with the dielectric constant enhancement due to La^{3+} and/or Bi^{3+} substitution, appearing as a single convoluted dielectric constant peak at 620°C in Figure 4.6c. The lack of a DSC endotherm corresponding to the dielectric constant peak at ∼520°C implies a second-order transformation (no latent heat). High temperature XRD of xBiLaO$_3$-$(1-x)$PbTiO$_3$ specimens has confirmed that the macroscopically noncubic-cubic transition occurs at ∼310°C [11] which corresponds to the dielectric peak at ∼330°C. As can be seen from Figure 4.6, the dielectric constant of this $Bi_{0.35}La_{10}Sc_{0.25}(O_3)_{0.35}$-$(PbTiO_3)_{0.65}$ specimen seems to be a combination of the independent dielectric response of 0.25BiSc(O$_3$)-0.75PbTiO$_3$ and 0.10BiLa(O$_3$)-0.90PbTiO$_3$. For this $Bi_{0.35}La_{10}Sc_{0.25}(O_3)_{0.35}$-$(PbTiO_3)_{0.65}$ specimen, similar to 0.10BiLa(O$_3$)-0.90PbTiO$_3$ system, the low temperature peak is related to the macroscopically noncubic-cubic transition, which is associated with the breaking down of Ti-La long range order as suggested by previous chapter. The highest temperature peak is related to the annihilation of dipoles related to La B-site occupied clustering. The dielectric peak at around 500° is attributed to the activation of Sc related dipoles.

Based on the analysis above, the dielectric constant of the $Bi_{0.35}La_{0.10}Sc_{0.25}(O_3)_{0.35}$-$(PbTiO_3)_{0.65}$ system can be viewed as the combination of contributions of dipoles related to Sc^{3+} and dipoles related to La^{3+} when they form solid solutions with PbTiO$_3$. Similar to $Bi_{0.35}La_xSc_{0.35-x}(O_3)_{0.35}$-$(PbTiO_3)_{0.65}$ system, Jang *et al.* previously reported more than one dielectric peak in $Pb(Mg_{1/3}Nb_{2/3})O_3 : PbTiO_3 : Ba(Zn_{1/3}Nb_{2/3})O_3$ system and referred to the retaining of identity of Mg and Zn dipoles [10]. As in $Bi_{0.35}La_{0.10}Sc_{0.25}(O_3)_{0.35}$-$(PbTiO_3)_{0.65}$ system, when the temperature passed the macroscopic noncubic- cubic transition as indicated by the bump labeled La1, dipoles related to Sc^{3+} become thermally activated and cause the overall increase of dielectric constant (the low temperature dielectric constant peak) until thermal fluctuation by further increasing of temperature can randomize those dipoles and begin decreasing the dielectric constant. This assumes that

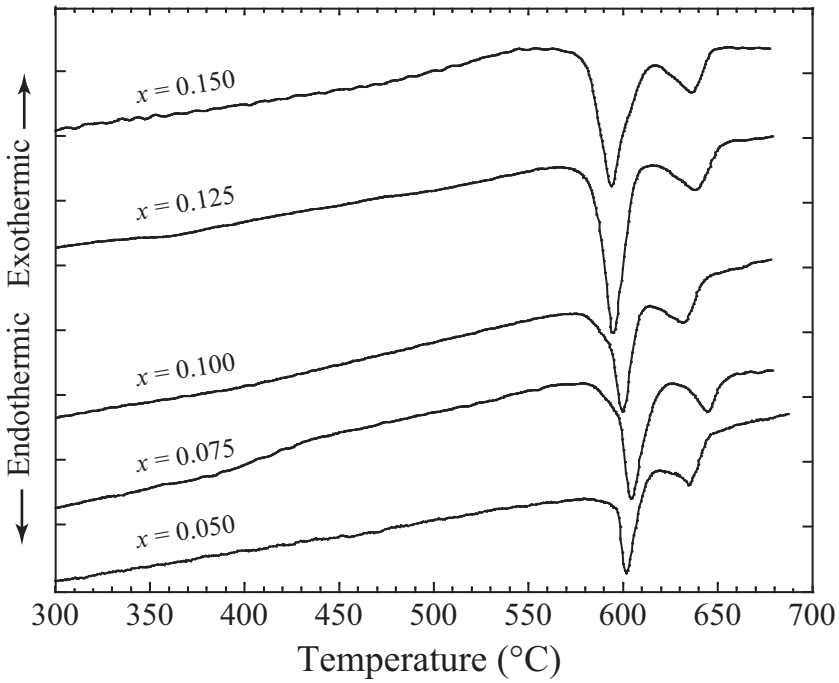

Fig 4.9: Differential scanning calorimetry scans of $Bi_{0.35}La_xSc_{0.35-x}(O_3)_{0.35}$-$(PbTiO_3)_{0.65}$ specimens with various x.

dipoles related to B-site La^{3+} clustering have not yet been activated so that the dielectric constant maximum observed in Figure 4.6a and 4.6c in the temperature range of 500°C can be mostly attributed to dipoles related to Sc^{3+}. With continued increasing of temperature to over 600°C, the dipoles related to La^{3+} B-site occupied clustering are then thermally activated, the overall dielectric constant rises up again hence showing the higher temperature peaks displayed in Figures 4.6b and 4.6c.

Evidence that this occurs in the $Bi_{0.35}La_xSc_{0.35-x}(O_3)_{0.35}$-$(PbTiO_3)_{0.65}$ system is obtained by comparing the positions of dielectric peaks in the simpler $(BiScO_3)_{0.25}$-$(PbTiO_3)_{0.75}$, $(BiLaO_3)_{0.10}$-$(PbTiO_3)_{0.90}$ specimens with a mixed sample containing the same Sc^{3+} and La^{3+} content (see Figure 4.6). The endotherms in Figures 4.7 show that the transitions over 400°C in both $(BiScO_3)_{0.25}$-$(PbTiO_3)_{0.75}$ and $(BiLaO_3)_{0.10}$-$(PbTiO_3)_{0.90}$ systems are first order. However, for the $Bi_{0.35}La_{0.10}Sc_{0.25}(O_3)_{0.35}$-$(PbTiO_3)_{0.65}$ specimen (Figure 4.6c) and all the $Bi_{0.35}La_xSc_{0.35-x}(O_3)_{0.35}$-$(PbTiO_3)_{0.65}$ specimens (Figure 4.8), latent heat was not detected for the transitions between 400°C and 520°C. This implies that second order (continuous in enthalpy) transitions occurred upon additional doping of Bi^{3+} and La^{3+}.

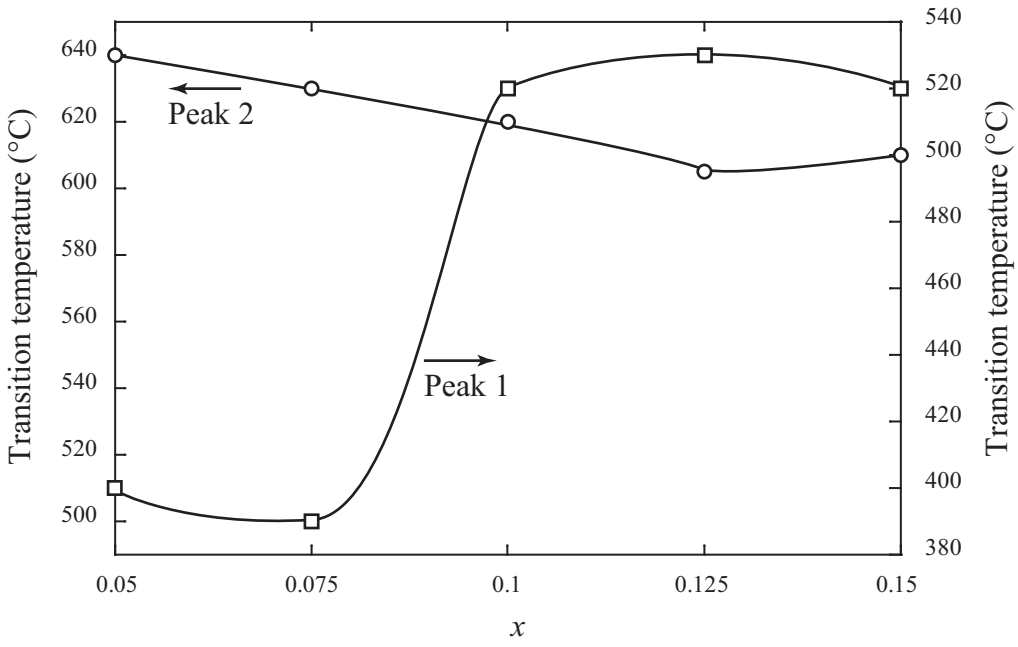

Fig 4.10: Transition temperatures indicated by dielectric peaks as labeled in Figure 4.8 for $Bi_{0.35}La_xSc_{0.35-x}(O_3)_{0.35}$-$(PbTiO_3)_{0.65}$ specimens with various x.

In order to understand the interplay between the Sc^{3+} and La^{3+} substitutions, Figure 4.8 is discussed next. In the xBiLaO$_3$-$(1-x)$PBTiO$_3$ system, the first dielectric constant peak associated with the macroscopic noncubic-cubic structural transition shifts to lower temperature as x is increased. For $x = 0.05$ and 0.075, the first dielectric constant peaks of the corresponding BLS-PT compositions are in the vicinity of 400°C [11]. While for xBiScO$_3$-$(1-x)$PBTiO$_3$ system, the dielectric constant peaks of composition with $x = 0.30$ and $x = 0.275$ are close to 460°C, and shift to over 500°C with further decrease in x. Thus in $Bi_{0.35}La_xSc_{0.35-x}(O_3)_{0.35}$-$(PbTiO_3)_{0.65}$ five cation system, low La^{3+} concentration, $x = 0.05/0.075$ (the temperature for the low temperature transition is high as in xBiLaO$_3$-$(1-x)$PBTiO$_3$ system) corresponds to high Sc^{3+} concentration 0.30/0.275(low transition temperature as in xBiScO$_3$-$(1-x)$PBTiO$_3$ system). Thus the dielectric constant peak of the ∼400°C transition for $x = 0.05$ and $x = 0.075$ are believed to be a convolution of the peak as in xBiLaO$_3$-$(1-x)$PbTiO$_3$ and the xBiScO$_3$-$(1-x)$PbTiO$_3$ peak associated with the noncubic-cubic transition(Figure 4.8a). For higher x, the dielectric response is almost identical and can be refereed to the analysis on composition with $x = 0.10$ above.

The positions of high temperature dielectric peaks ($\sim$ 620°C) displayed in Figure 4.8 matched the first endotherm positions in Figure 4.9. It can be seen in Figure 4.8 that the high temperature dielectric peaks are broadened especially for the specimens with $x = 0.050$ and $x = 0.075$. This can be explained by the fact that there might be two high temperature transformations as indicated by the DSC measurements. As discussed before, these higher temperature transitions appear to be associated with dipoles related to the large cations such as La^{3+}. The reason that two high temperature transitions are present may be because small amounts of A-site Bi^{3+} cations also exchange with B-site La^{3+} or Sc^{3+} and formed dipoles related to Bi^{3+}. Because of the large size of Bi^{3+}, these dipoles were randomized by thermal fluctuation at even higher temperature than those related to La^{3+}. Evidence that Bi^{3+} can also occupy B-sites has been observed in non-stoichiometric N-BS-PT composition [17].

4.5 Chapter Conclusions

Multiple dielectric transition peaks were detected in the dielectric spectra of $(BiInO_3)_{0.15}$-$(PbZr_{0.45}Ti_{0.55}O_3)_{0.85}$, $(Bi_{0.40}Sc_{0.38}(O_3)_{0.39})$-$(PbTiO_3)_{0.61}$, and $Bi_{0.35}La_xSc_{0.35-x}(O_3)_{0.35}$-$(PbTiO_3)_{0.65}$ perovskite solid solutions with $x = 0.050$ to $x = 0.150$. As in BLS-PT system, low temperature transitions, one at $\sim$330°C associated with the macroscopic noncubic-cubic structural transition in xBiLaO$_3$-$(1-x)$PbTiO$_3$, the other in the range 400-550°C are ascribed to Sc^{3+} related dipoles. A broadened high temperature transition in the 600°C and above range is ascribed to possible La^{3+} occupancy in the B-site. The highest temperature transition was confirmed by detection of a DSC endotherm. The source of the multiple dielectric peak behavior in these multiple cations compositions is therefore ascribed to possible B-site occupancy by the large cations In^{3+}, La^{3+} and Bi^{3+}. Experimental evidence showed that the thermal activation of dipole related to various B-site cations at different transition temperatures in $PbTiO_3$ solid solutions with Bi(B'B")O$_3$ are determined in great part by the sizes of those B-site cations.

4.6 References

REFERENCES

[1] R. Eitel, C. Randall, T. Shrout, S. Park, P. Rehrig and W. Hackenberger, "New High Temperature Morphotropic Phase boundary Piezoelectrics Based on $Bi(Me)O_3{-}PbTiO_3$ Ceramics," *Jpn. Journal of Applied Physics*, **40** [10] 5999 (2001).

[2] C. Randall, R. Eitel, B. Jones, T. R. Shrout, D. Woodward and I. Reaney, "Investigation of a High T_c Piezoelectric System: $(1-x)Bi(Mg_{1/2}Ti_{1/2})O_3{-}(x)PbTiO_3$," *Journal of Applied Physics*, **95** [7] 3633 (2004).

[3] R. Duan, R. Speyer, E. Alberta and T. Shrout, "High Curie Temperature Perovskite $BiInO_3$-$PbTiO_3$ Ceramics," *J. Mater. Res.*, **19** [7] 2185 (2004).

[4] M. Suchomel and P. Davies, "Enhanced Tetragonality in $(x)PbTiO_3{-}(1-x)Bi(Zn_{1/2}Ti_{1/2})O_3$ and Related Solid Solution Systems," *Applied Physics Letters*, **86** [26] 262905 (2005).

[5] J. Wang, J. B. Neaton, H. Zheng, V. Nagarajan, S. Ogale, B. Liu, D. Viehland, V. Vaithyanathan, D. Schlom, U. Waghmare, N. Spaldin, K. Rabe, M. Wuttig, and R. Ramesh, "Epitaxial $BiFeO_3$ Multiferroic Thin Film Heterostructures," *Science*, **299** [5613] 1719 (2003).

[6] C. Stringer, R. Eitel, T. R. Shrout, C. Randall and I. Reaney, "Phase Transition and Chemical Order in the Ferroelectric Perovskite $(1-x)Bi(Mg_{3/4}W_{1/4})O_3$-$xPbTiO_3$ Solid Solution System," *Journal of Applied Physics*, **97** [2] 024101 (2005).

[7] J. Iniguez, D. Vanderbilt and L. Bellaiche, "First-principles Study of $(1-x)BiScO_3$-$xPbTiO_3$ Piezoelectric Alloys," *Physical Review B*, **67** [22] 224107 (2003).

[8] J. Burfoot and G. Taylor, *Polar Dielectrics and Their Applications*, Berkeley: University of California Press, Berkeley and Los Angles, California, (1979).

[9] B. Jaffe, W. R. Cook and H. Jaffe, *Piezoelectric Ceramics*, Academic Press, New York, (1971).

[10] S. Jang, L. Cross and K. Uchino, "Dielectric and Electrostrictive Properties of Ferroelectric Relaxors in the System $Pb(Mg_{1/3}Nb_{2/3})O_3 : PbTiO_3 : Ba(Zn_{1/3}Nb_{2/3})O_3$," *Journal of The American Ceramic Society*, **64** [4] 209 (1981).

[11] R. Duan and R. Speyer, Unpublished work.

[12] R. Eitel, Doctoral Thesis, Pennsylvania State University, (2003).

[13] M. Zemansky and R. Dittman, *Heat and Thermodynamics: An Intermediate Textbook*, 6th ed., McGraw-Hill, New York, (1981).

[14] R. Clarke and L. Benguigui, "Tricritical Point in $BaTiO_3$," *Journal of Physics C-Solid State Physics*, **10** [11] 1963 (1977).

[15] K. Bethe and F. Welz, "Preparation and Properties of (Ba,Sr)TiO_3 Single Crystals," *Materials Research Bulletin*, **6** [4] 209 (1971).

[16] L. Benguigui and Y. Beaucamps, "A New Tricritical Point in Co-Doped Barium-Titanate," *Ferroelectrics*, **25** [1-4] 633 (1980).

[17] R. Duan R. Ou, R. Gerhardt and R. Speyer, Unpublished work.

[18] R. C. Buchanan, *Ceramic Materials for Electronics: Processing, Properties, and Applications*, New York, Marcel Dekker, (1986).

CHAPTER 5

Proposed Theory on the Origin of Morphotropic Phase Boundary (MPB) in $PbTiO_3$-based Solid Solutions

The research goals of this project are to develop Bi(B')/Bi(B',B") doped, $PbTiO_3$-based ferroelectric solid solution systems (preferably with MPBs) with high transition temperatures, and also investigate the structure-property relationships for those systems. A MPB is desirable since it would likely lead to good ferroelectric and piezoelectric properties. Unfortunately, as evidences showed in previous chapters, not all $PbTiO_3$-based, Bi(B')/Bi(B',B") doped solid solutions would have a MPB within the solubility limit. In order to understand the composition-structure relationship, it would be beneficial to look into the origin of the MPB at $PBTiO_3$-based systems. The following chapter uses a qualitatively thermodynamic theory to explain the necessary conditions for a MPB to appear in a solid solution system. This theory provides a tentative guidance for the compositional selection for a MPB type solid solution system.

5.1 Introduction

The ferroelectric solid solutions (PZT) formed between Lead titanate ($PbTiO_3$) and lead zirconate ($PbZrO_3$) are among the most investigated systems because their importance to the electromechanical industry. PZT along with some other solid solution systems (e.g. PMN-PT, PZN-PT), are the basis of most electromechanical devices in sonars, hydrophones, etc [1].

Recently, Considerable interest has been extended to the studying of so-called morphotropic phase boundary (MPB) found in those perovskite solid solution systems. The

phase diagram of PZT was originally established by Jaffe et al. as shown in Figure 5.1 [2]. In the hight temperature region labeled with P_C, PZT posseses a cubic perovskite structure and is in its paraelectric state. At lower temperature, there is an nearly vertical boundary near 48 mol% $PbTiO_3$ (with a change of 91K over 1% Ti content) which separate the ferroelectric regions with different crystallographic structures. The ferroelectric composition with $x > 0.48$ has a tetragonal structure with space group P4mm. The compositions with $0.20 < x < 0.48$ have a rhombohedral structure with space groups of R3c (LT) and R3m (HT). The exact location of the MPB was not previously well defined since there have been different models proposed for the MPB: a finite region where both tetragonal and rhombohedral phase coexist, with the maximum of the dielectric and piezoelectric properties at the edge of the coexistence region; a finite coexistence region in which one of the two phases is metastable [3]; and a true boundary, the observed coexistence region being explained either by unwanted compositional fluctuations [4], or by quenched-in thermal fluctuations [5]. The last paper proposes the width of the coexistence region to be inversely proportional to the particle size, which means that an ideal boundary would be observed in single crystal case (unfortunately, it is not possible to grow single crystal PZT), and would explain the variety of widths observed experimentally in ceramic samples.

One interesting question regarding the MPB boundary is, how it is possible to pass smoothly from the tetragonal side to the rhombohedral side with such an abrupt structural change? In such case, one would expect to find a two phase region separating the two solid solutions within the phase diagram. An indication of a way to explain the sequence of phases present across the MPB was given by Corker [6] in 1998, who carried out neutron powder structure analysis of the rhombohedral phase. In this paper, a model for disordered Pb position was proposed, which essentially could be interpreted in terms of local monoclinic distortions within individual unit cells. A following breakthrough work by Noheda et al [7], showed that a bridging monoclinic region at low temperature (< 400K) existed in PZT solutions (see Figure 5.3 a)) Such phenomenon was also observed in other important lead-based piezoelectric solid solutions, PZN-PT [8] and PMN-PT [9], and the schematics of the proposed phase diagrams are shown in Figure 5.3 b) and 5.3 c).

Glazer *et al* [10] has given a detailed explanation on the nature of the MPB. In their point of view, different crystallographic regions were determined by the way the unit cell is distorted (e.g. the disorder of Pb atoms), and the coherent ordering length of such cells. It was claimed that it is possible to account for the sequence of phases R3m, Cm, P4mm, so that there is in fact no distinct phase boundary that needs be crossed with varying the compositions. They came to the conclusion that *from a local structural point of view, there is no morphotropic phase boundary because both the rhombohedral and tetragonal phases (with the exception of pure $PbTiO_3$) are really monoclinic, but exhibit different degrees of structural distortion.*

Although a lot of work has been carried out on the investigations of MPB, there are still many fundamental questions associated with the true origin of the MPB remained answered unsatisfactorily. What is the cause for such an abrupt structural change for a small compositional change in the vicinity of the MPB? Will there will be a way to predict such a crystallographic characteristic change in complex solid solutions? Also, one of the most discussed subjects among the piezoelectric community was whether the origin of the dielectric and piezoelectric anomalies observed at the MPB was intrinsic [11] or extrinsic (mainly due to domain wall motion). Several attempts have been made towards developing a Devonshire-type phenomenological model [12]-[13] and first-principles model [14] of MPB systems. However, the electrical properties tend to vary for different processing techniques near the MPB due to variations in grain size, phase assemblage, and purity. This variability has frustrated many attempts to model the MPB. Single-crystals of PZT are very difficult to grow, but with the newly available relaxor-$PbTiO_3$ single crystals and PZT thin films, these materials may lead to new modeling developments.

Here a qualitatively theory based on thermal dynamics was proposed to explain the origin of the "MPB". PZT solid solution was selected as an example to present this theory. This theory can also be applied to other complex solid solutions such as PMN-PT etc. A few common phenomena in MPB ferroelectric systems can be explained self-consistently by applying this theory.

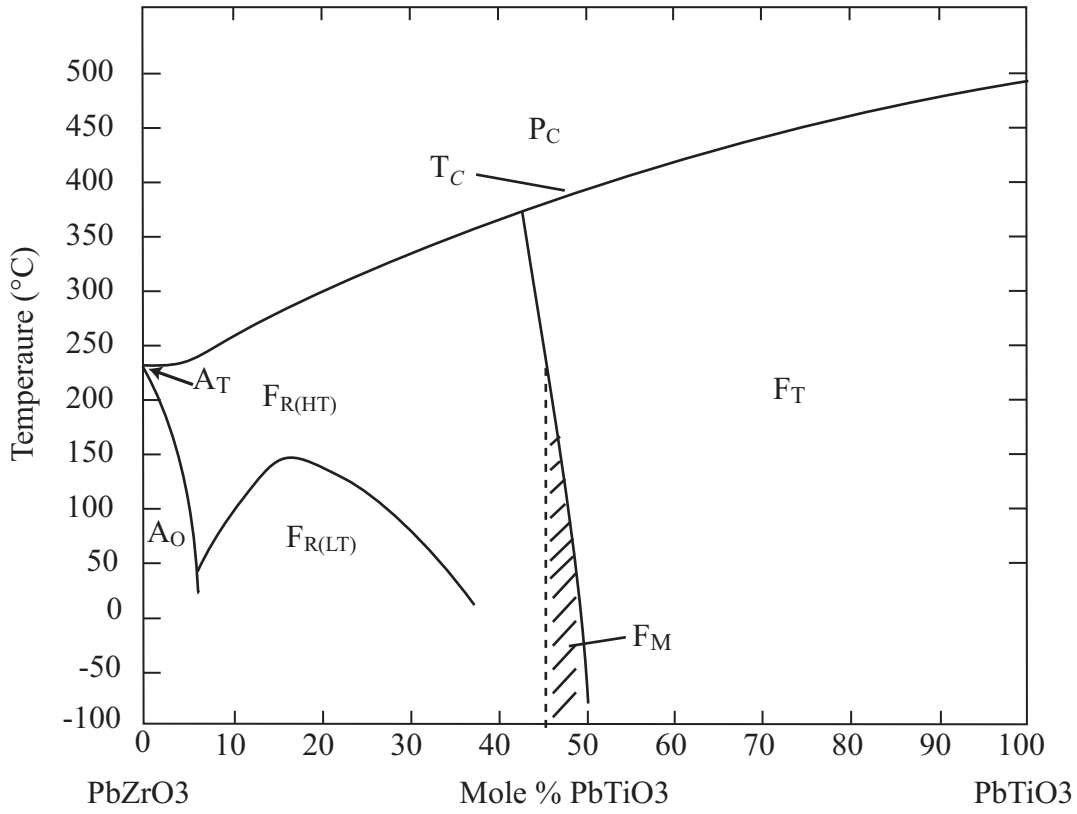

Fig 5.1: PZT "phase diagram".

5.2 Proposed Theory

In single phase solid solution, basic crystallographic structure can be categorized into: cubic, tetragonal, orthorhombic, hexagonal, rhombohedral, monoclinic and triclinic.

For those crystallographic structures, the geometric shape can be described using lattice constants and the angle between them. For example, triclinic would be $a \neq b \neq c$ and $\alpha \neq \beta \neq \gamma$. Taking into account that six of those crystallographic structures (exclude hexagonal) can be represented by a hexahedron, they can be viewed as the derivation of the cubic structure (similar in a phase diagram, low temperature phases are derived from high temperature liquid phase).

Here a new way to look at these structures (structural free energy state) is introduced to facilitated the interpretation (similar to Gibbs free energy for liquid, and corresponding solid phases in a binary phase diagram). This means that all these structures are internally

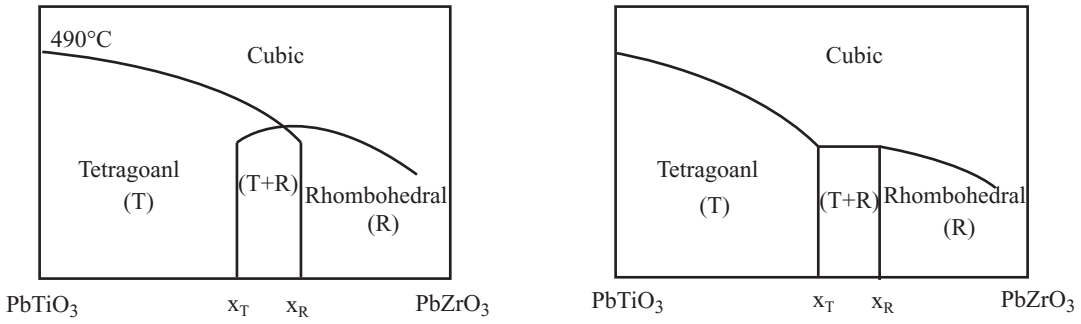

Fig 5.2: Two schematic representations of the morphotropic phase boundary in $Pb(Zr_{(1-x)}Ti_x)O_3$. (After Kakegawa et al. [1977(K)1]). T: tetragonal; O: Orthorhombic; C: cubic; M: monoclinic; R: rhombohedral.

related to each other and can also be generated by the combination of other structural energy states. Here we need 4 out of 7 structural energy states to represent six structural energy state (no hexagonal), which are Cubic, Tetragonal, Orthorhombic, and an energy ζ (ζ will be explained later).

Here is the example showing how it is constructed:

For a triclinic unit cell, the structure can be viewed as a distorted orthorhombic structure, with a body diagonal extension or contraction. The energy change is only related to the body diagonal extension (without changing the edge length of the hexahedron). It is labeled as ζ can can be visualized in Figure 5.4.

When structural energy states are combined, they have influence over each other. For example, the combination of cubic and tetragonal will tend to bring the tetragonal toward the cubic structure, the consequence would be the decrease in the lattice distortion (e.g. c/a ratio). The level of decrease in the distortion would be determined by the weight of those two factors (cubic energy state and tetragonal energy state), This is similar to considering a two phase region consisting a liquid and solid phase, where the relative amount for liquid and solid can vary in a wide range as indicated by the lever rule.

Based on the premises above, a tentative free energy interpretation was constructed to describe the different crystallographic regions in the "PZT phase diagram" and the transition between those structural regions.

The PZT solid solution can be viewed as binary system between $PbZrO_3$ (PZ) and

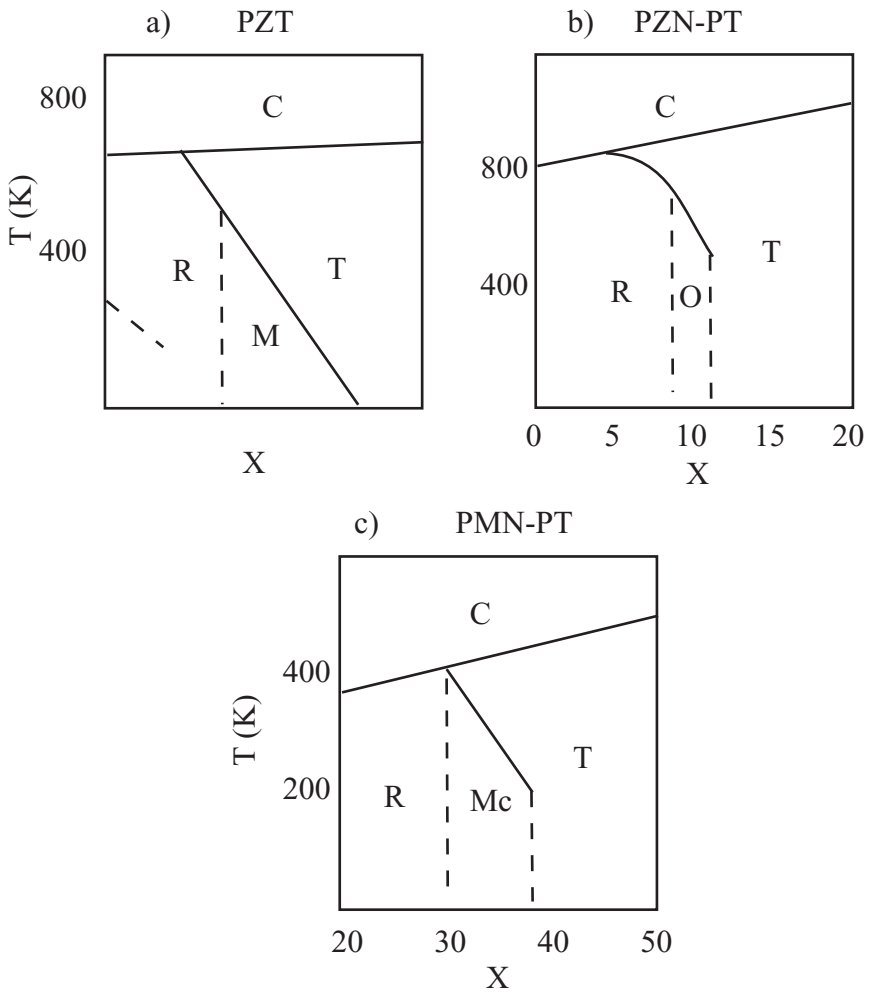

Fig 5.3: PZT "phase diagram" of different $PbTiO_3$ solidsolutions.

$PbTiO_3$ (PT). PZ possessed an orthorhombic structure at room temperature. The other end member, PT, has a tetragonal structure at room temperature. Each end member would go through a first order non-cubic to cubic transition at elevated temperature. Here, $\mu_{PZ,O}$ and $\mu_{PT,T}$ are assigned for the structural free energy of the PZ and PT at room temperature (O: orthorhombic, T: tetragonal). If in a perfected process that the Zr^{4+} and Ti^{4+} are homogenously distributed thoughtout the PZT solid solution, this solid solution can be reasonably treated as a "**regular solution**". In this case, the total free energy for the Cubic structured PZT solution at a temperature below the Curie temperature of the PZ (**using tetragonal PT and orthorhombic PZ as standard state**), with the presence of external electrical field and force field, can be expressed as follows:

$G_{SS,\ c} = X_{PZ}\mu_{PZ,O} + X_{PT}\mu_{PT,T} + RT(\ln X_{PZ} + \ln X_{PT}) + \Omega X_{PZ}X_{PT} + X_{PZ}\Delta G_{PZ,O\rightarrow C} + X_{PT}\Delta G_{PT,T\rightarrow C} + \phi(E) + \varphi(T)$;

ϕ(E) and φ(T) represent the electrical energy and mechanical energy respectively associated with external electrical field and force field. Here it can be seen that an excess energy term $\Omega X_{PZ}X_{PT}$ represents the influence between the PZ and PT endmembers. This is believed to be the energy to cause the body diagonal extension of a given structure.

In the following discussions, different temperatures are selected and the corresponding free energy curves associated with the four basic structural energy states are constructed. The determination of different crystallographic regions in PZT "phase diagram" are derived from these free energy diagrams.

Figure 5.5 shows that temperature T1 is selected to be above the Curie temperatures of both PZ and PT. At this temperature, the solid solution stays as cubic structure for all compositions. The lower portion of this figure is the free energy curve corresponding to the different basic crystallographic structural energy states. As can be seen from this figure, it is assumed that in the free energy curve, the orthorhombic has little "solubility" in tetragonal, or vice versa. Recall that the free energy of mixing PZ and PT to form a cubic structured solid solution is given by:

$\Delta G_{SS,\ c} = RT(\ln X_{PZ} + \ln X_{PT}) + \Omega X_{PZ}X_{PT} + X_{PZ}\Delta G_{PZ,O\rightarrow C} + X_{PT}\Delta G_{PT,T\rightarrow C} + \phi(E) + \varphi(T)$;

Here we assume that the sign of $\Omega X_{PZ}X_{PT}$ term is positive (the determination of the sign of this term will be explained later). The competing entropy term $RT(\ln X_{PZ} + \ln X_{PT})$ is negative. At a sufficiently high temperature, the entropy term dominates. Thus the cubic free energy curve is "convex downward" throughout the entire composition range.

Figure 5.6 displays the free energy curve for different structures at a temperature between the Curie temperature of PZ and PT. At this temperature, the entropy term $RT(\ln X_{PZ} + \ln X_{PT})$ is still dominant, so the cubic free energy curve is still "convex downward" throughout the entire composition range. Since the temperature is below the Curie temperature of PT, so the free energy of the compositions x_1 ($x_2 < x_1 < 1$) lies on the

common tangent line of the cubic and the tetragonal curve as indicated in the lower half of this figure. The compositions between x_2 and 1 have tetragonal structure at temperature T2. The composition at the tangent point (x_2) sets the boundary between the cubic and tetragonal regions.

A very important phenomenon in PZT solutions, that the decrease in the lattice distortion c/a, as the composition deviates from pure PT, can be explained by this figure. As explained in Figure 5.4, the combination of tetragonal and cubic energy state tend to change the lattice parameters of the tetragonal state leading to less tetragonality. As the composition x_1 shifts from 1 to x_2, following the lever rule, the weight of the cubic energy state in this cubic-tetragonal combination gets higher, thus the tetragonal state is "pulled" toward the cubic state, and results in a decrease in the tetragonality.

Figure 5.7 represents the free energy curves at T3. This figure is similar to the energy curves construction at temperature T2. One unique feature in this figure is that T3 is the critical temperature below which the cubic energy curve will shift from "concave downwards at all composition" (T2) to a mix of "concave downwards" and "concave upwards" (T4).

Figure 5.8 shows a temperature at which the cubic free energy curve shows a "concave upwards" region between x_1 and x_2. In this composition region, the temperature related entropy term $\mathrm{RT}(\mathrm{lnX_{PZ}} + \mathrm{lnX_{PT}})$ (negative) is overwhelmed by the excess free energy term $\Omega \mathrm{X_{PZ}X_{PT}}$ (positive). As mentioned above, the net effect of the excess energy is to cause the body diagonal extension. Thus the corresponding structure in $x_1 - x_2$ composition region is rhombohedral as the result of the combination of cubic and body diagonal extension. Similar to the energy curve construction at higher temperature (T2), the $x_2 - 1$ region represents the combination of cubic and tetragonal, thus the structure will stay as tetragonal. While for composition region from 0 to $x1$, as the free energy curve indicated, the structure is still cubic.

Figure 5.9 explains the origin of the monoclinic structural region which were recently discovered and studied by quite a few scientists [7]. For a given temperature T5, it can be seen that the x-ray detected monoclinic region is in the composition range (x_1, x_2). x_3 is the composition that separates the "concave upwards" and "concave downwards" regions

at the cubic energy curve. Thus the composition x_1, being in the "concave upward region", has an energy state of rhombohedral (cubic + ζ). From the common tangent line drawn on the free energy curves, it can be seen that the whole composition region between x_1 and 1 is the combination of the energy state rhombohedral(cubic + body diagonal extension) and tetragonal. Thus the combined effect is that the whole $x_1, 1$ region is essentially a tetragonal structure with body diagonal extension , which in turn is a monoclinic structured solid solution. The reason that the compositional range $x_2, 1$ is labeled as tetragonal is discussed here. When the composition shifts from x_2 towards 1, the weight of tetragonal state in this combination increases. This will decrease the weight of the cubic energy and excess energy related to the body diagonal extension, thus the monoclinic distortion becomes almost not observable in $x_2, 1$. In other words, the average detected structure goes through the transition between monoclinic and tetragonal. As predicted by Glazer et al [10], with further decrease in temperature, the excess energy becomes more influential and the detectable monoclinic region (x_1, x_2) becomes broader.

5.3 Application of the Proposed Theory

The proposed theory above can explain some phenomena related to phase transition in ferroelectric solid solutions:

1. Oh et al [15] reported that para-ferroelectric transition temperature increases with increasing tensile hydrostatic pressure. Contrary to these, opposite trends were predicted with increasing compressive pressure.

This phenomenon can be explained as follow:

Recall $\Delta \mathrm{G}_{SS,\ c} = \mathrm{RT}(\ln \mathrm{X_{PZ}} + \ln \mathrm{X_{PT}}) + \Omega \mathrm{X_{PZ}} \mathrm{X_{PT}} + \mathrm{X_{PZ}} \Delta G_{\mathrm{PZ,O}\rightarrow\mathrm{C}} + \mathrm{X_{PT}} \Delta G_{\mathrm{PT,T}\rightarrow\mathrm{C}} + \phi(\mathrm{E}) + \varphi(\mathrm{T})$;

As pressure being applied to the specimen, depending on how the pressure is applied, the sign of term $\varphi(\mathrm{T})$ which represent change of the mechanical energy introduced by the applied force field can be either negative or positive. If the sign of the mechanical energy term is positive, it means that the cubic state is less stable at a given temperature. For

the same $\Delta G_{SS,\ c}$, higher temperature is requited so that the term $RT(\ln X_{PZ} + \ln X_{PT})$ will be more negative and balance the positive mechanical energy term out. Thus the corresponding ferro-paraelectric transition temperature increases. On the other hand, if the sign of the mechanical energy term is negative, the cubic state becomes more stable, and the corresponding ferro-paraelectric transition temperature decreases. As can be seen in figure 5.10, at a temperature T, composition x is at the cubic-tetragonal boundary if there is no external field (Solid line). When the energy introduced by hydraulic pressure is positive, the cubic energy curve shifts upwards. The tetragonal region decided by the common tangent line between the cubic energy and the tetragonal energy curve extended to composition region (X_1, 1). The composition x now lies in the tetragonal region. This means that the corresponding tetragonal-cubic transition temperature increases. While if the energy introduced by hydraulic pressure is negative, the tetragonal region contracts to (X_2,1) and composition x is in the cubic region instead, which corresponds to a decrease in the tetragonal-cubic transition temperature.

Similar to the phenomena above, several reported electrical field introduced changes in structural transition temperatures can also be explained by evaluating the sign of energy introduced by the electrical energy term, $\phi(E)$. Depending how the external electrical field is applied, one would expect the energy curve associated with different structures change accordingly. Thus, the corresponding structure transition temperature for a given composition will adjust accordingly.

Not all $PbTiO_3$ based solid solution are expected to display a "MPB" type of crystallographic construction, e.g. $BiInO_3$-$PbTiO_3$ system [16]. What determins whether or not a $PbTiO_3$ solid solution would have a "MPB" character? Based on the analysis above, a "MPB" type PT based solid solution system should have cubic free energy which exhibits a mixing of "concave downwards" and "concave upwards" character. This means that cubic free energy of mixing in the solid solution system exhibits a positive deviation from ideal behavior [17]. If the cubic free energy shows a negative deviation from the ideal behavior, a "MPB" type character would not be expected. To further examine this question, what type of doping would cause the solid solution to have either positive or negative deviation

from ideal behavior? An observation is that almost all reported $PbTiO_3$ based "MPB" systems have a common character, which is that the dopants contain at least one cation that has de-occupied d or f electron orbitals. Thus transition metal cations are commonly seen as dopant elements in "MPB" type solid solutions. The de-occupied d or f electrons orbitals seem to make a contribution to this "MPB" phenomenon possible due to *spd* or *spdf* hybridization with neighboring atoms.

5.4 References

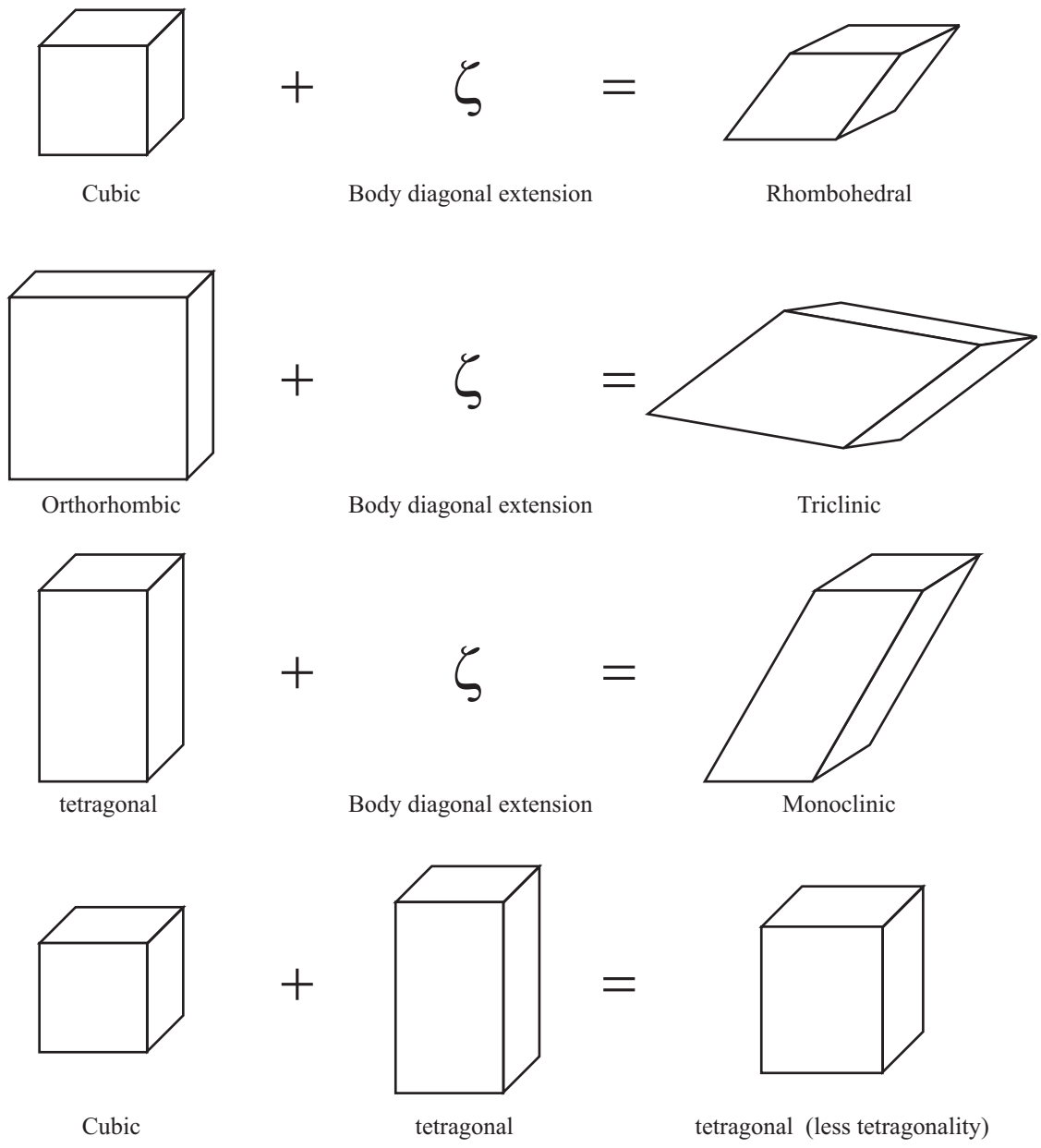

Fig 5.4: Illustration of certain structural energy states as the combination of other structural energy states.

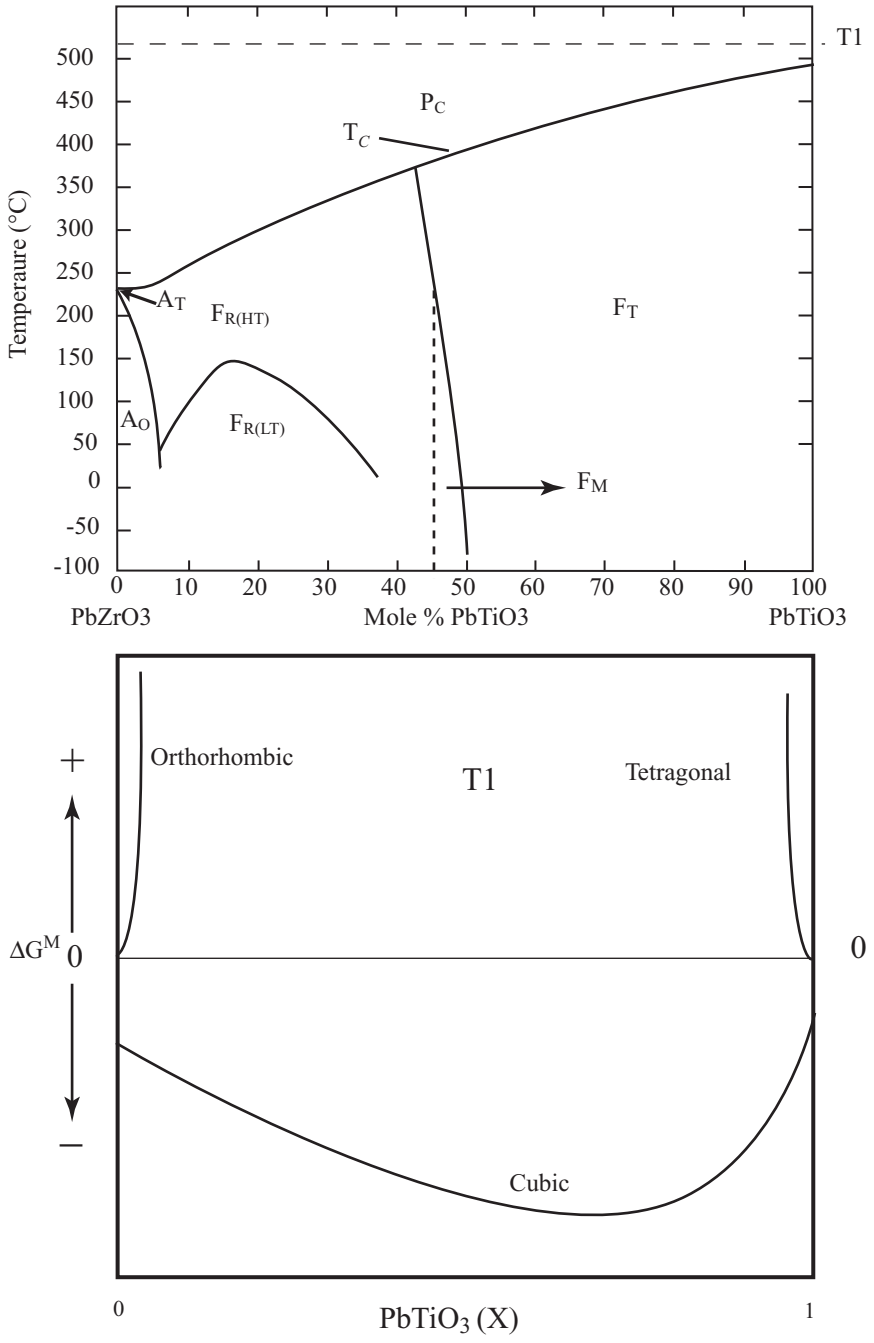

Fig 5.5: Free energy curves for basic structural energy states at a selected temperature T1.

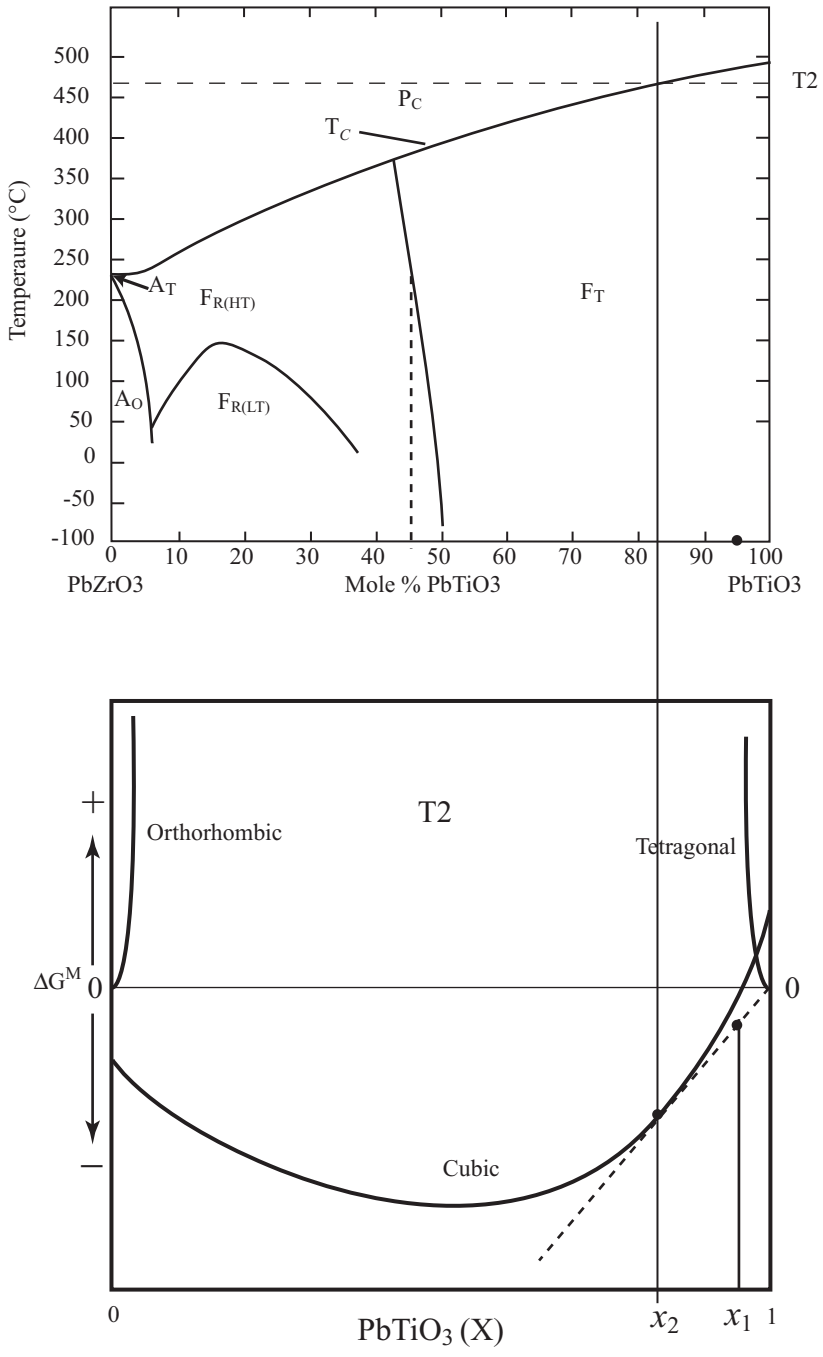

Fig 5.6: Free energy curves for basic structural energy states at a selected temperature T2.

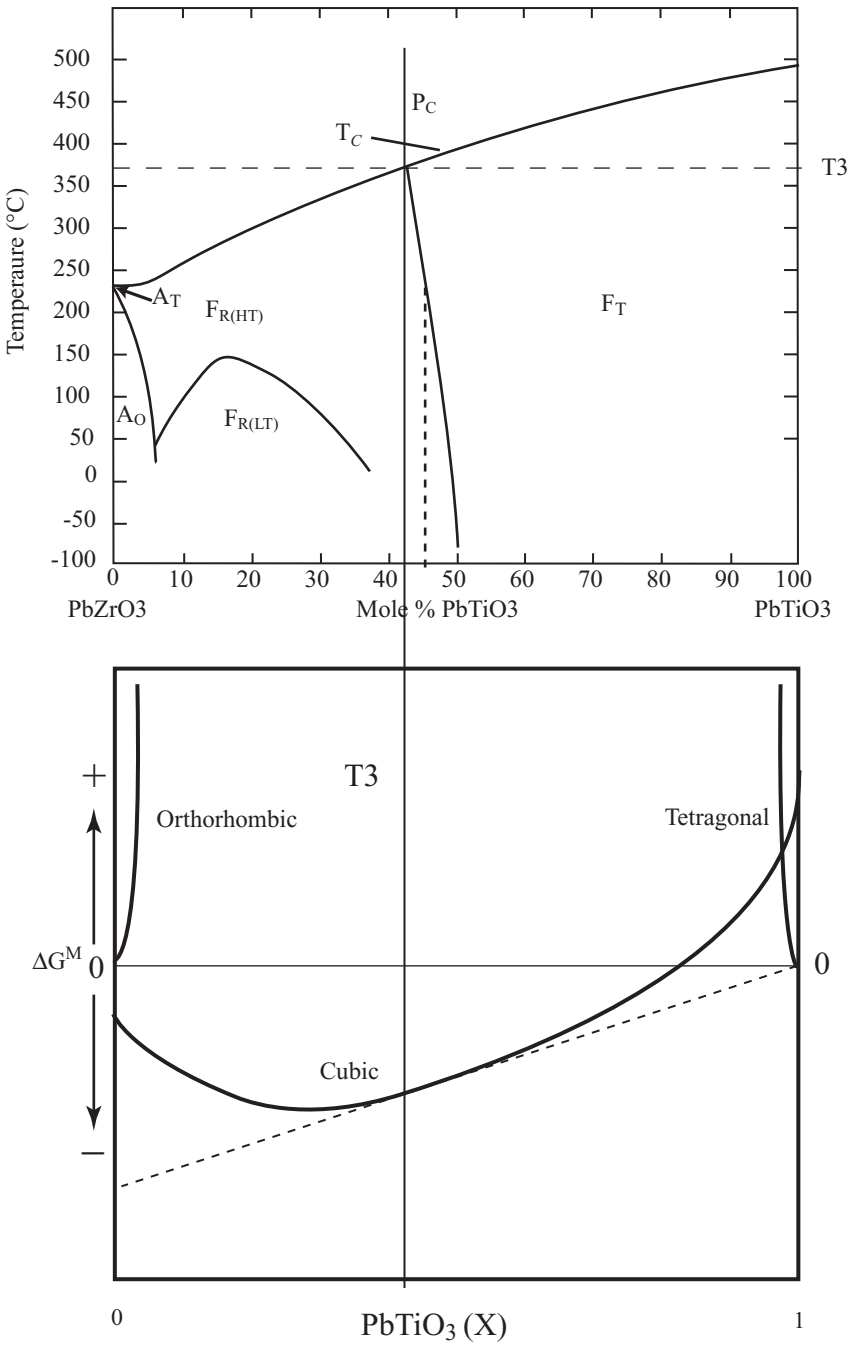

Fig 5.7: Free energy curves for basic structural energy states at a selected temperature T3.

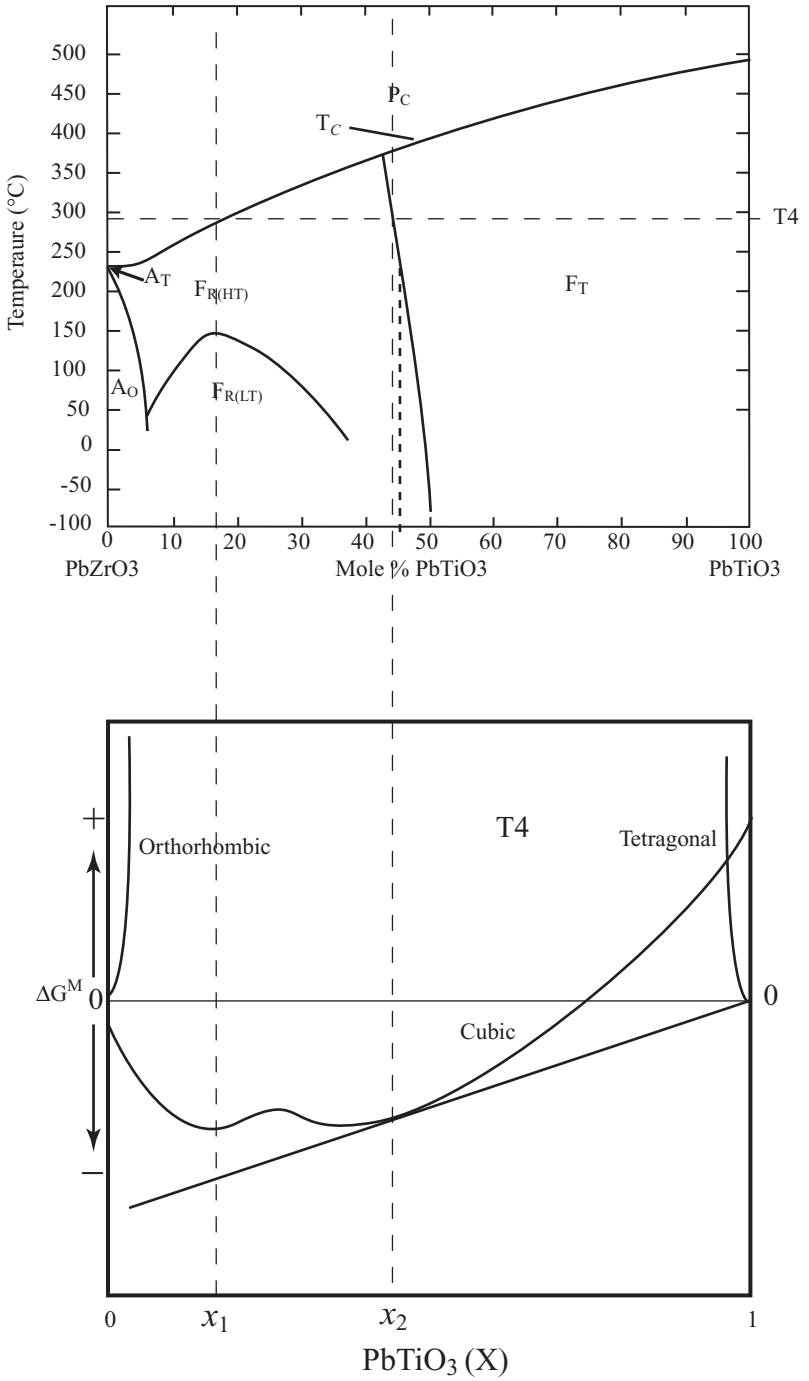

Fig 5.8: Free energy curves for basic structural energy states at a selected temperature T4.

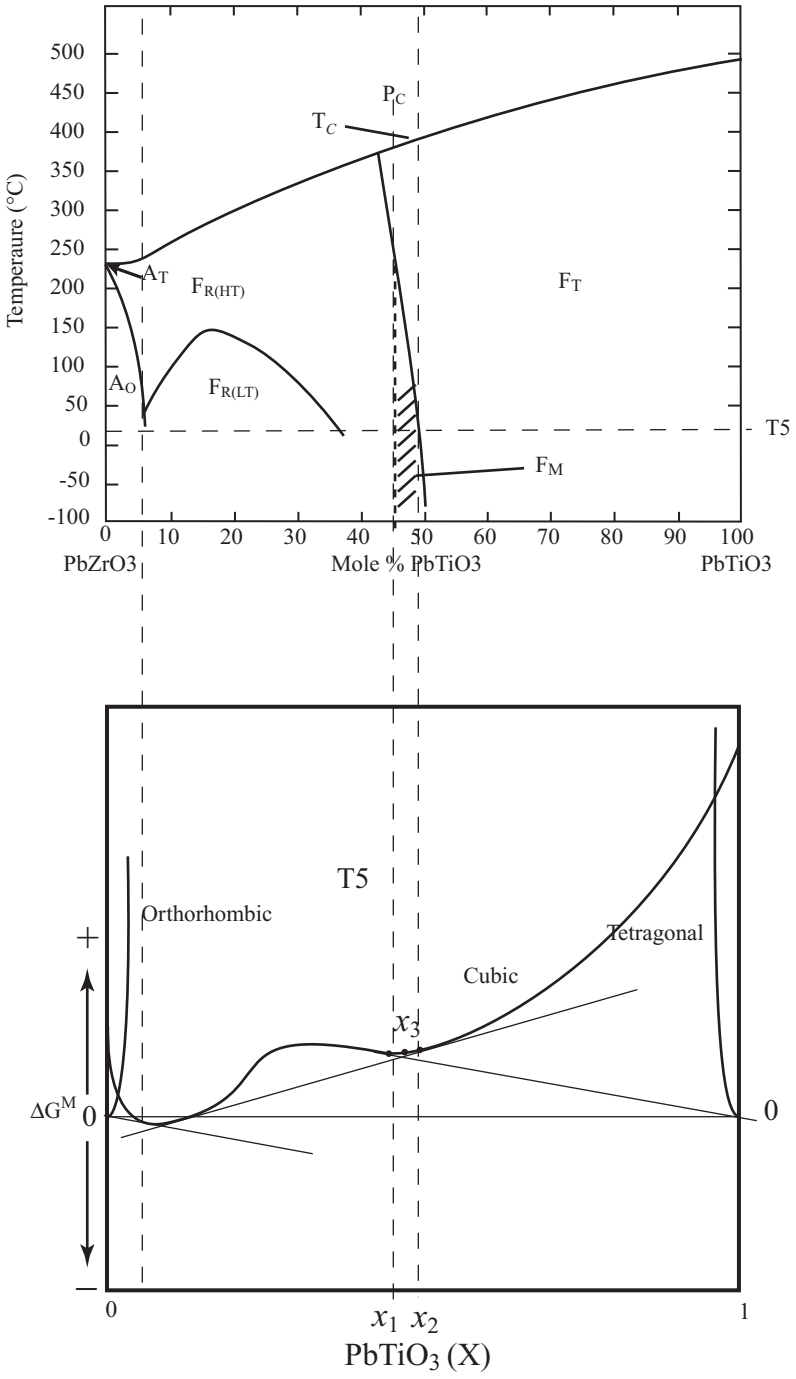

Fig 5.9: Free energy curves for basic structural energy states at a selected temperature T5.

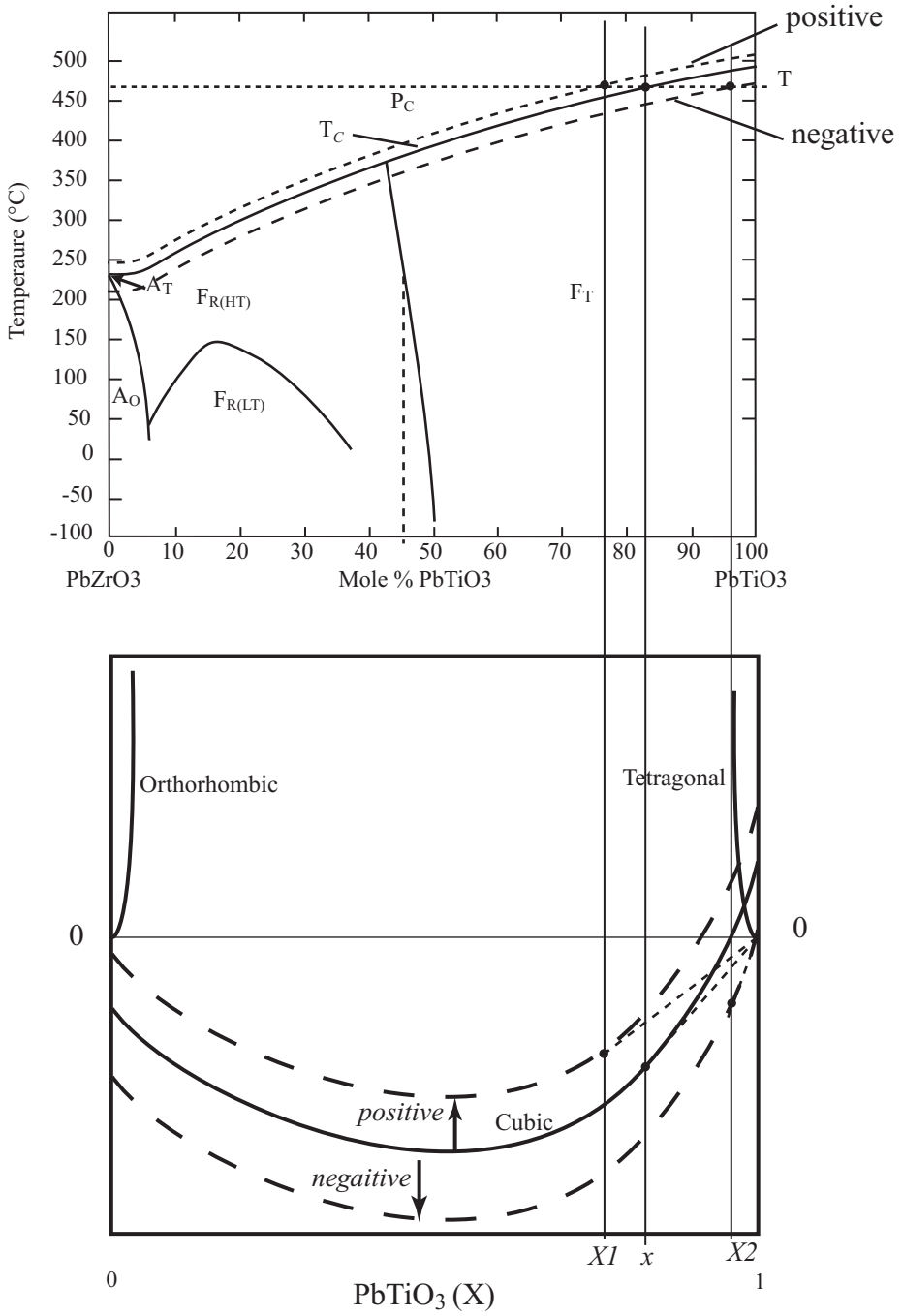

Fig 5.10: Illustration of the influence of the external field on the PZT transition temperature.

REFERENCES

[1] Y. Xu, *Ferroelectric Materials and Their Applications.* North-Holland, (1991).

[2] B. Jaffe, W. Cook Jr. and H. Jaffe, *Piezoelectric Ceramics,* Academic Press Ltd., New York, (1971).

[3] V.A. Isupov, Comments on the paper "X-ray study of the PZT solid solution near the morphotropic phase transition," *Solid State Communication* **17** 1331 (1975).

[4] K. Kakegawa, J. Mohri, T. Takahashi, H. Yamamura, S. Shirasaki, "Compositional Fluctuation and Properties of Pb(Zr,Ti)O_3," *Solid State Communication*, **24** 769 (1977).

[5] W. Cao and L. Cross, "Theoretical Model For the Morphotropic Phase Boundary in Lead Zirconate-titanate Solid Solution," *Physical Review B*, **47** 4825 (1993).

[6] D. Corker, A. Glazer, R. Whatmore, A. Stallard and F. Fauth, "A Neutron Diffraction Investigation into the Rhombohedral Phases of the Perovskite Series $PbZr_{(1-x)}Ti_xO_3$," *Journal of Physics: Condensed Matter*, **10** 6251 (1998).

[7] B. Noheda, D. Cox, G. Shirane, J. Gonzalo, L. Cross and S. Park, "A Monoclinic Ferroelectric Phase in the $Pb(Zr_{1-x}Ti_x)O_3$ Solid Solution," *Applied physics letters*, **74** 2059 (1999).

[8] D. La-Orauttapong, B. Noheda, Z. Ye, P. Gehring, J. Toulouse and D. Cox, "New Phase Diagram of the Relaxor Ferroelectric $(1-x)Pb(Zn_{1/3}Nb_{2/3}O_3$-$x PbTiO_3$," *Physical Review B* **65** 144101 (2002).

[9] B. Noheda, D. Cox, G. Shirane, J. Gao and Z. Ye, "Phase Diagram of the Ferroelectric Relaxor $(1-x)PbMg_{1/3}Nb_{2/3}O_3$-$x PbTiO_3$," *Physical Review B*, **66** [5] 054104 (2002).

[10] A. Glazer, P. Thomas, K. Baba-Kishi, G. Pang and C. Tai, "Influence of Short-Range and Long-range order on the Evolution of the Morphotropic Phase Boundary in $Pb(Zr_{1-x}Ti_xO_3)$," Physical Review B, **70** 184123 (2004).

[11] Y. Ishibashi and M. Iwata, "Morphotropic Phase Boundary in Solid Solution Systems of Perovskite-type Oxide Ferroelectrics," *Japanese Journal of Applied Physics*, **37** 985 (1998).

[12] K. Carl and K. Hardtl, "On the Orign of the Maximum in the Electromechanical Activity in $Pb(Zr_xTi_{1-x})O_3$ Ceramics Near the Morphotropic Phase Boundary," *physica status solidi (a)*, **8** 87 (1971).

[13] A. Amin and L. E. Cross, "Effect of Electric Boundary Conditions on Morphotropic Pb(Zr,Ti)O_3 Piezoelectrics," *Japanese Journal of Applied Physics*, **24** 229 (1985).

[14] B. Burton, R. McCormack, B. Toby, and E. Goo, "Cation Ordering in Some ABO_3 Perovskites," *Ferroelectrics*, **194** 187 (1997).

[15] S. Oh and H. Jang, "Three-dimensional Phase Diagram of the Pb(Zr,Ti)O_3 System under Hydrostatic Pressure," *Ceramics International*, **26** 565 (2000).

[16] R. Duan, R. Speyer, E. Alberta and T. Shrout, "High Curie Temperature Perovskite $BiInO_3$-$PbTiO_3$ Ceramics," *Journal of Materials Research*, **19** [7] 2185 (2004).

[17] D. Gaskell, *Introduction to the Thermodynimics of Materials*, New York, (2003).

CHAPTER 6

Conclusions

Perovskite solid solutions xBiInO$_3$-$(1-x)$PbTiO$_3$ (BI-PT), xBiLaO$_3$-$(1-x)$PbTiO$_3$ (BL-PT), and complex xBi(B', B")O$_3$-$(1-x)$PbTiO$_3$ (where B' and B" refer to 3+ cations) were fabricated using conventional ceramic processing. The extent of Bi(B')/(B'B")O3 substitution in the perovskite system and the corresponding shifts in the transition temperatures were investigated using thermal analysis, dielectric measurements, x-ray diffraction, and electron microscopy. A qualitative theory on the origin of morphotropic phase boundary (MPB) was proposed. This theory facilitates the understanding of composition modification influence on the composition-structure relationship in the PZT system. It predicts the circumstances in which a MPB is expected for a Bi(B')/Bi(B',B") doped PbTiO$_3$-based solid solution system.

xBiInO$_3$-$(1-x)$PbTiO$_3$ (BI-PT) and xBiLaO$_3$-$(1-x)$PbTiO$_3$ solid solution both showed enhanced transition temperature. The transition temperature for BI-PT system reached 582°C for $x = 0.20$. While transition temperatures as high as ∼600°C were observed in BL-PT systems. Nb-modified xBiInO$_3$-$(1-x)$PbTiO$_3$ showed increased resistivity and can be poled for electromechanical measurement. Compared to pure BI-PT, the transition temperature decreased as result of Nb modification. 1.5 Nb mol%-0.15BI-0.85PT composition showed high transition temperature (542°) and good electromechanical properties. Double dielectric anomalies were observed for composition with $x \geq 0.05$. The double dielectric peak were attributed to two transitions at different temperatures. The low temperature peak was a result of macroscopically tetragonal-cubic transition as indicated by hot-stage X-ray. While the high temperature peak was speculated as a result of the segregation of B-site cations, as well as the formation of polar nano-regions.

Multiple dielectric constant peaks were detected in the dielectric spectra of $(BiInO_3)_{0.15}$-$(PbZr_{0.45}Ti_{0.55}O_3)_{0.85}$, $(Bi_{0.40}Sc_{0.38}(O_3)_{0.39})$-$(PbTiO_3)_{0.61}$ and a series of $Bi_{0.35}La_xSc_{0.35-x}(O_3)_{0.35}$-$(PbTiO_3)_{0.65}$ (BLS-PT) ($0.05 \leq x \leq 0.15$ solutions; Evidence in BLS-PT system showed that dielectric response detected at different temperatures may related to dipole/nanoploar regions associated with different B-site cations (Sc^{3+} and La^{3+}). The source of the multiple dielectric peak behavior in these multiple cations compositions is ascribed to possible B-site occupancy by the large cations In^{3+}, La^{3+} and Bi^{3+}.

The results from the systems investigated provided experimental evidence that the transition temperatures in $PbTiO_3$ solid solutions with Bi(B', B")O_3 are determined in great part by the sizes of the B-site cations.